AMERICAN UNIVERSITY OF BEIRUT

Biomimetic Humanoid Gait Design and Push Recovery

by

Noel Joseph Maalouf

A dissertation
submitted in partial fulfillment of the requirements
for the degree of Doctor of Philosophy
to the Department of Electrical and Computer Engineering
of the Maroun Semaan Faculty of Engineering and Architecture
at the American University of Beirut

Beirut, Lebanon
November 2018

AMERICAN UNIVERSITY OF BEIRUT

Biomimetic Humanoid Gait Design and Push Recovery

by

Noel Joseph Maalouf

Approved by:

_____

Dr. Imad H. Elhajj, Professor   Advisor

Electrical and Computer Engineering

_____

Dr. Ali Chehab, Professor   Chairperson of Committee

Electrical and Computer Engineering

_____

Dr. Daniel Asmar, Associate Professor   Member of Committee

Mechanical Engineering

_____

Dr. Elie Shammas, Associate Professor   Member of Committee

Mechanical Engineering

_____   on behalf : Ali Chehab

Dr. Ning Xi, Professor   Member of Committee

Industrial and Manufacturing Systems Engineering, The University of Hong Kong

_____

Dr. Najib Metni, Associate Professor   Member of Committee

Mechanical Engineering, Notre Dame University

Date of dissertation defense: November 7, 2018

AMERICAN UNIVERSITY OF BEIRUT

THESIS, DISSERTATION, PROJECT
RELEASE FORM

Student Name: __Maalouf__   __Noel__   __Joseph__
                          Last   First   Middle

◯ Master's Thesis   ◯ Master's Project   ⊘ Doctoral Dissertation

☐   I authorize the American University of Beirut to: (a) reproduce hard or electronic copies of my thesis, dissertation, or project; (b) include such copies in the archives and digital repositories of the University; and (c) make freely available such copies to third parties for research or educational purposes.

☑   I authorize the American University of Beirut, to: (a) reproduce hard or electronic copies of it; (b) include such copies in the archives and digital repositories of the University; and (c) make freely available such copies to third parties for research or educational purposes after: **One ___ year from the date of submission of my thesis, dissertation or project.**
Two ___ years from the date of submission of my thesis , dissertation or project.
Three ✓ years from the date of submission of my thesis , dissertation or project.

_____   17/12/2018
          Signature   Date

This form is signed when submitting the thesis, dissertation, or project to the University Libraries

Acknowledgements

More than five years of graduate life at AUB were filled with fun moments but also many difficulties. I thank God for putting amazing friends in my path during this important stage of my life. Ali Kanso, our friendship started during my first days at AUB, became stronger throughout our graduate studies, and I hope it stays for life. Thank you for your help and for the side chats we had during our breaks. Serge Mghabghab and Aline Eid, thank you for all the good times we shared. No matter how far our lives take us apart I hope we stay close friends. Haytham Dbouk, thank you for showing me that we can pursue many goals at the same time as long as we put our minds to it. I will always cherish our friendship. Abbas Sidaoui, I will never forget our adventures during the past couple of years. I hope our paths cross again so we can enjoy many more.

To all my relatives, thank you for always being there for me. Your emotional support kept me on my feet during the tough times. To my uncle, Prof. Abdo Salameh, thank you for inspiring me to pursue my PhD. You have been my academic role model since childhood and I hope to follow in your footsteps throughout my career. Uncle Fuad Maalouf, thank you for setting an example of loyalty and dedication. I am proud to share your love for AUB which you served for more than forty years. In memory of my uncles Tony & Fawzi Maalouf and Georges & Elie Salameh whom I lost during the past few years. I wish you were with us to witness my achievement.

Last but most importantly, I would like to thank my parents for their endless support. I could not have done it without you. No words can express my gratitude to the sacrifices you made so I can be the man I am today. No matter what I do, I will always be in you debt. I ask God to keep you in good health and promise to always make you proud.

An Abstract of the Dissertation of

Noel J. Maalouf   for   Doctor of Philosophy

                                   Major: Electrical and Computer Engineering

Title: Biomimetic Humanoid Gait Design and Push Recovery

Humanoid robots are among the most recognizable robotic systems in exploration, industrial applications, and personal assistance. However, like all bipedal systems, the main challenge that faces humanoid locomotion is stability. Humanoids are vulnerable to balance disturbances. The risks of humanoid falling are not limited to the robots but also affect the humans around them. The research efforts in humanoid stability in the past few decades have been far from shy, but there is still a long path before full stability is reached. This thesis presents biomimetic techniques for humanoid fall avoidance and gait design. The main two problems addressed in this thesis are push recovery during quiet standing and stability during walking. The proposed push recovery strategy is inspired by human reliance on three main sensory information to assess their posture: visual, vestibular, and somatosensory. Fusing sensory inputs enables the robot to adapt to different environmental changes during locomotion. Experimental results show improvements in maximum joint-torque exertion of up to 17.5% and response time by 9.3%. Inspired by excessive human reliance on somatosensory information, a model-free push recovery strategy is also developed enabling small-scale commercial humanoids to make use of foot pressure sensors to reject disturbances from any direction and at any location on the body. The proposed strategy withstands around 8.0% higher magnitude push disturbances compared to standard control methods. On a related note, kinesiologists define the energy-exchange theory as the main guidance for human walking. In this thesis, an energy-exchange gait generation technique is developed through formulating an optimization problem capable of maintaining this human-inspired property. Additionally, a new Energy-Based Controller is developed to drive the generated energy-exchange gait. The new controller not only maintains the desired gait an-

gles but also is more efficient in terms of energy expenditure and torque exertion on the joint motors. The proposed gait improves total mechanical energy needed by 4.9% in simulations and 1.8% in experiments. The proposed algorithms are simulated on two commercial humanoids, the Hoap2 and Nao in Webots. Experiments are also performed on the Nao humanoid in order to validate the proposed hypotheses. The strategies developed in this thesis contribute to safer humanoid locomotion by providing human-like pose estimation, sensory integration, and maneuverability. The biomimetic framework aids in reducing the gap between humans and humanoids and improves the integration of robots into the society.

Contents

List of Figures

List of Tables

Dedicated to my parents, Joseph and Vergina.

Chapter 1

Introduction

Bipedal systems are mechanisms that move using the help of two rear limbs or legs [4]. The dependence on two legs for support renders them more vulnerable to balance disturbances such as trips and push forces. Humans perform robust and efficient gaits, however it is challenging to apply human-like gait on bipedal robots. In this thesis, new methods of bipedal stability and gait design are presented. These methods are biomimetic in nature and they are inspired by human posture assessment, push recovery strategies and motion characteristics.

1.1   Motivation

Bipedal stability is an ongoing area of research that has been widely visited especially in the past couple of decades. The challenge behind this research topic is that bipedal systems are by nature more prone to instabilities than other systems such as quadrupeds. The 2-legged support creates an unstable system which is vulnerable under external disturbances as well as ego motion.

By investigating the problems in using bipedal robots one might question the need to use them in the first place. A main advantage which bipedal robots hold over other types of robots is the ability to traverse various types of terrains including stairs and uneven floors with pits and cavities. Moreover, bipeds also are more efficient in traversing confined areas as they have a smaller footprint than wheeled robots.

While bipedal systems are essential for several tasks, ensuring their safe and efficient operation is a challenge that still faces researchers in this domain. The main challenge lies in maintaining bipedal stability without restricting maneuverability and limiting the tasks that the robot can perform. One of the main disturbances that the robot might encounter during its operation is a push force that disrupts its balance and thus requires a reaction from the robot to maintain stability.

Humanoid push recovery could be divided into two main categories. The first

is push recovery during quiet standing. This problem has been investigated by several researchers and various methods have been developed to ensure humanoid balance against external disturbances. The other category of humanoid push recovery is during gait. While both areas have been tackled by researchers, there is still significant room for improvement which lies in the strategies followed for push recovery and fall avoidance.

1.2 Objectives

While reviewing the current and past research on humanoid push recovery and fall avoidance, several areas for improvements can be found which are summarized in the points below.

- The strategies applied during quiet standing are model-dependent and thus have to be tailored differently when applied on different humanoids.

- The approach is in most cases taking a pure mechanical aspect which makes it harder to introduce a more human-like fall avoidance approach for small-scale commercial humanoids. This approach would render humanoid push recovery and fall avoidance smoother and more energy-efficient since the humans hold exemplary behavior which should be targeted.

- The existing work that implements human-like walking for small-scale humanoids still lacks depth and needs to be investigated more thoroughly.

The aim of the thesis is to implement strategies for humanoid fall avoidance and gait design considering the following points:

- **Obj. 1:** Humanoid fall avoidance during quiet standing that follows human-like strategies while considering dynamic changes in the environment.

- **Obj. 2:** Humanoid fall avoidance during quiet standing that could be implemented on different humanoids, i.e. model-independent.

- **Obj. 3:** Humanoid gait design that applies human-inspired strategies.

- **Obj. 4:** Humanoid gait design that is energy-efficient.

- **Obj. 5:** Humanoid gait design that is robust against external push disturbances.
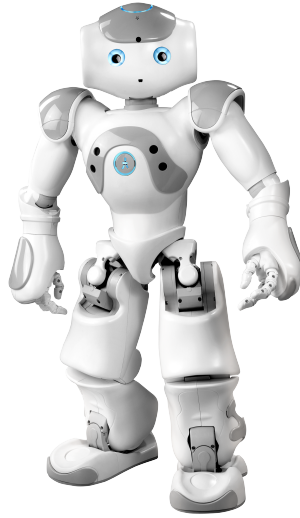
Figure 1.1: Nao H25 V3.3 by Aldebaran [1]

1.3 Humanoids used in Simulations and Experiments

The humanoids used in this thesis are the Nao H25 robot (Fig. 1.1) developed by Aldebaran and Hoap2 developed by Fujitsu [5]. Nao's height is 57.3 cm and it weighs 5.4 kg. It has 25 degrees of freedom and various types of sensors for perceiving the environment, measuring ego motion and interacting with other robots or operators. Hoap2 is 48 cm tall, weighs 7.03 kg, and has 25 degrees of freedom.

The simulator used to test the algorithms is the Webots simulator developed by Cyberbotics (Fig. 1.2). Webots provides an environment to test the fall avoidance and push recovery strategies under various conditions. The robot properties and the physical properties of the environment can be set by the user and changed for testing different scenarios. This allows testing for different push force magnitudes and directions.

1.4 Contributions

This thesis holds contributions in the area of humanoid push recovery and stable gait design. The main contributions are listed below.
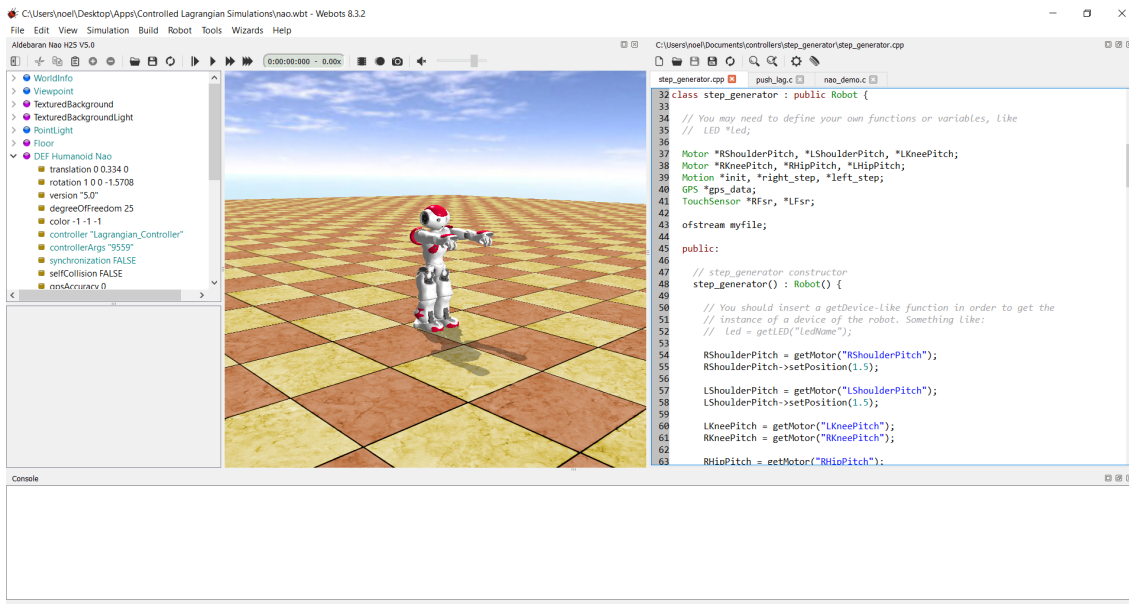
Figure 1.2: Webots Simulator by Cyberbotics

1. Human-like humanoid posture estimation through the integration of Visual MonoSLAM and gyroscope measurements. This helps in overcoming the limitation of a predetermined distance between the humanoid and the visual scene. While the integration of Visual MonoSLAM has been widely used in the literature, to the best of our knowledge it has not been used in humanoid posture assessment.

2. Visual sensory input assessment through the introduction of blur and brightness factors to accurately evaluate the quality of the acquired visual pose estimation. These factors are used to decide the degree of reliance on each of the camera and the gyroscope information during quiet standing posture assessment.

3. High-magnitude disturbance rejection against sudden impacts for small-scale commercial humanoid platforms. This improves robot maneuverability as compared to the small-angle swaying disturbance rejection found in the literature.

4. A model-free control algorithm, which can be applied on any humanoid having foot pressure sensors without any prior knowledge of the robot's parameters. This simplifies and generalizes the application of the presented algorithm.

5. The model-free system is more robust to unexpected changes in the hu-

manoid's interaction with the environment. For example, a model-based algorithm would perform poorly in cases where there is a change in the location of the humanoid's Center of Mass (CoM). However, in the model-free algorithm the change is directly reflected by the foot pressure sensors readings.

6. The introduction of a new Energy-Based Controller (EBC) for humanoid joint control during both quiet standing and gait. The new controller is more energy-efficient than standard control methods and provides human-like motion.

7. Novel humanoid gait synthesis based on the human-inspired energy-exchange theory. The designed humanoid gait is more energy-efficient and stable against push disturbances. Combined with the EBC, the proposed gait produces human-like locomotion and push recovery.

1.5 Thesis Outline

The remainder of the thesis is organized as follows. In Chapter 2, a brief overview of human posture assessment and fall avoidance strategies is given. This lays the ground for the biomimetic gait design and push recovery techniques developed for small-scale humanoid robots.

Chapter 3 covers the state of the art humanoid balance techniques found in the literature and highlights the areas of contribution that this thesis focuses on to improve push recovery and achieve stable human-like gait design.

In Chapter 4, a new sensory reweighting algorithm for humanoid push recovery during quiet standing is introduced. This algorithm mimics the human posture assessment by modifying the reliance on different sensors in accordance with the environment the robot is operating in. The visual sensory input is also improved with the integration of blur and brightness evaluation techniques to evaluate the credibility of the visual information.

A model-free push recovery algorithm is presented in Chapter 5 where the humanoid's proprioceptive sensors are used to estimate its posture and recover from push disturbances using the human-inspired ankle strategy. The significance of this method lies in the ability to reject disturbances from any direction and at any part of the humanoid's body, not necessarily its Center of Mass.

Chapter 6 covers energy minimization techniques found in the literature that are used for humanoid gait design and control. This chapter highlights the weaknesses of the currently used techniques and paves the way for the human-inspired gait synthesis presented in this thesis.

The new gait design algorithm is presented in Chapter 7. This design is inspired by the energy-exchange theory that guides human gait. Also, in this

chapter, a new Energy-Based Controller is developed and employed in the energy-exchange gait to replace the standard PID controller in achieving the desired joint angles during humanoid walking.

Chapter 8 presents concluding thoughts about this thesis and provides areas of possible future work.

Chapter 2

Human Fall Avoidance and Gait

The objective of this chapter is to give a general overview about important concepts related to the strategies of human posture assessment, fall avoidance and walking. First, an overview is given of the different sensory information involved in human posture assessment. Then, the three main push recovery strategies during quiet standing are covered. The mechanics behind human motion are then analysed from the viewpoint of Kinesiology.

2.1   Human Posture Estimation

The approach for humanoid fall avoidance in this thesis is biomimetic in nature. In fact, humans possess superior balance capabilities and mimicking them would help devise a more robust fall avoidance system. During quiet standing, humans tend to rely on three sensor information: visual sensors, vestibular sensors (otolith and semi-circular canals), and somatosensory/proprioceptive information (coming from muscles and joints) [6].

Vision plays an important role in human balance recovery, while it contributes to approximately 10% of the control, it is found to be the most critical in the decision making [7]. Vision describes the relative motion to the environment [6]. The brain processes visual information in order to differentiate between ego-motion and object motion in the environment. The vestibular system is reported to contribute 20% of the human balance control [8], sensing both angular velocity and linear acceleration of the head [9]. The angular velocity is provided by semi-circular canals, while the otolith organs measure the linear acceleration. Both of these organs lie in the human's inner ear. The vestibular system can be thought of as a level sensor; as the sensor is tilted the fluid inside the sensor (inside the ear of a human) reaches its edge, thereby triggering a feeling that one is falling. As for the somatosensory or proprioceptive information, it includes joint positions as well as muscle activity which are valid indicators of the human posture [10]. This system contributes to 70% of the posture control since it needs the least

processing. Given the information from the different sensory inputs and the current postural state, the role of the balance control strategy is to find the best path to reach the target posture [11, 12]. It is important to note that the role of vision is not restricted to the differentiation between ego-motion and the moving environment. The visual information is used to perceive the environment, thus affecting the choice of recovery strategies to regain balance [13]. Another factor affecting the sensor fusion is the processing time of information coming from the different sensors [14]. The visual information take longer processing time than vestibular and proprioceptive sensory inputs [15]. Event-Related Potential (ERP) readings reveal that a demanding visual processing task can take between 150 and 300 ms to be processed [15], while vestibular and proprioceptive inputs require around 90 to 100 ms of processing [16, 17]. The different response rates affect reweighting and that is why the percentage of reliance on visual inputs is relatively lower than vestibular and proprioceptive information.

2.2   Human Push Recovery Strategies

After assessing their posture, humans apply three main strategies to overcome external disturbances. The first strategy that humans follow is the ankle strategy [18]. Torque is applied at the ankle joints opposite to the direction of the disturbance. When the magnitude of the disturbance grows, the ankle strategy is no longer capable of preventing a fall and humans tend to apply the hip strategy, where the hip rotates along the direction of the disturbance in such a manner to absorb the disturbance, then it stops and returns to the equilibrium position using the hip and ankles [19]. When subjected to yet a higher magnitude disturbance, it is only through stepping that humans can avoid falling. This may be accomplished by taking one or more steps depending on the magnitude of the disturbance. A demonstration of the three aforementioned strategies is shown in Fig. 2.1, 2.2, and Fig. 2.3. In humanoid fall avoidance, the stepping strategy is usually considered as a last resort when the ankle and hip are no longer sufficient. However, humans deal with this problem in a different way. Evidence from the literature in Kinesiology [20] indicates that humans tend to take a step way before the magnitude of the disturbance reaches the ankle and hip thresholds. The key difference lies in the information processing and decision-making strategies that the human body uses to keep its balance. This lies in environment perception which guides human interaction with the surroundings to maintain balance.

When studying human posture, kinesiologists differentiate between ideal posture and normal posture [21]. Ideal posture requires the least amount of muscular support and minimizes the stresses on the joints. In other words, it is a hypothetical term that represents the posture which minimizes the loads in the supporting ligaments [21]. Normal posture however, presents the actual joint angles and torques that result from extensive experiments on human subjects with no im-
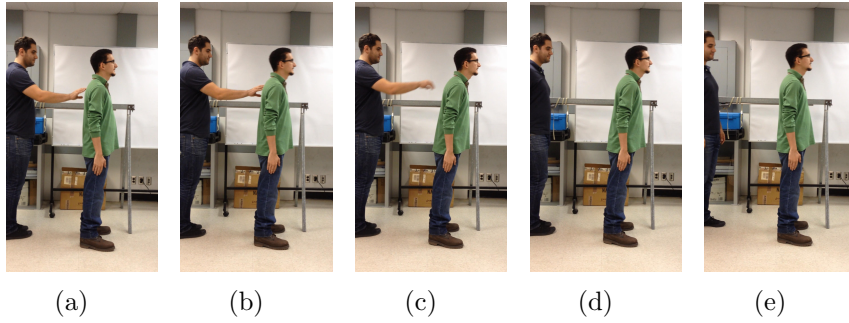
Figure 2.1: Demonstration of the ankle strategy.
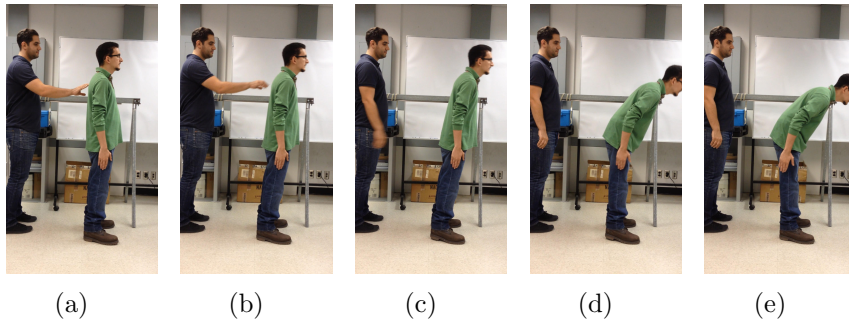
Figure 2.2: Demonstration of the hip strategy.

pairments. The experiments focus on the line of gravity, which is the vertical projection of the Center of Gravity [22]. Experiments show that during quiet standing, the line of gravity must lie within the border of the supporting feet in order to maintain equilibrium. Therefore, the ideal posture is when the Line of Gravity passes through the axes of rotation of the related joints [22]. However, in reality there is no perfect posture, so the line of gravity tends to pass anteriorly or posteriorly to the affected joint axes. This is the normal posture. As the distance separating the line of gravity from the joint axis increases, the gravitational moment increases, and thus a counter torque is needed to decrease the distance [22].

The arms play a key role in human balancing and even in fall management [23]. They are usually used to absorb the fall in the absence of a possibility to recover. However, this thesis focuses on the role of the lower body in fall avoidance, push recovery and gait design without accounting for the arms because including the arms would require working with models of high degrees of freedom.

(a)   (b)   (c)   (d)   (e)
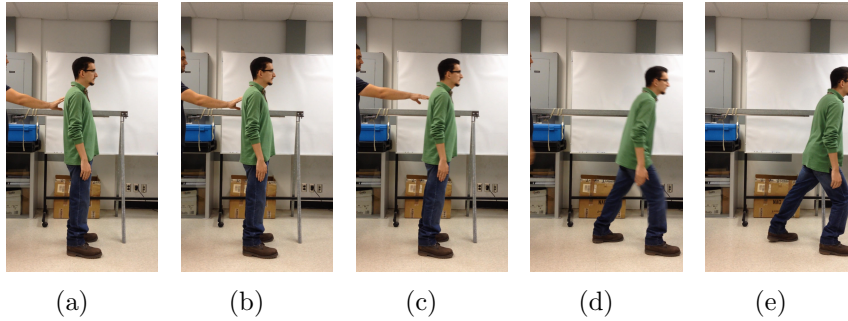
Figure 2.3: Demonstration of the stepping strategy.

2.3 Human Walking from the Viewpoint of Kinesiology

The complexity of human movement has taken years of research in the fields of biomechanics as well as psychology [24]. Each motion is guided by the assessment of the environment, awareness of the body's ego-motion, and planning of the next step [25]. The focus in this thesis is on finding human motion characteristics capable of being utilized in humanoid gait planning and fall avoidance.

2.3.1 Mechanics of Human Walking

Human gait is a cyclic motion consisting of repetitive events or phases [26]. The stance phase of human gait represents the time when the reference foot is placed on the ground, thus it is called the stance foot [21]. While the stance phase makes up around 60% of the gait cycle, the remaining 40% are covered by the swing phase during which the leg swings to reach the next contact point with the floor.

Examining the significance of the swing and stance phase of gait provides a framework for characterizing the movements in each phase of gait. While the ultimate goal of locomotion is the movement from one position to another, the stance and swing phases contribute to that goal in different ways. The stance phase has three tasks in locomotion: providing adequate support to avoid a fall, absorbing the shock of impact between the limb and the ground, and providing adequate forward and backward force for forward progress [27].

In brief, human walking can be visualized as a double inverted pendulum where each foot is a pendulum pivot [28]. While walking at a constant preferred speed, an asymmetrical motion between the right and left halves of the body guides the gait.

2.3.2 Equilibrium Point Hypothesis

The Equilibrium Point (EP) hypothesis was introduced in 1959 by a group of researchers at the Russian School of Physiology [29]. The main purpose behind EP hypothesis is to study the relationship between involuntary and voluntary movements through Neurology and Physiology. If a person is carrying an object with one arm and the object is suddenly removed, the arm undergoes an involuntary motion to return to equilibrium. However, if the same person is reaching for an object, the arm undergoes a voluntary movement to complete the task [30]. While both movements may not seem visibly different, they generate different EMG signals and involve the release of different motor-neurons.

In the context of postural stability and gait, the EP hypothesis can be used to give a more general definition to these phenomena. Contrary to traditional views, the EP hypothesis considers posture stability and locomotion as a homogeneous problem where stability during locomotion is a result of an intentional reset of the equilibrium point by the nervous system [31].

While having a unified framework for stability during both quiet standing and gait is desirable, there remains the issue of choosing which muscles/joints to activate for achieving this stability. According to the EP hypothesis, this choice is guided by the goal of energy minimization [30]. This transforms the problem of motor redundancy to a luxury of motor abundance [31, 32]. The EP hypothesis has put several aspects of human posture and locomotion into perspective, however the concept of energy minimization raised a question which created a turning point in this thesis: *What if there is a higher characteristic that guides human walking and all other properties are just subsets of it?* Fortunately, the answer was found in the Energy-Exchange theory.

2.3.3 Energy-Exchange Theory

Human movement consists of three hierarchical levels: *strategic*, *tactical*, and *executive* [33]. The *strategic* level is represented by the cerebellum, the neurons are involved at the *tactical* level, and the *executive* level is mostly managed by the muscles and joints. While most approaches in robotics focus on the *executive* level, the focus in this thesis is on finding a characteristic embedded at the *strategic* level of human locomotion and that could be mapped to humanoid robot motion.

Although the concept of energy minimization is inspired by human Kinesiology, the methods applied to obtain this minimization in small-scale humanoid gait are still far from the way humans behave. This is due to the fact that the energy minimization is a very broad theory that applies to many systems, not only biological ones.

In order to reach a more human-like gait, a special characteristic, exclusive to human locomotion must be found. Once this feature is set as a reference, a
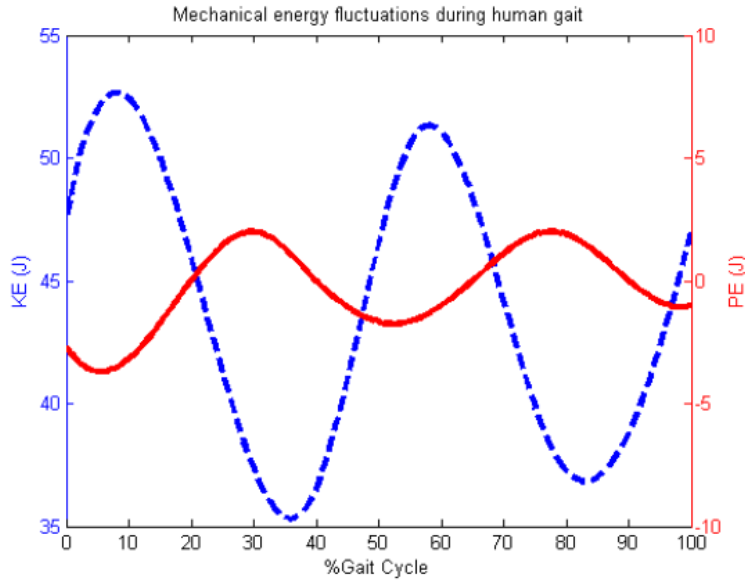
Figure 2.4: Mechanical energy fluctuations showing kinetic energy (KE) and potential energy (PE) out-of-phase [2]

model following approach can be utilized to obtain human-like walking. Luckily, Cavagna *et al.* [34] has pinpointed this characteristic around forty years ago. However, it remained in the field of kinesiology and hasn't been applied yet in the field of humanoid locomotion. The theory states that in order to minimize energy during gait, humans make use of the imperfect linear inverted pendulum mechanism of energy-exchange [34]. This means that during gait at constant (preferred) speed, KE and PE of the human's CoM oscillate in a perfect out-of-phase fashion which allows energy-exchange to occur. The out-of-phase KE and PE oscillations are seen in Fig. 2.4 [2]. The exchange between KE and PE conserves energy expenditure during walking and complies with human tendency to minimize energy as demonstrated by Kinesiologists [34].

The total amount of positive muscle work done during human gait is divided into two main categories; internal and external work [2]. Internal work is the work done by the muscles and tendons of the body that doesn't result in the displacement of the body's CoM. External work on the other hand, is the work that accelerates and elevates the body's CoM. Therefore, the energy minimization lies in minimizing the external work. When KE and PE are oscillating in an out-of-phase manner, around 70% of the external mechanical energy can be recovered [2, 34]. The remaining energy must be supplied by the muscles and tendons.

This realization opens new horizons in the design and control of humanoid gait. It narrows down the target of minimizing mechanical energy to keeping KE

Gait Parameter	Parameter Value
Average step width	11.88 cm
Right stride length	133.489 cm
Left stride length	132.427 cm
Right step length	66.393 cm
Left step length	67.096 cm
Average speed	128.67 cm/s

Table 2.1: Gait Parameters for Constant Speed Forward Walking

and PE out-of-phase throughout the constant speed gait cycle.

The theory of imperfect inverted pendulum energy-exchange highlights the importance of the 3D inverted pendulum developed by Kajita *et al.* [35]. The use of this model with the energy-exchange theory as a reference leads to a more human-like gait.

In order to further understand the human gait, data is obtained online from Limb Fitting Centre in Scotland [36]. Experiments consist of 25 trials done on 5 young adults. The subjects were told to walk at their preferred constant speed in the forward direction. Angle values of different joints were captured using the Vicon motion capture system and published online available for research purposes. The parameters of the gait experiments are summarized in Table 2.1.

The sample oscillations of the joint angles during human gait are shown in Fig. 2.5 and Fig. 2.6. The right and left joint angle oscillations are plotted together for comparison purposes. It is clear from the above plots that there also exists an out-of-phase pattern between the right and left sides of the body. For example, the right and left elbow oscillations in the third plot of Fig. 2.6 are clearly out-of-phase. Right and left hip pitch variations are also out-of-phase as can be seen in the third plot of Fig. 2.5. This realization backs the theory of inverted pendulum energy-exchange.
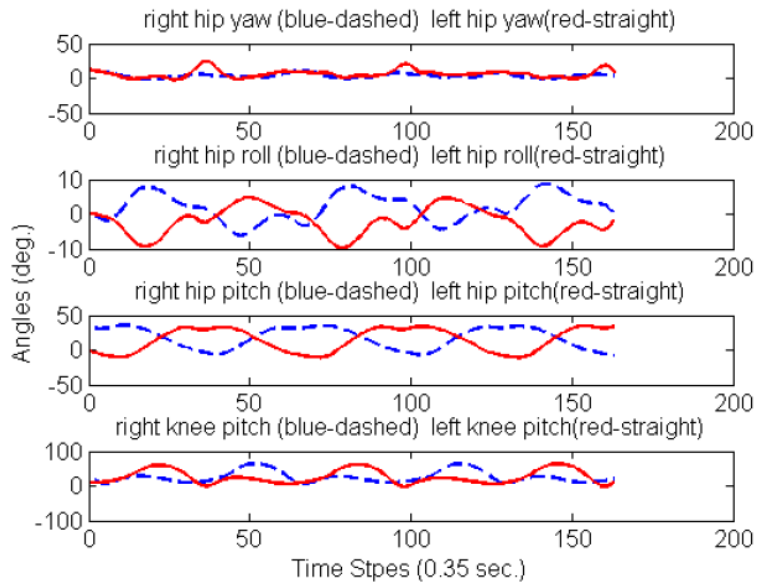
Figure 2.5: Joint angle variations during gait-part1
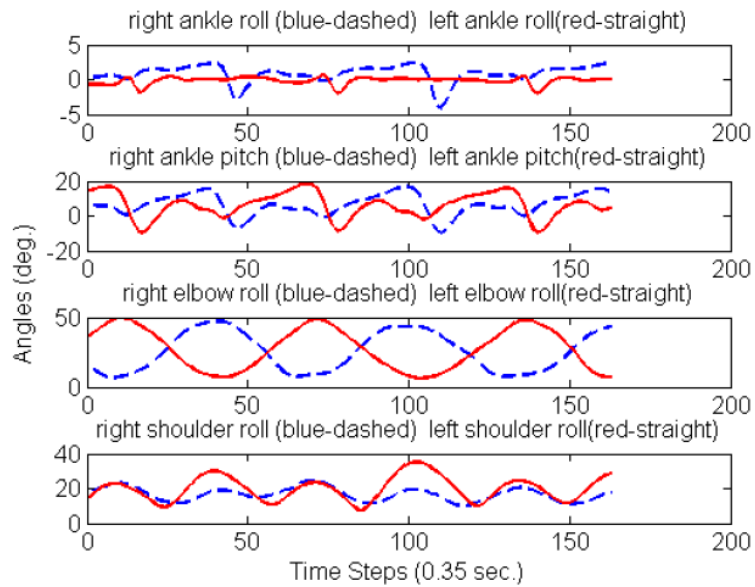
Figure 2.6: Joint angle variations during gait-part2

Chapter 3

State of the Art Humanoid Balance Techniques

Most humanoid balance systems to date focus on Zero Moment Point (ZMP) control [37]. ZMP is the contact point of the foot with the ground where the sum of horizontal inertia and gravity forces is zero [38]. This concept also applies to human behavior, however the difference lies in how posture is sensed.

3.1 Sensor Fusion

Few attempts have been made to take measurement noise into consideration while assessing balance. Mahboobin *et al.* [39] introduced a sensory reweighting mechanism in order to fuse vestibular and proprioceptive information. The reweighting scheme consists of two Kalman filters, each giving more preference to one sensor over the other (through Kalman gain changing).

Another work on sensory reweighting in humanoid fall avoidance involves the fusion of the gyro and accelerometer sensors which together constitute the vestibular system [9]. However, none of the previously mentioned systems includes vision. In fact, the first system that applies sensory reweighting of visual, vestibular and proprioceptive information was recently introduced by Klein *et al.* [40]. The visual information is obtained from optical flow analysis, while an adaptive Kalman filter calculates three gains depending on the noise covariance of each sensor [40]. Although vision is included in posture estimation, its role is limited to the distance separating the robot from the visual environment. Any change in this distance causes inaccurate posture estimation and thus a faulty control strategy. So, the system only functions in a predetermined environment. Another limitation lies in the fact that the system is not designed to cope with unpredicted visual changes such as blurriness or poor lighting conditions. Another approach that uses vision but without sensory reweighting is introduced by Mahani *et al.* [41], where stereovision is used to estimate the humanoid's

16

Center of Mass pose and the knee/knee-hip strategies are used for push recovery. This approach fully relies on vision, which makes it non-reliable in poor lighting conditions and in environments with blurry scenes.

The sensory reweighting systems mentioned above are all tested for small-angle swaying disturbances applied to the platform on which the humanoid is standing on. However, push disturbances differ from pure swaying in their magnitude and impulse-like behavior. In this thesis, the fall avoidance strategy is tested by applying a push force to the humanoid robot and recording its response in terms of ankle torques in addition to the swaying angles.

3.2   Model-Based vs. Model-Free

The basic approach to solve the humanoid fall avoidance problem is through modeling the humanoid as a linear inverted pendulum and controlling the ankle torque to maintain the upright standing position. The humanoid posture is estimated by the ankle displacement angle and angular velocity [3, 42, 43]. The control algorithm is based on a Virtual Model Control strategy that calculates the appropriate ankle torque needed to be applied after a disturbance. The main limitation of this approach is that it only allows fall avoidance in the sagittal plane and against low magnitude disturbances.

Humanoid quiet stance could also be maintained using the Capture Point technique, as illustrated by Pratt *et al.* [44]. The algorithm is based on the Zero Moment Point (ZMP), which is the location inside the support polygon where the applied moments are balanced by the ground reaction force and where the horizontal moments at the ground reaction point are zero [38]. In cases where the ZMP is a fictitious one (*i.e.*, it lies outside the humanoid's support polygon), a step is taken by the humanoid to avoid falling. The Capture Point strategy can be applied for disturbances in differently-oriented directions but its complexity lies in the modeling process of the humanoid and in the control of the stepping action when applied.

Humanoid fall avoidance is not always purely related to modeling. In recent years, compliant humanoids have been utilized to recover from disturbances and comply with voluntary movements [45]. Compliant humanoids have their joints specially manufactured to act in accordance with the disturbance instead of counteracting it as in traditional humanoids. The advantage of compliant humanoids is that it reduces calculation and modeling complexities as the joints absorb the external disturbances; however, it poses manufacturing difficulties [45]. In addition, this approach only solves the fall avoidance problem for a specific type of humanoids, thus making it inapplicable to a generic humanoid robot.

Literature in Kinesiology emphasizes the importance of proprioceptive information in evaluating posture and achieving balance [10]. Somatosensory information includes muscle activity, joint positions, and contact with the environment.

It is established [10] that proprioceptive information is responsible for roughly seventy percent of the balance control in humans. The proprioceptive sensors used in humanoid fall avoidance are the foot reaction force sensors. Traditionally, these sensors are used to detect foot rotation in tilt in order to adjust the ankle torques [46]. Byuon and Shon [46] use foot pressure sensors to help imitate the control of humanoid gait by tracing the Center of Pressure of the operator. However, the authors state that the linear inverted pendulum model is used to maintain balance in cases of unexpected instability. Another model-free approach is presented in the work of Grimes *et al.* [47] where mathematical and dynamic modeling are replaced by Bayesian learning networks. These networks estimate the proper joint positions and torques for maintaining stability by referring to experimental data obtained from tests done on human subjects performing similar tasks as the ones being done by the humanoid. This introduces two main limitations: the first one lies in the need to set up the learning network through significant experimentation prior to the application on the humanoid robot. In addition, the dynamic nature of the environments in which humanoids usually operate makes it difficult to cover all types of external disturbances while maintaining a balanced posture. This shows in the experimentation where the humanoid only performs predefined motion behaviors without applying any unexpected disturbances, which are not covered in the learning stage [47]. If machine learning techniques were to be used in changing environments and in the presence of disturbances, numerous scenarios should be accounted for. These cases include terrain types, possible loads carried by the robot, disturbance magnitude and point of application on the robot's body.

In order to mimic the human behavior in maintaining balance, a review of the proprioceptive role in human balance is presented next. Tanaka *et al.* [48] highlight the importance of foot pressure in evaluating human posture by showing the change in human swaying patterns with ageing [8]. As humans age, they tend to lose control of the toe muscle activity. This is directly correlated to inferior balance capability compared to young subjects especially during posterior swaying. On the other hand, elderly subjects were found to perform as well as younger ones in swaying activities involving the heel sensation and heel muscle activation, knowing that the heel area is not greatly affected by age. Kavounoudias *et al.* [49] argue that erect stance is a result of a co-processed input from the tactile and proprioceptive information in the foot sole and ankle muscles. Their experiments show that the location of the pressure peak on the foot sole is a direct indication of the stance state. The visual and vestibular roles are considered to be auxiliary to the proprioceptive role but the latter is understood to be the most substantial. The aim is to make use of the dominant characteristic of the proprioceptive sensors in balance control by applying it on a humanoid undergoing push force disturbances.

3.3 Humanoid Gait and Energy Minimization

Humanoid gait has been the subject of research over the past few decades. Kinesiology studies indicate that the human learns how to walk progressively until the age of 5 to 7 years [2]. A similar pattern can be seen in the field of robotics nowadays, as gait design is being developed and improved, yet at a relatively slow pace [2]. In their search for bipedal gait design, researchers find two main paradigms for bipedal walking. The first paradigm dates back to 1990, where T. McGeer introduced the idea of passive walking which relies solely on the body dynamics [50]. According to McGeer, a steady walking cycle can be sustained by a passive interaction of gravity and inertia [50]. The second paradigm is that of powered walking which is governed by the use of actuators. This paradigm is broader and could be branched into several sub-paradigms as will be described later. Bipedal balance is also essential in humanoid operation. Balance during quiet standing is achieved through multiple strategies [51, 3, 42, 43].

There are several approaches for bipedal gait in the field of robotics varying from pure kinematic and dynamic design to biomimetic and human inspired gait design. Harada *et al.* [52] use online planning of the humanoid's Center of Gravity (CoG) and Zero Moment Point (ZMP) to ensure a stable bipedal gait. The gait plan is done through finding the next CoG and ZMP position and calculating the proper humanoid joint angles to move the feet to the desired positions. Another approach relies on feedback control for angular momentum compensation during bipedal gait. However, this approach is directed more towards gait stability than gait design [53]. Moreover, capture points are also utilized for planning the humanoid's footsteps during gait in order to ensure balanced walking [54, 55]. The 3D linear inverted pendulum model is also widely used in bipedal gait design [35]. The gait cycle is categorized by two main phases which are the single support phase and the double support phase. So each cycle starts with a single support phase, followed by a double support phase and then another single support phase.

The previously mentioned approaches treat the bipedal system as a pure mechanical body, and the control strategies followed are low-level (at the actuator level). However, it is always useful to be inspired by a biological system that is close to the mechanical or robotic system that is to be controlled. In the case of bipedal gait, the biological reference is the human gait. The inspiration by humans is twofold. The first inspiration is at the anatomy level. This is shown in the compliant humanoid design, where the joints are built to mimic the human muscles and tendons. Compliant humanoids have their joints specially manufactured to be more flexible and act along disturbances as opposed to traditional humanoids. The advantage of compliant humanoids is that it reduces processing and modeling complexities as the joints absorb the external disturbances; however, it poses manufacturing difficulties [45, 56]. In addition, this approach introduces a new type of humanoid design without considering the fact that most commercial humanoids do not have compliant joints. Therefore, a more generic

approach for humanoid gait and balance control is still needed.

This leads to the second form of inspiration by the human body, which is the cognitive one. This approach is more of a bird's eye view of the hierarchy in human posture and movement control. According to the cognitivism theory, human posture and movement are a problem of information processing [57]. According to Collins and De Luca, movement and postural regulation consists of two mechanisms; open-loop and closed-loop. The open-loop mechanism applies for short term regulation of movements while the closed-loop is for planned long term movement regulations relative to a reference value. In contradiction to the linear inverted pendulum theory, the cognitivism theory states that each body segment is controlled relative to its own position in space and relative to the adjacent segments (limbs) [57]. Understanding human posture and movement control is essential for achieving better humanoid gait and posture. However, not all kinesiology concepts could be directly mapped and programmed on a humanoid.

In the search for theories in kinesiology that could guide the approach for humanoid gait, the concept of energy minimization strikes as a cornerstone for bipedal gait design. Carol Oatis, in the book on human movements, states that human motion is driven by the concept of energy minimization [58]. The theory states that whether in quiet standing or while walking, the human body tends to apply the least muscular effort and joint torques in order to save energy. This concept could be deployed in humanoid movement.

The concept of energy minimization is widely used for humanoid posture and movement control [59]. In this thesis, the use of energy-based control will guide the human-inspired bipedal locomotion synthesis.

3.4   Energy-Based Control Applied to Humanoids

Energy-based control is used in a wide range of applications ranging from power, to mechanical systems [60, 61, 62]. The main objective in these control strategies is to reach the target with minimum energy expenditure.

In the work of Howlett *et al.* [63], optimal speed control is applied on train trajectories; the energy cost function was designed to reduce fuel consumption. Optimal energy reduction was also implemented in [64] for speed control of a wind generation system, and in [65] for the problem of home automation and building environments, where the smart building is guided by a multi-agent control system to ensure user preferences with minimized energy expenditure.

Mechanical system control also relies on energy-based strategies as in [66], where the locomotion of a hexapod is controlled based on kinetic energy control. The energy function consists of the difference between the hexapod's actual kinetic energy and the desired kinetic energy. The focus on kinetic energy alone is motivated by the assumption that potential energy varies minimally during locomotion on a flat terrain. Energy-efficient control strategies also apply to other

real-time systems such as Dynamic Voltage Scaling systems [67] and autonomous flying quadrotors [68]. Manipulator control also benefits from energy-based control algorithms, where learning techniques are used to find the optimal joint configuration for specific tasks [69, 70, 71].

On the other hand, many studies exist in the field of Kinesiology on the characteristics of human gaits; drawing from these studies should provide insight for the design of controllers for humanoid robots. In [72] a hill-type human-like musculoskeletal model is used to control reaching positions and simple tasks by reducing muscular effort. The energy minimization in this case is focused on the muscular effort exerted during motion.

Energy-based control is not foreign to humanoid robotics: in the work of Nansai *et al.* [73], the Jansen walking robot used an energy function that served as a cost metric, and guided the robot's gait to enable energy-efficient locomotion.

3.5 Small-Scale Humanoid Gait

While the ZMP concept is the main framework that guides humanoid gait [54, 74], there has been an increased interest in energy-efficient bipedal gait generation during the past years [75, 76, 77]. The approaches range from energy-based control of simplified compass bipeds [78] to more complex seven-link models [79] including upper limb motion planning as described in previous sections. Considering the fact that the height of the biped's CoM undergoes small variations during locomotion, it is sometimes assumed to be constant. In this approach, the energy minimization is focused on shaping the biped's kinetic energy during gaits [80]. The fixed CoM height has led to the conventional bent-knee humanoid gait; however, a more comprehensive energy minimization technique includes the total mechanical energy of the bipedal system in motion planning [81] leading to optimal gaits in terms of energy expenditure [82, 83].

The main framework for bipedal locomotion has always been centered around mimicking the human walk [84, 85, 86]. The Linear Inverted Pendulum Model (LIPM) is the most utilized model to characterize the human walk, with the system being considered as a series of linear inverted pendulums with moving bases. Here, the tip of the stance foot is considered as the pendulum pivot [35]. More complicated models have been developed over the years to better represent the human walk, and map it to humanoid locomotion [87, 88]; however, the LIPM remains integral in characterizing bipedal walking, especially in the context of energy expenditure. Mimicking human walking is not limited to the choice of an appropriate model; instead, it could lie in the control strategy applied to achieve the planned motion [89, 90] or in the biped's mechanical design, such as in the use of compliant joints for disturbance absorption [86, 45].

The methods mentioned above have often led to stable bipedal gaits; however, a more energy-efficient behavior is yet to be achieved especially in small-scale
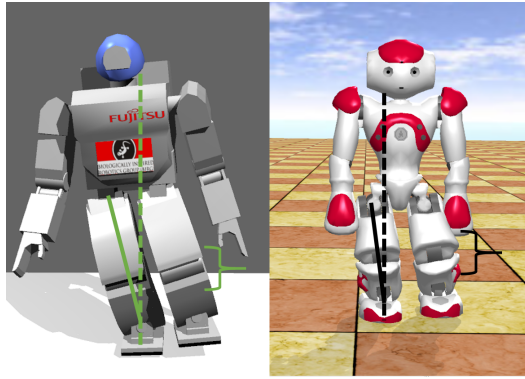
Figure 3.1: Hoap2 and Nao original gaits showing overbent knees and large lateral deviation during single stance

commercial humanoids with low degrees of freedom (DoFs). Fig. 3.1 shows Nao and Hoap2 humanoids during single stance of their walking cycle. These *low-knee* gait types apply the ZMP concept to ensure stability, but do not resemble human walking, neither visually nor mechanically. Low-knee gait applies excessive strain on the knee joints and extends the time of single stance, thus making the humanoid more vulnerable to disturbances during this part of the gait cycle. Moreover, the single stance phase involves large angle deviations in the lateral plane as depicted in the angle formed between the dashed and straight lines in Fig. 3.1. This increases the biped's vulnerability during single stance and raises the need for developing a human-like energy-efficient gait synthesis technique which can be applied to small-scale bipedal humanoid models to recover from external disturbances.

Chapter 4

Humanoid Push Recovery using Sensory Reweighting

4.1 Robot Model

In this section, the analysis is limited to the fall avoidance in the sagittal plane alone, accordingly, the humanoid is modeled as an inverted pendulum where the angle difference at the ankles is the control input and the ankle torque is the output. The robot model is shown in Fig. 4.1, where CoM is the humanoid's Center of Mass, a is the angular displacement of the ankle, L_0 is the distance from the foot to the ankle, L_L is the distance from the ankle joint to the CoM, D^+ is the distance from the foot base to the front tip, while D^- is the distance from the foot base to the foot's rear end, and β is the foot rotation angle.

In order to model the humanoid as a linear inverted pendulum, the following assumptions are made:

- The body is considered as a point mass located at the humanoid's center of mass (CoM).

- The focus is on the humanoid's motion in the sagittal plane.

- The humanoid's foot rotation angle with respect to the ground is β.

- The length from the humanoid's feet to its CoM is constant.

- The hip and knees are locked and the only torque applied is at the ankles.

4.2 Torque Control

The ankle strategy implemented on the humanoid is inspired by Jalgha *et al.* [3] whose work is an extension of the ankle strategy developed by Stephens [91]. The
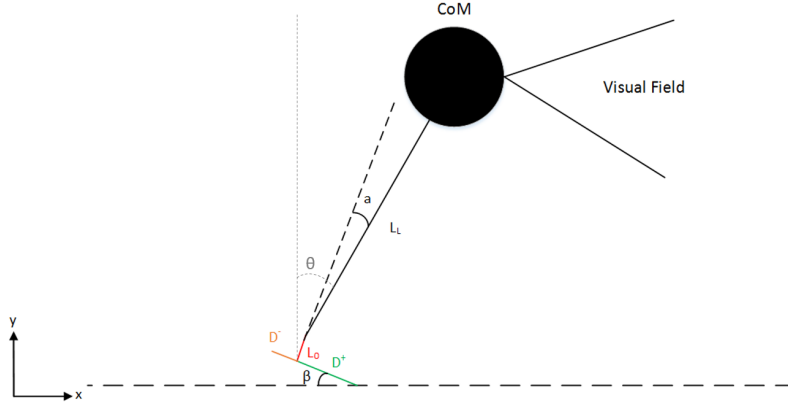
Figure 4.1: Humanoid robot modeled as a Linear Inverted Pendulum.

aim of our work is to improve the ankle strategy by following a more human-like assessment of the humanoid posture through sensor fusion. The control algorithm is that of a Virtual Model Control (VMC) which is based on attaching virtual components to a robot in order to control its behavior. The forces created by these mechanical components affect the torques applied on the corresponding actuators and in turn control the robot's movements. The VMC implemented on our humanoid consists of a virtual spring and dashpot system (connected in parallel) attached to the humanoid's CoM on one side and to a roller on the other as shown in Fig. 4.2. The parameters discussed in this section are defined in Table 4.1.

The transformation matrix that relates the world frame to the CoM frame of the humanoid is shown in (4.1), where D is either D^+, 0, or D^- depending on the position of the humanoid's foot [3]:

$$\mathbf{T} = \begin{pmatrix} s_{\beta+a} & -c_{\beta+a} & 0 & D - (Dc_\beta + L_0 s_\beta + L_L s_{\beta+a}) \\ -c_{\beta+a} & -s_{\beta+a} & 0 & -Ds_\beta + L_0 s_\beta + L_L c_{\beta+a} \\ 0 & 0 & -1 & 0 \\ 0 & 0 & 0 & 1 \end{pmatrix} \tag{4.1}$$

Since the humanoid is modeled as a linear inverted pendulum, a single inclination angle (θ) is considered which is the inclination of the CoM from the vertical line. The work is focused on the robot's motion in the sagittal plane, so θ could be derived from the x-y position of the robot's CoM taken from the last column of $\mathbf{T}$ in (4.1):

$$\theta = \arctan \frac{x}{y} = \arctan \frac{D - (Dc_\beta + L_0 s_\beta + L_L s_{\beta+a})}{-Ds_\beta + L_0 s_\beta + L_L c_{\beta+a}} \tag{4.2}$$

The Jacobian relating the joint torques to the virtual forces is found in (4.3):

Table 4.1: VMC parameters and their significance.

β	humanoid foot rotation angle
a	displacement angle at the ankles
D^+	distance between ankle and front tip of the foot
D^-	distance between ankle and back of the foot
L_0	distance between foot and ankle actuator
L_L	distance between ankle actuator and CoM
F_S	spring force
F_D	dashpot force
F_Y	vertical vertical force opposite to the gravitational force
K	spring constant
B	damping constant
L_C	$L_0 + L_L$
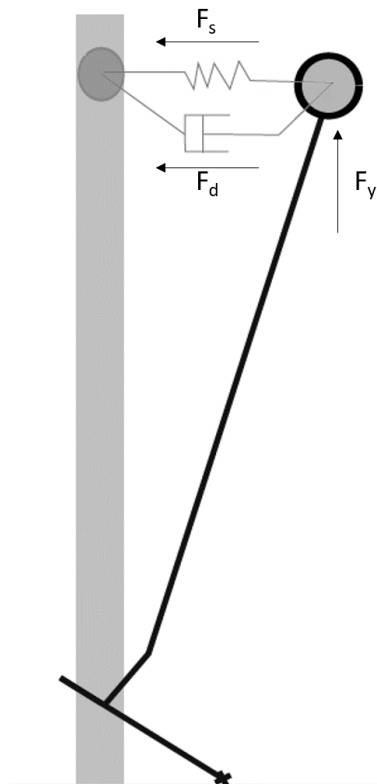
Figure 4.2: Humanoid robot model with virtual forces. [3]

$$\mathbf{J} = \begin{pmatrix} \delta x/\delta a \\ \delta y/\delta a \end{pmatrix} = \begin{pmatrix} -L_L c_{a+\beta} \\ -L_L s_{a+\beta} \end{pmatrix} \qquad (4.3)$$

Define the virtual spring and damper forces represented by F_S and F_D respectively. Both act in the x-direction and are summed up in F_X. Let the force F_Y cancel the effect of gravity. The virtual forces F_S, F_D, F_X, and F_Y are expressed in (4.4):

$$
\begin{aligned}
F_S &= Kx = K(D - (Dc_\beta + L_0 s_\beta + L_L s_{\beta+a})) \\
F_D &= B\dot{x} = B(\dot{\beta}(Ds_\beta - L_0 c_\beta) - (\dot{a} + \dot{\beta})L_L c_{\beta+a}) \\
F_X &= F_S + F_D \\
F_Y &= mg \\
\mathbf{F} &= \begin{pmatrix} F_X \\ F_Y \end{pmatrix}
\end{aligned}
\qquad (4.4)
$$

The torque applied at the ankle joints is calculated using the Jacobian property where the actuator torque is the product of the transpose Jacobian and the forces acting on the end effector, being the humanoid's center of mass in this case.

$$\tau = \mathbf{J}^T \mathbf{F} = -F_X(L_L c_{a+\beta}) - F_Y(L_L s_{a+\beta}) \qquad (4.5)$$

The torque in (4.5) is passed to the ankle joints to maintain stability. The presented approach only accounts for forces acting in the sagittal plane. The push recovery is therefore applicable in the sagittal plane against disturbances at the humanoid's CoM. In addition, the initial velocity of the CoM is not taken into consideration since the push recovery takes place at a uniform even terrain. In case the recovery is to be applied on changing terrains the initial velocity needs to be accounted for in relation to the push disturbance magnitude [92].

4.3   Pose Estimation using Monocular SLAM

In order to acquire visual information, a single camera is used to apply a Monocular SLAM (Simultaneous Localization and Mapping) algorithm developed by Davison *et al.* [93] in order to estimate the robot pose and angular velocity. The MonoSLAM algorithm consists of selecting landmarks from the visual scene of the robot and extracting features in the image. Tracking these features during camera movement, allows for motion estimation. The feature position and orientation estimation is calculated through an Extended Kalman Filter [93]. The feature detection is based on 1-point RANSAC (RANdom SAmple Consensus). The algorithm consists of detecting corners and following their motion between image frames. In addition, the uncertainty surrounding each estimated point is

calculated and considered when solving for the new state. According to [93], the camera state vector ($\boldsymbol{x}$) is:

$$\boldsymbol{x} = [\boldsymbol{r}\ \boldsymbol{q}\ \boldsymbol{v}\ w] \tag{4.6}$$

where $\boldsymbol{r}$ is the orientation vector, $\boldsymbol{q}$ is the orientation quaternion, $\boldsymbol{v}$ is the velocity vector, and ω is the angular velocity. The noise is assumed to be zero-mean Gaussian and applied as an acceleration noise. This leads to an impulse change in velocities. The noise vector is shown in (4.7):

$$\boldsymbol{n} = [n_{linear}\ \mathbf{n_{angular}}]^{\mathbf{T}} = [\gamma\mathbf{\Delta t}\ \alpha\mathbf{\Delta t}] \tag{4.7}$$

where γ and α are the unknown linear and angular acceleration respectively. The updated elements of the camera state vector are shown in (4.8-4.11):

$$\mathbf{r_{updated}} = \mathbf{r} + (\mathbf{v} + \mathbf{n_{linear}})\mathbf{\Delta t} \tag{4.8}$$

$$\mathbf{q_{updated}} = \mathbf{q} \times \mathbf{q}((\omega + \mathbf{n_{angular}}))\mathbf{\Delta t} \tag{4.9}$$

$$\mathbf{v_{updated}} = \mathbf{v} + \mathbf{n_{linear}} \tag{4.10}$$

$$\omega_{updated} = \omega + n_{angular} \tag{4.11}$$

Using the above values, the robot's change in angular position and velocity are deduced in order to estimate its posture. Therefore, vision is used as a position and velocity estimator independent of the environment in which the robot is operating. It is important to note that poor lighting conditions and blurriness will affect the estimation. However, those two factors are taken into consideration in the final system.

The MonoSLAM code returns the robot's state as a quaternion; however this application requires the humanoid's pitch angle only since the focus is on the sagittal plane. Given a rotation matrix $\mathbf{R}$, the pitch angle (θ) in radians is calculated using (4.12) [93]:

$$\theta = \arctan \frac{-\mathbf{R}(2,0)}{\sqrt{\mathbf{R}^2(2,1) + \mathbf{R}^2(2,2)}} \tag{4.12}$$

While visual feedback enhances the fall avoidance strategy, the quality of the acquired images has an effect on the pose estimation. For this reason it is important to take image quality into consideration. Two metrics are assessed at each frame and their values affect the error covariance of the Kalman Filter. The blur metric is calculated by blurring the image both horizontally and vertically followed by calculating the difference between the blurred image and the original one [94]. The horizontal and vertical filters used to blur the image frames are

shown in (4.13). The idea behind this algorithm is that when starting with a blurry image, adding blurriness will not have a difference between the original and the updated one [94]. This way the blur factor of the visual scene can be determined. The blur metric is a value between 0 and 1, where 0 indicates a perfectly sharp image and 1 indicates a fully blurred image [94].

Another important factor that affects image quality is the brightness metric. This is analogical to the human case where the dependency on vision decreases in dark environments. The brightness is calculated by taking the mean of the *Value* matrix[1] of the image in *HSV* (Hue-Saturation-Value) format. The brightness metric is also normalized where 0 means totally dark and 1 means fully bright. The desired blur factor is a value close to 0, while the optimum brightness factor is around 0.5 (midway):

$$H_{hor} = 1/9\begin{pmatrix} 1 & 1 & 1 & 1 & 1 & 1 & 1 & 1 & 1 \end{pmatrix} \qquad H_{ver} = H_{hor}{}^T \qquad (4.13)$$

4.4 Sensory Reweighting System

The overall system consists of three main blocks; robot angle and angular rate estimation (using vision and gyroscope), Kalman filter, and torque controller (see Fig. 4.3). The vision pose estimation was discussed in the previous section and the angular velocity is directly measured using the gyroscope of the Nao humanoid robot.

The Kalman Filter is used to fuse the camera and gyroscope measurements and come up with a better estimate of the humanoid's pose. The state space model of the system is presented in (4.14):

$$x_n = \mathbf{A}x_{n-1} + \mathbf{B}u_n + \omega_n$$
$$y_n = \mathbf{C}x_n + v_n \qquad (4.14)$$

$$x_n = \begin{pmatrix} \theta \\ \dot{\theta} \end{pmatrix} \quad \mathbf{A} = \begin{pmatrix} 1 & \Delta t \\ \frac{g}{L} & \Delta t \end{pmatrix}$$
$$\mathbf{B} = \begin{pmatrix} 1 \\ \frac{1}{mL^2}\Delta t \end{pmatrix} \quad \mathbf{C} = \begin{pmatrix} 1 & 0 \\ 0 & 1 \end{pmatrix}$$

where x_n is the current state vector, u_n is the input vector, and y_n is the measurement vector. The process and measurement noise vectors are represented by w_n and v_n respectively. The process noise covariance matrix ($\mathbf{Q}$) and the

---

[1]The Value matrix represents the intensity (brightness) of each pixel in the image.
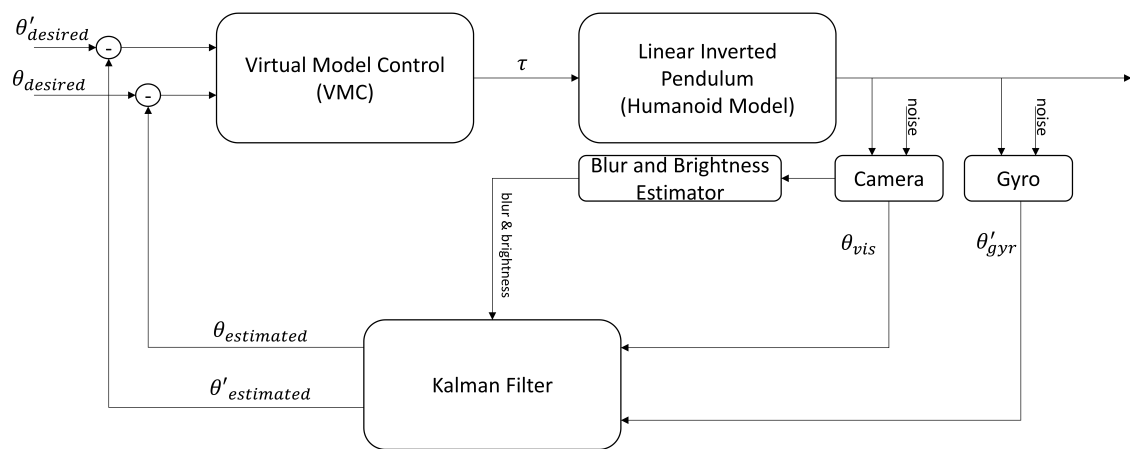
Figure 4.3: Control Loop of the overall system. The visual and gyro measurements are subjected to noise. The Kalman Filter fuses the measurements along with the blur and brightness metric and sends the predicted angular position and velocity to the Virtual Model Controller which in turn sends the appropriate ankle torque (τ) in order to maintain postural balance.

measurement noise covariance matrix ($\mathbf{R}$) are shown below:

$$\mathbf{Q} = \begin{pmatrix} 0 & 0 \\ 0 & \sigma_\omega{}^2 \end{pmatrix} \quad \mathbf{R} = \begin{pmatrix} \sigma^2{}_\theta & 0 \\ 0 & \sigma^2{}_{\dot\theta} \end{pmatrix}$$

The process noise standard deviation is σ_ω, while the visual and gyro measurement noise standard deviations are σ_θ and $\sigma_{\dot\theta}$ respectively. The blur and brightness factors introduced in the previous section, are integrated into the measurement noise covariance update as shown in (4.15). Since the blur and brightness factors are only related to the visual information, their values are used to update the first element of the measurement noise covariance matrix $\mathbf{R}$. The idea behind this equation is that the worse the brightness or the blur metric is the more weight is given to the difference between the old and the new covariance matrices. In the ideal case, where $bl = 0$ and $br{=}0.5$, no weight is given to the difference as the measurements are considered to be reliable:

$$\mathbf{R_n(1,1)} = \mathbf{R(1,1)} + (bl + |br - \mathbf{0.5}|/\mathbf{2}) * (\mathbf{R(1,1)} - \mathbf{R_{n-1}(1,1)}) \qquad (4.15)$$

In order to give time for the sensor information to be reliable, $\mathbf{R}$ is initialized to be $\mathbf{R_0 = 5R}$.

4.5   Experimental Setup

The MonoSLAM algorithm is tested alone prior to conducting the seven experiments. The MonoSLAM demonstration is shown in Fig. 4.4. The four frames are part of a robot's pitch motion from $0°$ to $9.4°$ with a velocity of about $1.5°/s$. The estimated pitch angle using MonoSLAM was correct to within an error $0.03°$.

It is noticeable in Fig. 4.4 that in the first frames, few features are detected and most of them represent corners in the scene. The corners are usually the most reliable features in an image, since tracking them is much easier than tracking edges [95]. The humanoid used for experimenting is the Nao H25 V3.3, a product of Aldebaran Robotics (see Fig. 4.5). Nao is 57.3 cm tall and weighs 5.4 kg. The robot is equipped with a 2-axis gyroscope with 5% precision [96], which is used to measure the angular velocity. Although Nao is equipped with two cameras, there is no common field of view between them and thus no stereo vision can be done. A Microsoft LifeCam HD (mounted on the head of the robot) is used to get better image quality. The Nao robot doesn't permit torque control natively, so the calculated torque was used to control the ankle motors' stiffness which is feasible on Nao.

The push recovery algorithm is written in C++ running on Ubuntu 12.04. The humanoid robot is set to stand in an upright position with the webcam strapped to its face. The Nao robot is also tied to a linear guide for safety. This
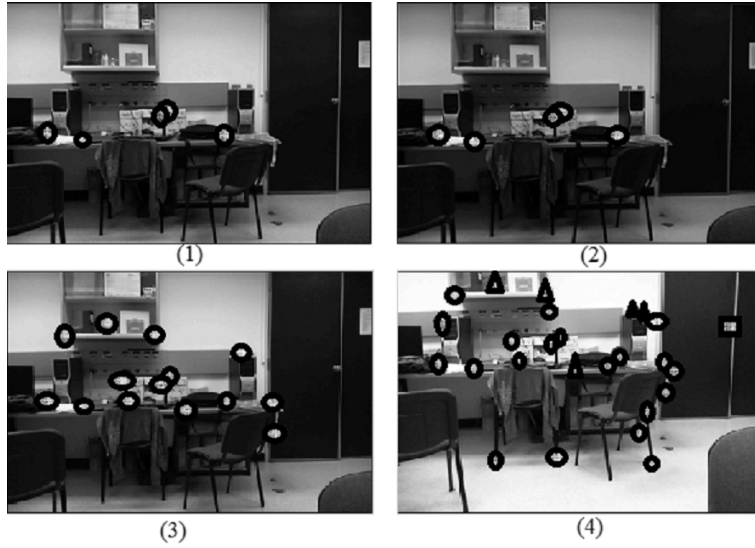
Figure 4.4: Frames from a camera with MonoSLAM run on MATLAB. The detected features increase with the number of frames; however some of the new features are not very certain (triangles and squares).

guide is frictionless and doesn't affect the humanoid's movement. It only protects the robot in case the fall avoidance algorithm fails. The reason behind resorting directly to experiments instead of simulation is due to the difficulty in simulating the MonoSLAM algorithm in Webots.

In order to get a consistent push force for all trials the humanoid is hit by a ball hanging from a rope and released at a predetermined angle. The experimental parameters are listed below.

- rope length is 76 cm

- distance between robot's back and projection of the ball is 40 cm

- height at rest (between bottom of the ball and ground) is 23 cm

- angle of release (with respect to the normal) is 45°

- ball weight is 425.85 g

- ball diameter is 21.804 cm

After 100 trials using the above mentioned setup, the average force (measured using the OMEGA digital force sensor) at the back of the Nao robot is 56.095N with a standard deviation of 2.697N. The 95% confidence interval for the applied force is in the range of 52.0 and 61.2N. The statistical data is obtained by placing the force sensor at the impact point and repeating the trials. The system is shown in Fig. 4.5.

Figure 4.5: The whole system is shown in this figure. The humanoid and camera are connected to the laptop running C++ and python code.

4.6 Results and Analysis

The experiment is conducted in seven different scenarios each repeated ten times, in order to test the robustness and improvement the sensory reweighting gives in push recovery. The scenarios are:

1. Gyro and camera integrated for push recovery under normal conditions

2. Gyro alone for push recovery under normal conditions

3. Noisy gyro measurements integrated with camera

4. Noisy gyro without camera integration (no reweighting)

5. Camera only under normal conditions

6. Camera and gyro in a dark environment (lights out)

7. Camera only in a dark environment (no reweighting)

The following sections present comparisons between the different scenarios which highlighting the superiority of the sensory reweighting system. The average angle displacements (obtained from Nao's IMU) and ankle torques taken across trials are compared for the seven scenarios. It is important to note that the recovery algorithm is applied on Nao's ankle joints and that all of its other joints are locked. In fact, since the algorithm is only applied in the sagittal plane, only Nao's pitch ankle motors are controlled.

Figure 4.6: Angle displacement plots using Sensory reweighting (red) and Camera alone (blue) for a 56 N push force under normal conditions.

4.6.1 Sensory reweighting vs vision alone (under normal conditions)

The experiment described above is conducted both when sensory reweighting is applied and when the camera is used alone. The tests are done under normal conditions. The angle displacement and ankle torque plots are shown in Fig. 4.6 and Fig. 4.7 respectively. It is clear that sensory reweighting leads to a lower angle displacement (peak of 0.33 rad.) compared to 0.42 rad when only vision is used. In addition, sensory reweighting improves the settling time by 9.3% (1.17 sec. compared to 1.29 sec.). As for the applied ankle torque during the fall avoidance strategy, sensory reweighting requires the application of 1.5 N while vision alone requires a peak of 2.14 N. The results show the superiority of sensory reweighting over using vision alone.

4.6.2 Sensory reweighting vs gyro alone (under normal conditions)

In this section, the sensory reweighting results are compared to the case where the gyro is used alone. The angle displacement and ankle torque plots are shown in Fig. 4.8 and Fig. 4.9 respectively. Although using gyro alone leads to a lower angle displacement (peak of 0.17 rad.), this method has a poor settling time (1.95 sec.) compared to the sensory reweighting method. Sensory reweighting is also superior in terms of the maximum applied torque (1.5 N) compared to 3.75 N

33
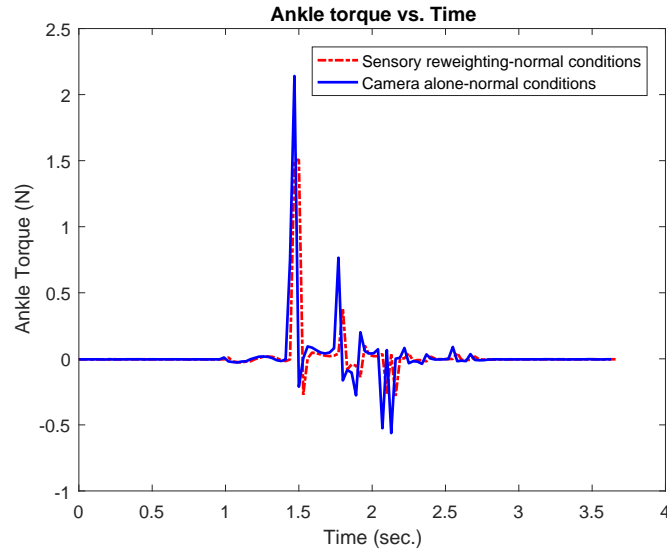
Figure 4.7: Ankle torque plots using Sensory reweighting (red) and Camera alone (blue) for a 56 N push force under normal conditions.

applied when gyro is used alone. This comparison also indicates the improvement introduced by relying on both gyro and camera measurements.

4.6.3 Sensory reweighting vs vision alone (lights out)

The sensory reweighting system is tested against a scenario where only the camera is used to estimate the humanoid's posture. This test is performed in a dark environment. The angle displacement and torque plots are shown in Fig. 4.10 and Fig. 4.11 respectively. It is clear that using a camera alone to assess posture is problematic. This is shown in the angle displacement plot where the estimated angle is zero during to the whole strategy which leads to a negligible torque applied at the ankle joints. As a result, the humanoid is unable to recover from the push and falls down. On the other hand, when sensory reweighting is used, the humanoid relies more on the gyro measurement and is able to successfully recover from the push.

4.6.4 Sensory reweighting vs gyro alone (with added gyro noise)

In this comparison, a zero-mean Gaussian noise with a unit standard deviation is applied to the gyro measurements and the performance of the sensory reweighting system is tested against a gyro-only system. The angle displacement and torque plots are shown in Fig. 4.12 and Fig. 4.13 respectively. The sensory reweighting

34

Figure 4.8: Angle displacement plots using Sensory reweighting (red) and Gyro alone (blue) for a 56 N push force under normal conditions.
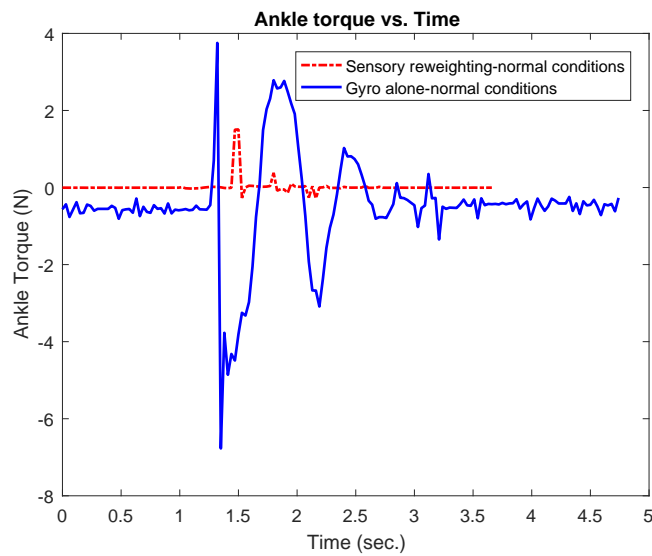
Figure 4.9: Ankle torque plots using Sensory reweighting (red) and Gyro alone (blue) for a 56 N push force under normal conditions.
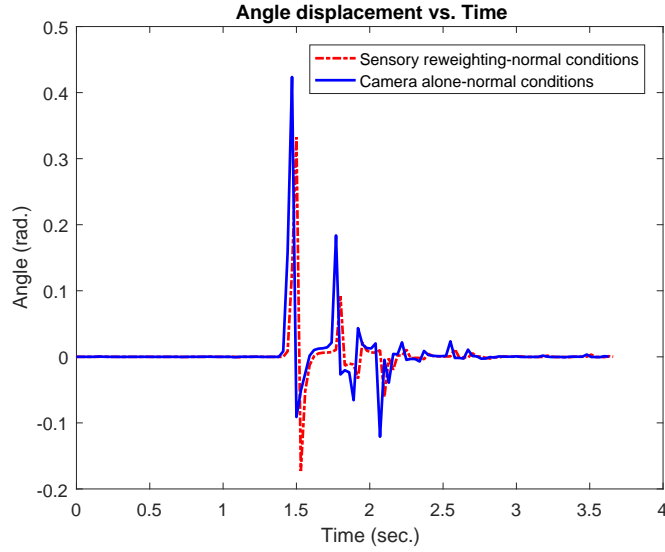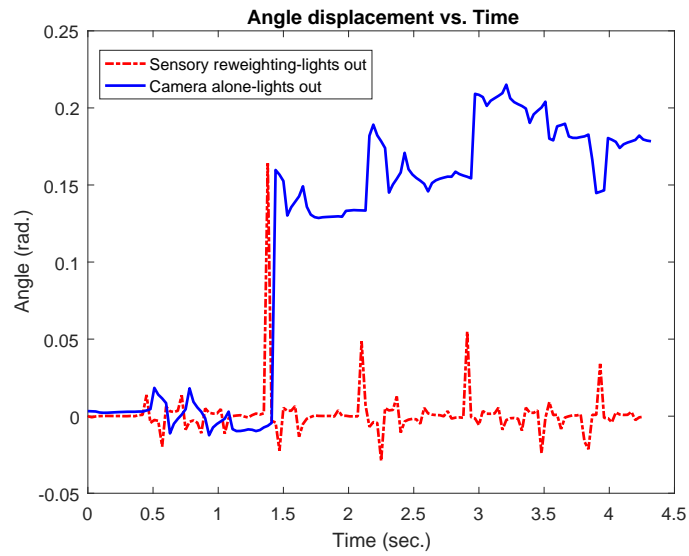
Figure 4.10: Angle displacement plots using Sensory reweighting (red) and Camera alone (blue) for a 56 N push force in a dark environment.
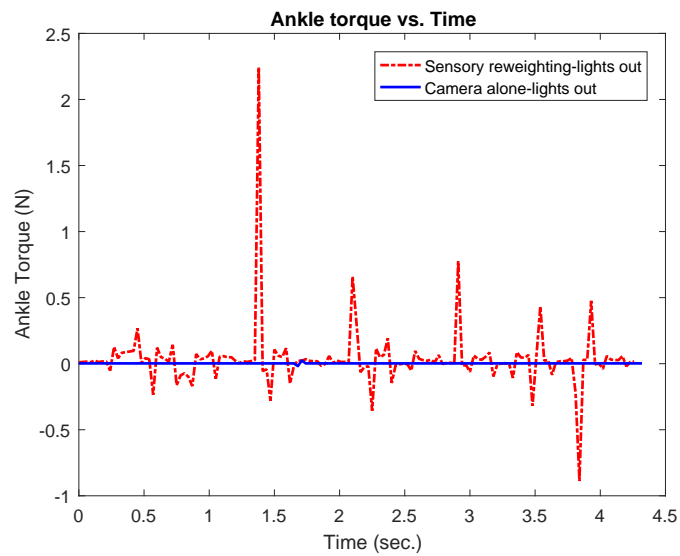
Figure 4.11: Ankle torque plots using (red) Sensory reweighting and Camera (blue) alone for a 56 N push force in a dark environment.
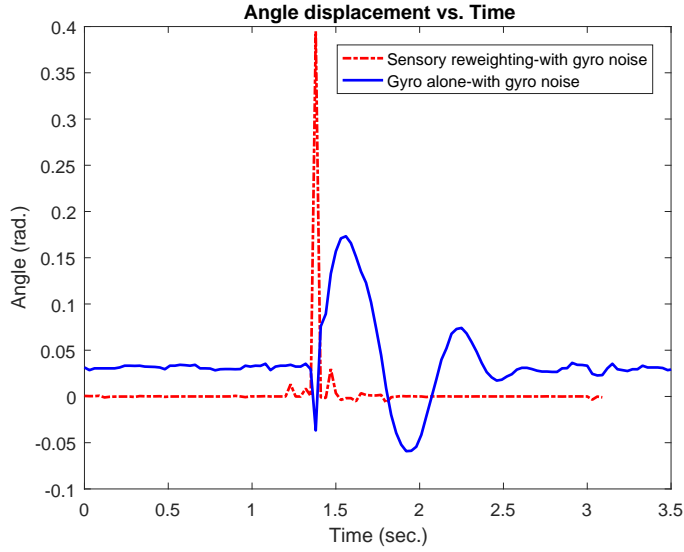
Figure 4.12: Angle displacement plots using Sensory reweighting (red) and Gyro alone (blue) for a 56 N push force when gyro noise is added.

system proves superior in terms of settling time (0.36 sec.) compared to 1.98 sec. when using gyro alone. However, the gyro-only method leads to smaller angle displacement (a peak of 0.17 rad.) while the sensory reweighting system requires a greater angle (0.39 rad.). The sensory reweighting system proves to be more energy-efficient since it requires the application of an ankle torque only for a short period of time, while in the gyro-only system a torque is always applied at the ankle joints which might lead to overheating if the strategy is applied for long periods of time. The average values of the performance parameters (across the 10 repetitions) of the different scenarios are summarized in Table 4.2.

In order to test the robustness of the sensory reweighting algorithm against gyroscope noise, the experiment is also conducted with double the magnitude of the Gaussian noise (with zero-mean) added to the gyroscope measurements. Under high magnitude noise sensory reweighting improves the maximum swaying angle by 17.47% and requires less overall torque than when the gyroscope measurements are used alone (see Fig. 4.14). Despite the fact that when the gyroscope measurements are used alone 60.96% less maximum torque is required to recover, the peak torque is only applied for 0.18 seconds while ankle torque is always applied in the 'gyro alone' approach (see Fig. 4.15).

Sensory reweighting improves fall avoidance in terms of applied ankle torque, angle displacement, and settling time. Referring to Table 4.2, it is clear that sensory reweighting ensures lower settling time when compared to the same scenario without reweighting. In Scenario 4, the maximum ankle torque applied is 6.44N while in Scenario 5, the value is 2N. These values may lead us to think
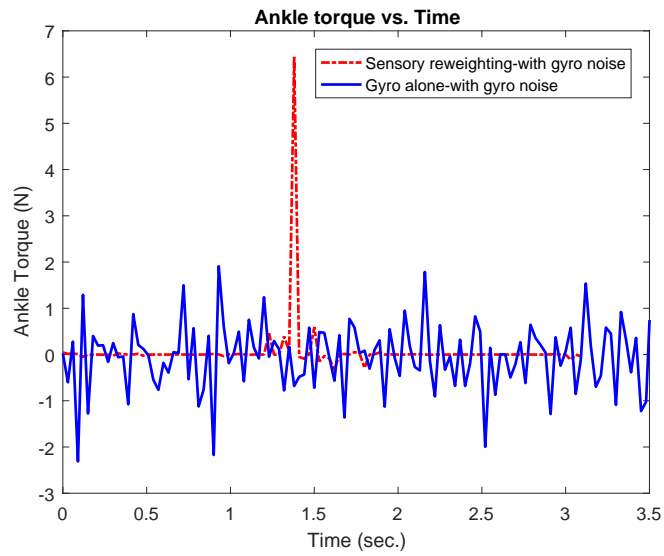
Figure 4.13: Ankle torque plots using Sensory reweighting (red) and Gyro alone (blue) for a 56 N push force when gyro noise is added.

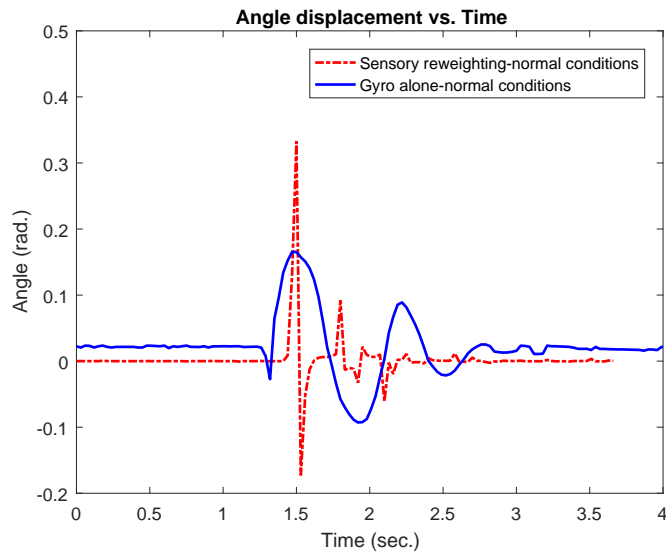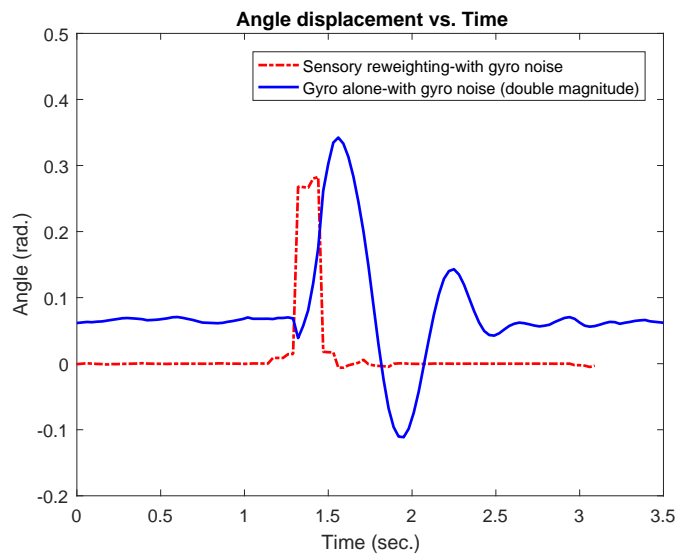Figure 4.14: Angle displacement plots using Sensory reweighting (red) and Gyro alone (blue) for a 56 N push force when a double magnitude gyro noise is added.
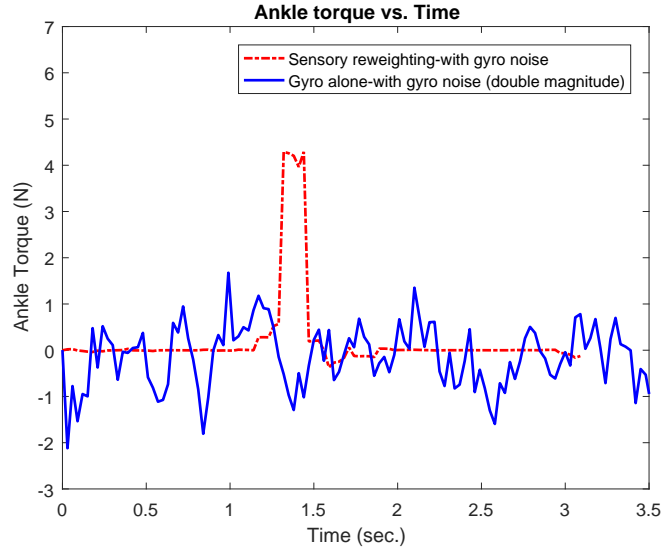
Figure 4.15: Ankle torque plots using Sensory reweighting (red) and Gyro alone (blue) for a 56 N push force when a double magnitude gyro noise is added.

that using gyro alone might be more efficient. However, sensory reweighting applies the torque for a short period of time (just after the push force is applied), but when gyro is used alone the torque is applied during the whole experiment time. This proves, that despite applying a higher torque, the sensory reweighting algorithm proves to be more efficient. The same reasoning applies for the angle displacement, where in some scenarios the maximum angle displacement is higher when using sensory reweighting. The higher angular displacement leads to a faster recovery which is shown in the low settling time in the sensory reweighting scenarios. Therefore, sensory reweighting leads to a faster, more robust, and more efficient humanoid fall avoidance.

When compared to the results in [3], the perturbations applied to Nao are of higher magnitude than the ones in [3]. However, the robot model is of different dimensions and the recovery assessment is of different nature. Also, the push recovery assessment metrics are of a different nature. The metrics used are based on the angle variation per second, while in this approach the impulse force is measured at the moment of impact.

Table 4.2: Performance parameters for the 7 scenarios (maximum torque, maximum displacement angle, and settling time)-Values are averages of the 10 repetitions

Scenario Number	Max. Torque (N)	Max. Angle Displacement (rad.)	Settling Time (sec.)
(1) Sensory Reweighting (normal conditions)	1.50	0.33	1.17
(2) Gyro alone (normal conditions)	3.75	0.17	1.95
(3) Camera alone (normal conditions)	2.14	0.42	1.29
(4) Sensory Reweighting (noisy gyro)	6.44	0.39	0.36
(5) Gyro alone (noisy gyro)	2.00	0.17	1.98
(6) Sensory Reweighting (lights out)	2.24	0.16	2.41
(7) Camera alone (lights out)	0.06	No recovery	No recovery

Chapter 5

Model-Free Humanoid Push Recovery

In this chapter, a model-free system for humanoid push recovery is presented. The concept is inspired by human proprioceptive sensory input used for detecting balance disturbances.

5.1 Humanoid Posture Estimation

The sensors used to measure foot pressure are Force Sensitive Resistors (FSRs). Each foot has two front and two rear sensors as can be seen in Fig. 5.1. The eight FSRs have a working range from 0N to 25N. Since the proposed algorithm is model free, the posture estimation is calculated solely through the difference between the front and rear sensors (for balance in the sagittal plane) and between the right and left sensors of each foot (for balance in the lateral plane).

For each foot, the equivalent FSR values in the sagittal and the lateral planes at iteration i are calculated by summing the front/back and right/left FSR values respectively for each foot. In order to minimize the effect of noise, a weight is given to the readings of the previous iterations by using a low pass filter.

The model-free approach presented in this section provides the humanoid with increased versatility and adaptability to changes in terrain inclination. It also aids in maintaining balance under the effect of external disturbances even when the humanoid carries a load.

5.2 Controller Design

The controllers used to maintain the humanoid's upright posture are two independent Proportional Integral Derivative (PID) controllers at the humanoid's ankle joint. One controller maintains balance in the sagittal plane by controlling the ankles' pitch angles, while the other maintains balance in the lateral plane by
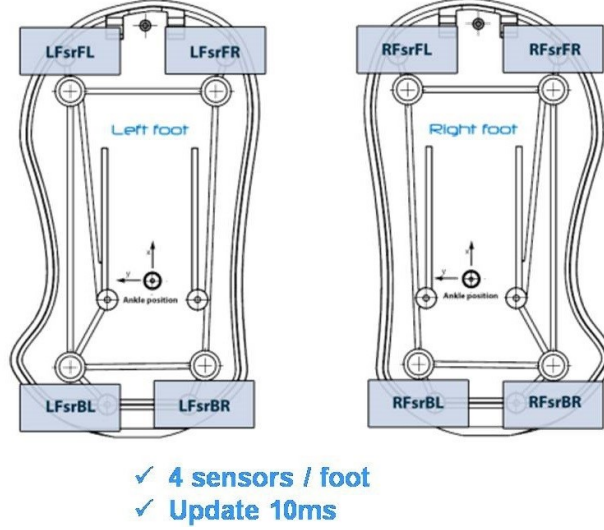
Figure 5.1: Force Sensitive Resistors.

controlling the roll angles. The errors fed to the sagittal and lateral PID Controllers are the difference between the front and back FSR values and the right and left FSR values respectively.

As a result, the proportional, integral, and differential terms for the pitch and roll ankle controllers are shown in (5.1)-(5.3) and (5.4)-(5.6) respectively, where K_p is the proportional gain, K_i is the integral gain, and K_d is the differential gain. The error between the FSR readings in the sagittal and lateral planes at iteration i are represented by $e(i)_{sagittal}$ and $e(i)_{lateral}$ respectively and Δt is the time step. The PID controller gains are obtained in simulation using the Ziegler-Nichols method as a starting point. The gains are then tuned manually to improve performance.

$$P_{sagittal} = K_p * e(i)_{sagittal} \tag{5.1}$$

$$I_{sagittal} = K_i * \Sigma e(i)_{sagittal} * \Delta t \tag{5.2}$$

$$D_{sagittal} = K_d * (e(i)_{sagittal} - e(i-1)_{sagittal})/\Delta t \tag{5.3}$$

$$P_{lateral} = K_p * e(i)_{lateral} \tag{5.4}$$

42
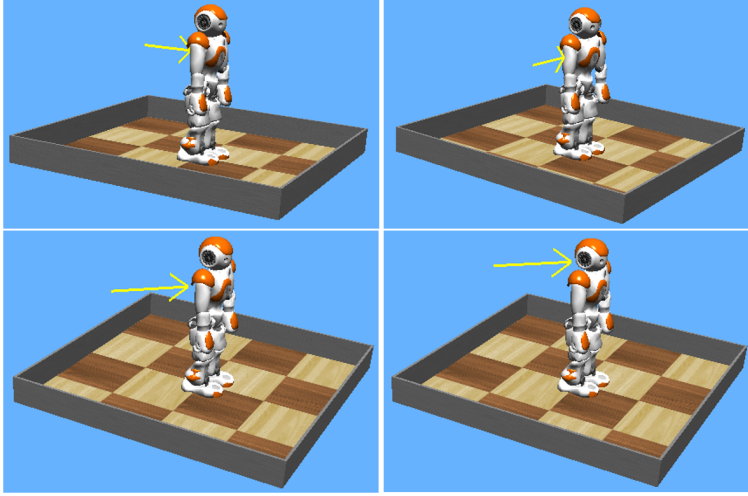
Figure 5.2: Summary of simulation scenarios

$$I_{lateral} = K_i * \Sigma e(i)_{lateral} * \Delta t \qquad (5.5)$$

$$D_{lateral} = K_d * (e(i)_{lateral} - e(i-1)_{lateral})/\Delta t \qquad (5.6)$$

The pitch and roll control inputs are calculated for each time step as shown in (5.7) and (5.8).

$$Pitch = (P_{sagittal} + I_{sagittal} + D_{sagittal}) * \Delta t \qquad (5.7)$$

$$Roll = (P_{lateral} + I_{lateral} + D_{lateral}) * \Delta t \qquad (5.8)$$

5.3   Simulation and Experiments

In order to compare the model-free and model-based approaches, a unified setup was developed in Webots. The Nao humanoid is subjected to push forces from different directions and at different locations of its body (see Fig. 5.2). The performance is evaluated by measuring the swaying angle of the Nao in response to the push.

Before comparing the results under the different scenarios it is important to describe the model-based strategy to which the proposed method is compared. The ankle strategy developed by Stephens [91] and then expanded by Jalgha for rotational state variables in [3] models the humanoid as a linear inverted pendulum and assumes that the disturbances are always applied at the humanoid's center of mass. The model is shown in Fig. 5.3, where CoM is the humanoid's
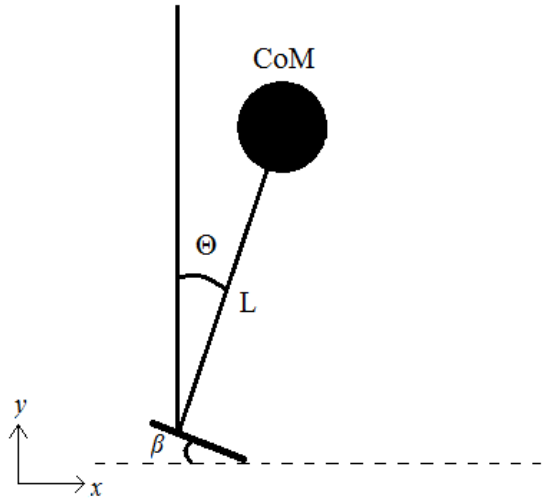
Figure 5.3: Humanoid modeled as a linear inverted pendulum

Center of Mass, θ is the angular displacement of the ankle, L is the distance from the foot to the CoM, and β is the foot rotation angle. In order to apply this model to the humanoid, the following assumptions are made:

- The body is considered as a point mass located at the humanoid's center of mass.

- The humanoid's foot rotation angle with respect to the ground is β.

- The length from the humanoid's feet to its CoM is constant.

- The hip and knees are locked and the only torque applied is at the ankles.

Therefore, the posture is assessed by measuring the angular displacement and velocity of the humanoid's CoM, and applying the appropriate torque at the ankles to counteract this displacement. The control approach is based on the Virtual Model Control concept in which the humanoid's CoM is considered to be attached to a virtual spring and damper. The controller parameters for the model-based approach are the spring and damper gains as opposed to the PID controller in the model-free approach.

In the Webots simulator, the angular displacement and velocity of the CoM are measured using an Inertial Measurement Unit (IMU) which is also found on the actual Nao humanoid. However, applying the torque directly to the ankle motors is only possible in the simulator whereas this element can't be controlled in the actual humanoid. This introduces a key advantage of our model-free approach

since the control is on the angular displacement of the ankles instead of torques; a feature available in the simulator as well as in the actual implementation. However, in the experiments shown in the following section a workaround was used in order to implement the model-based approach. The torque is transformed to stiffness which is an input that could be controlled on the actual Nao.

One solution that might be suggested for push recovery during quiet standing is to set all joints to maximum stiffness at all times. However, this solution has two main disadvantages that render it inapplicable. The first and most important limitation is that setting the joint motors at full stiffness leads to overheating and permanent damage when applied for long periods of time. The second disadvantage is that full stiffness eliminates any degree of compliance to absorb push disturbances and leads to rotation around the feet edges specially when the push is applied in the direction facing the humanoid. This decreases the degree of tolerance to high disturbance magnitudes.

The simulation consists of a Nao humanoid standing in the upright position and experiencing a push from different directions with different magnitudes. The push force is created using a physics plugin in Webots and is analogous to an actual push or bump that the humanoid may encounter during its normal operation. The scenarios used as a benchmark to compare the model-free approach against the model-based one can be distinguished into four categories (see Fig. 5.2).

- Push at CoM in the sagittal plane

- Push at CoM in the lateral plane

- Push at CoM with two components (in both planes)

- Push not at CoM with two components (in both planes)

5.3.1 Simulation Results and Analysis

The previously mentioned scenarios are tested in Webots and the compared results are analyzed in the following subsections. It is important to note that the controller parameters for the model-based approach are tuned to get the least displacement and fastest settling time.

Push at CoM in the Sagittal Plane

In the sagittal plane, the model-based control was able to withstand a push force of magnitude 24N, beyond which the humanoid would fall down. However, the model-free approach enabled the humanoid to withstand a push of magnitude 25N. Although a 1N improvement seems small, the disturbance rejection range
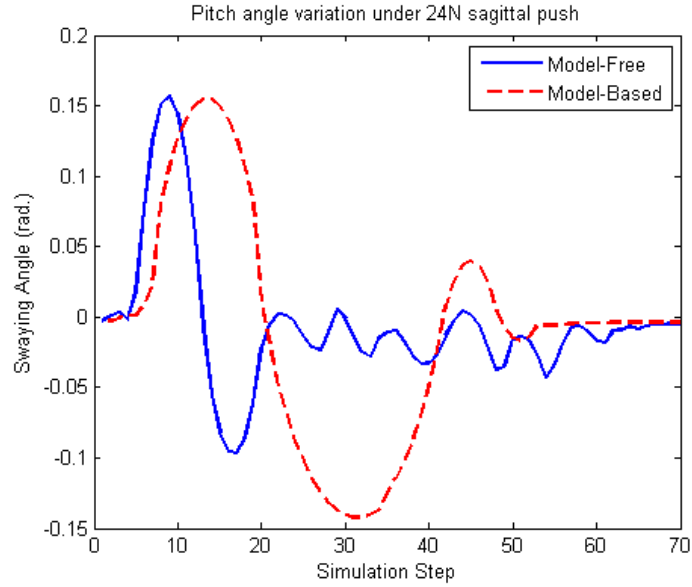
Figure 5.4: Pitch angle variation under 24N push in the sagittal plane - simulation

of the ankle strategy is limited so any improvement in this area is considered significant.

In order to compare the two approaches, a plot showing the pitch angle variation during and after the disturbance was applied is shown in Fig. 5.4. It is clear that the response in the model-free approach is faster than that in the model-based controller. The peak swaying angle of the model-free approach is greater by 0.0025 rad than that of the model-based. However, the model-free approach provides an improved undershoot by 0.04568 rad and a reduced swaying interval. Although, the model-free approach shows perturbations, these are limited between 0.0058 and 0.0436 rad between simulation steps 20 and 50, the model-based approach shows a large sway during the same interval.

The roll angle swaying under the influence of the same disturbance is shown in Fig. 5.5. It is expected that the model-based approach doesn't experience any swaying in the roll angle because no torque is applied to that motor. However, this is only the case when the disturbance is applied perfectly in the sagittal plane. Examining the model-free behavior, the swaying ranges between 0.01 and -0.01 rad that could be traced back to noise in the FSR readings and that the humanoid's feet are not well settled on the ground. In fact, these steady state oscillations don't exist in the experimental testing.
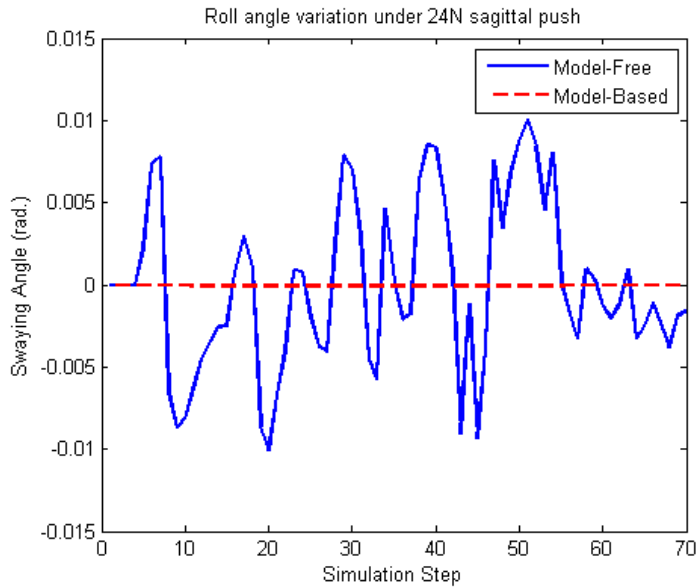
Figure 5.5: Roll angle variation under 24N push in the sagittal plane - simulation

Push at CoM in the Lateral Plane

In this scenario, the push force is applied in the lateral plane to test the roll angle sway in response to the disturbance. The maximum magnitude that the model-based controller is able to handle is 24N while the model-free handles 26N push forces. The two approaches under study are tested against a 24N push to compare their responses. In order to check the maximum angle sways that could be handled by both methods, the roll angle variations are shown in Fig. 5.6. It is shown that the model-free controller undergoes a peak sway of 0.11 rad compared to 0.14 rad in the model-based approach.

As for the pitch angle swaying (see Fig. 5.7), the values for both approaches are negligible which is logical since the disturbance is acting purely in the sagittal plane.

Push at CoM with Two Components (one in each plane)

The humanoid is subjected to a push having two components, one along each plane. The model-based can withstand up to 20N (in both planes) while the model-free resists a maximum of 24N (in both planes). The resulting pitch and roll angle swaying are shown in Fig. 5.8 and Fig. 5.9 respectively. The pitch angle variation in the model-free approach has a peak of 0.09 rad while the model-based approach has a peak pitch sway of 0.14 rad under the same disturbance magnitude of 20N.

As for the roll angle variation, the peak sway angle in the model-free approach

Figure 5.6: Roll angle variation under 24N push in the sagittal plane - simulation

Figure 5.7: Pitch angle variation under 24N push in the lateral plane - simulation
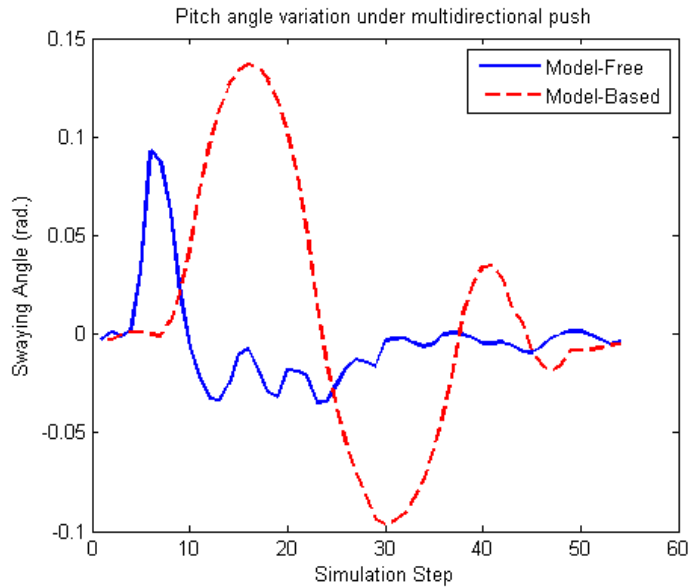
Figure 5.8: Pitch angle variation under 20N pushes in both planes - simulation

is 0.12 rad compared to 0.14 rad in the model-based approach, while the response time remains faster for the model-free case. This difference, despite being small, is still significant considering the limited range of the ankle strategy as discussed earlier.

Push not at CoM with Two Components (one in each plane)

The humanoid is subjected to the same push disturbance stated in the previous subsection but this time not at its CoM. The forces are applied at the head area. This presents a violation of the assumption that the push is applied at the CoM in the model-based case. This is reflected in the low resistance of the model-based approach which is able to handle only 15N push along both planes, compared to 19N in the model-free approach.

Figures 5.10 and 5.11 show the pitch and roll angle variations in response to a 15N push along both planes. The model-free approach improves the peak pitch angle sway by 0.04 rad and the peak roll angle sway by 0.01 rad compared to the model-based approach.

5.3.2 Experimental Results and Analysis

The model-free fall avoidance algorithm is tested on the actual Nao H25 V3.3 under the influence of push forces in the sagittal and lateral planes. The results are compared to those of the linear inverted pendulum model-based approach.

49
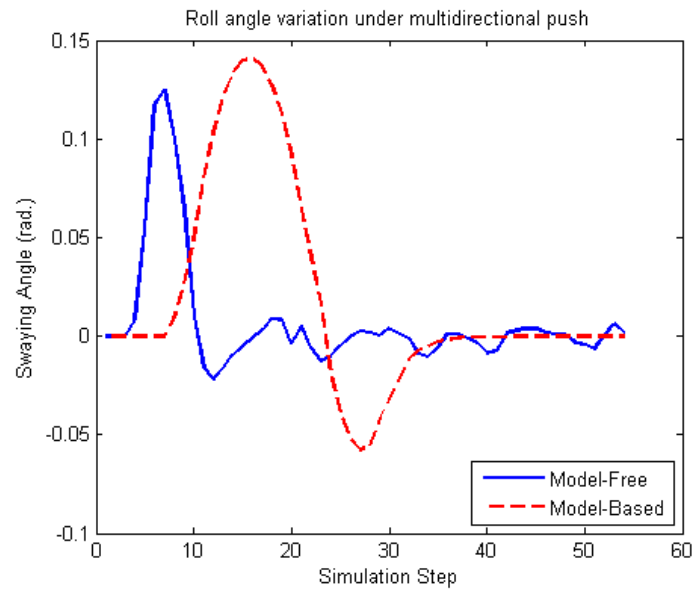
Figure 5.9: Roll angle variation under 20N pushes in both planes - simulation
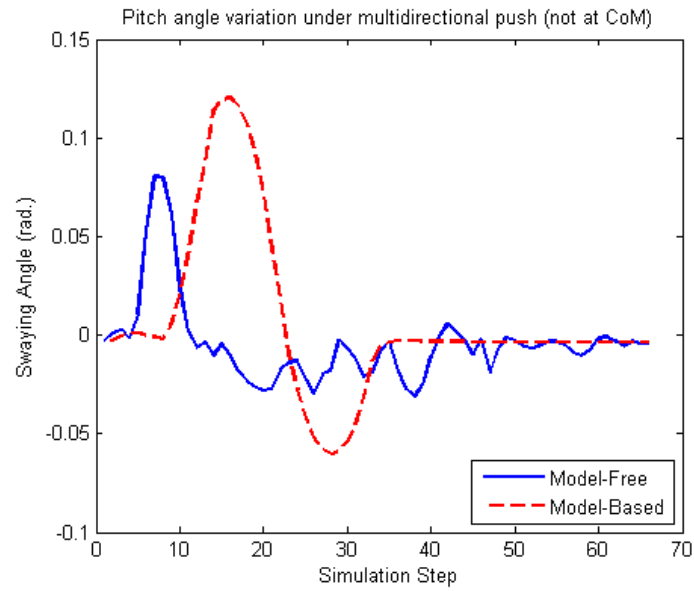
Figure 5.10: Pitch angle under 15N pushes in both planes (not at CoM) - simulation
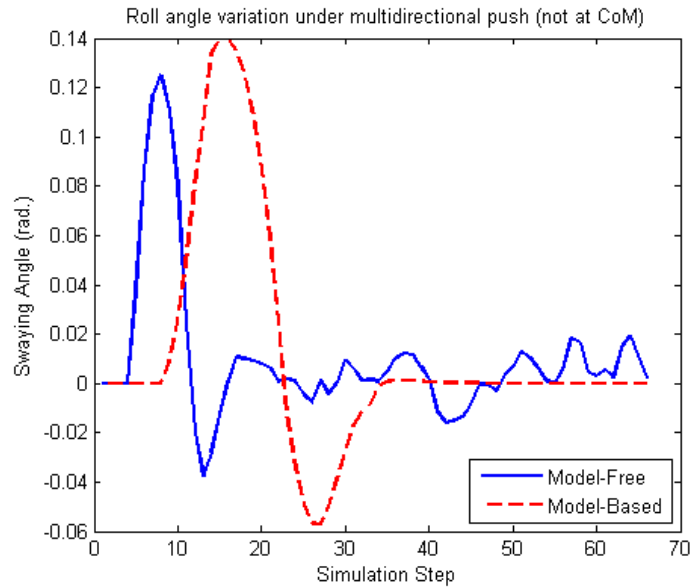
Figure 5.11: Roll angle under 15N pushes in both planes (not at CoM) - simulation

The model-based control parameters are tuned to obtain the best performance in terms of swaying angle and settling time.

The humanoid is set in quiet standing mode and the push force is applied using a suspended ball released at a predefined angle in order to ensure a consistent force. For each testing scenario, the experiment is repeated ten times and the results shown are the averages.

Push at CoM in the Sagittal Plane

The humanoid is subjected to a push force in the sagittal plane applied at its CoM. The model-free controller is able to recover form push forces up to 95N, while the model-based controller couldn't handle more than an 88N push force. Fig. 5.12 shows the response for an 88N sagittal push applied on the Nao while running model-free and model-based algorithms. In the model-free approach, the peak swaying angle is reduced by 0.26 rad and the settling time is reduced by 35 steps. The roll angle displacements are shown in Fig. 5.13 and are very minimal which is expected since the push is applied in the sagittal plane. The excessive swaying in the model-based approach is related to the reliance on stiffness control. The low stiffness allows for excessive swaying before the posture is corrected. However, when model-free control is used the position control driven by the change in proprioceptive sensor readings allows faster correction and thus involves less swaying.

51
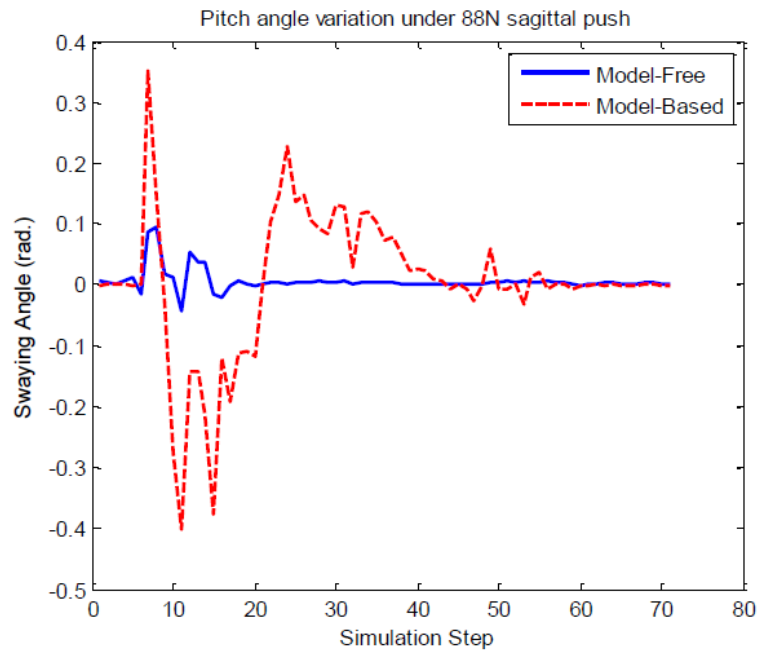
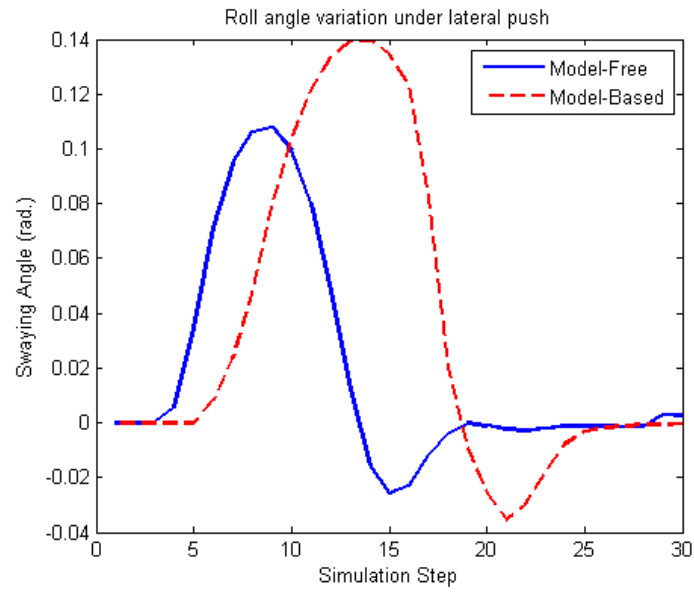Figure 5.12: Pitch angle variation under 88N push in the sagittal plane - experiment
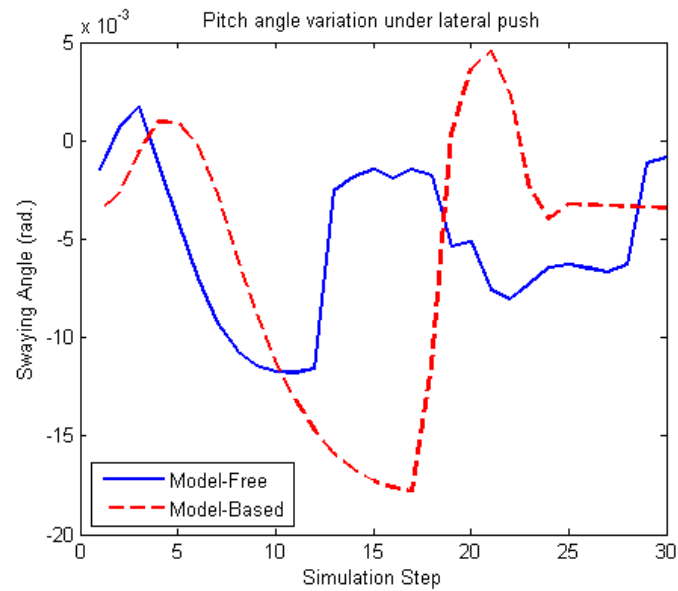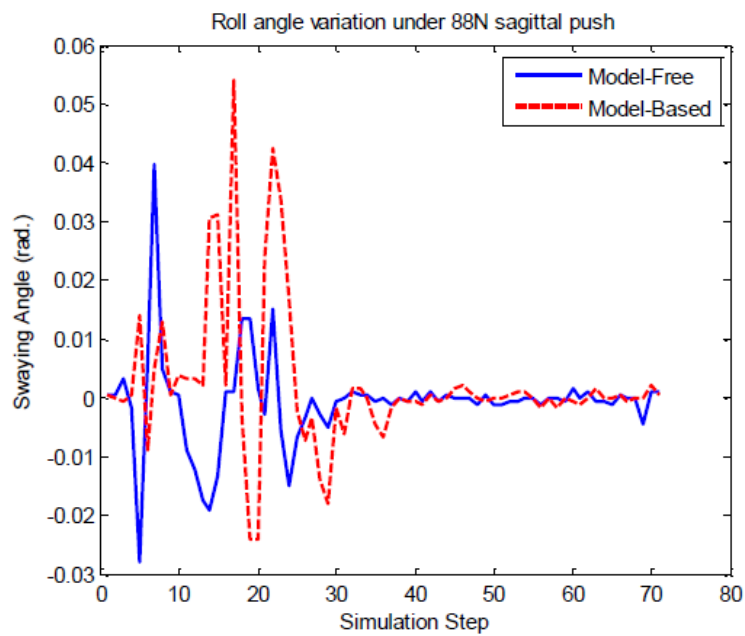

Figure 5.13: Roll angle variation under 88N push in the sagittal plane - experiment
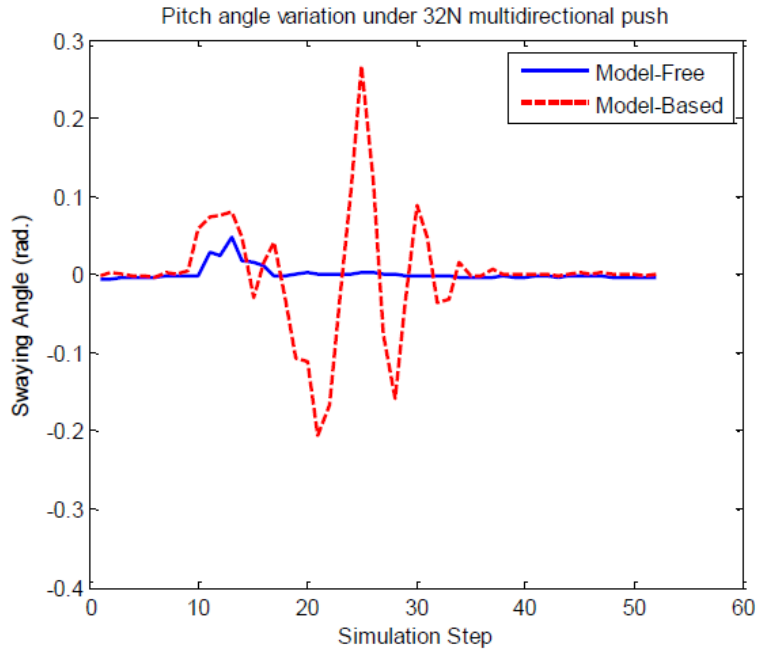
Figure 5.14: Pitch angle variation under 32N push in both planes - experiment

Push at CoM in Both Planes

In order to compare the two approaches under a multidirectional push, Nao is rotated by 45 degrees from the previous position. This way the released ball will apply a force with components in the sagittal and lateral planes. In this setup, the ability of the model-based approach is very limited and the maximum force beyond which it is impossible to recover is around 32N. However, the model-free approach maintained its ability to recover from the 95N push force. The comparison between the two approaches is done at a 32N push after averaging the results of ten trials. The model-free approach improves the peak pitch angle displacement by 0.22 rad and the settling time by 18 steps (Fig. 5.14). As for the roll angle displacement, the model-free approach improves the maximum angle displacement by 0.13 rad and the settling time by 18 steps (Fig. 5.15).

The experimental results on Nao show more substantial advantages of the model-free approach in swaying angle and settling time. The steady state perturbations present in the simulations are negligible in the experimental testing. This is due to the fact that in the simulation, Nao's feet are not well settled on the ground surface which maintains a difference between the front/back and right/left FSRs.

The proposed model-free posture control could be enhanced further by making it adaptable to different terrain types. This can be done by adding a calibration stage to identify the terrain before starting the operation. The proposed enhance-
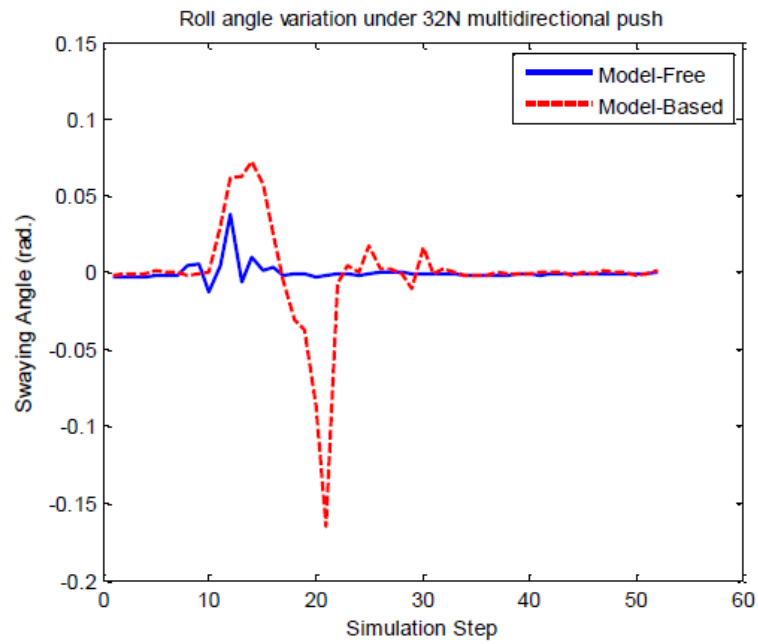
Figure 5.15: Roll angle variation under 32N push in both planes - experiment

ment would allow for push recovery on uneven terrains.

There is no clear choice between model-free and model-based control for humanoid push recovery. The preference is driven by the constraints placed on the system and the environment in which the humanoid is operating. The more flexible the constraints are, the choice of model-free control becomes more dominant.

Chapter 6

Energy-Minimization in Humanoid Gait

The concept of energy minimization is widely used for humanoid posture and movement control. The focus here is on the application of this concept in humanoid gait. In this section, the different approaches are categorized to models, types of energy, and types of controllers used to minimize energy in humanoid gait.

6.1   Biped Models an Types of Energy

The type and complexity of the models used differ from one work to another based on the parameters monitored and type of control. The compass model (two-link model) is widely used in the literature. It consists of two sticks and a Center of Mass (CoM). The feet, knees and trunk are not represented in this model. Asano *et al.* [75] use the compass model in designing walking gait cycles based on Mechanical Energy (ME) restoration. The claim is that the Potential Energy (PE) of the CoM is constant at the instant of heel strike, while there occurs a loss in the Kinetic Energy (KE). Therefore, restoring this lost energy creates a stable dynamic gait.

Another use of the compass gait model is found in the work of Holm and Spong [80], where they focus on the speed control of gait using the ankle torques only. Speed control is achieved by KE shaping by solving partial differential equations representing the biped's equations of motion. A typical representation of the biped's equation of motion is shown in (6.1), where $\mathbf{M}$ is the mass matrix equation, $\mathbf{C}$ is the centrifugal and Coriolis terms matrix, $\mathbf{G}$ is the vector of potential dependent terms, $\mathbf{B}$ is the matrix of actuators, and $\mathbf{u}$ is the vector of input forces.

$$\mathbf{M}(\mathbf{q})\ddot{\mathbf{q}} + \mathbf{C}(\mathbf{q}, \dot{\mathbf{q}})\dot{\mathbf{q}} + \mathbf{G}(\mathbf{q}) = \mathbf{B}(\mathbf{q})\mathbf{u} \qquad (6.1)$$

The compass model is also used in optimal energy gait planning. The KE is considered to be constant along the geodesics of the CoM path [82]. It can be seen that when the compass model is used for gait design, the focus is always on the KE. This is logical since in this specific model, the CoM is always at a constant height which indicates a constant PE throughout the whole gait cycle. However; this is not the case in human gait.

The four-link model, also known as the kneed compass model allows the variation of the CoM height during gait. This gives an important role for the PE factor as it is now considered to be varying throughout the gait cycle. In [97], a kneed compass gait is designed based on minimizing the total ME rate. The author's experiments however show the fragility of this design especially against external disturbances. Compliant design is also integrated into the compass model for ankle joint activation to minimize KE [78].

Another 4-link model approach is used in [98], where the gait is designed through multi virtual gravity forces to minimize actuator torque energy. The humanoid is moved as if it is pulled through by virtual forces in order to perform the gait cycle [98].

The hip role in humanoid gait is highlighted in the use of the three-link model which consists of two legs and a torso. In [76], only the hip joint is actuated. This is claimed to increase energy-efficiency due to under-actuation. However, this claim is not verified in experiments or by comparing with other approaches. Compliance is also integrated into the three-link model in order to study the effect of stiffness optimization on energy consumption [99].

The knee is considered by some as the main source of energy consumption [77]. This is due to the fact that in humanoids the main source of PE change is the knee flexion and extension which varies the height of the CoM. This is not the case in humans since they have the ability to bend their foot soles during gait. Sun and Roos [77] use the five-link model but focus on minimizing the energy consumption at the knee level by monitoring the current passing through it. Other researchers claim that although the peak power and torque are at the knee level, the most work is done at the level of the hip joint [100].

A more complex model is the seven-link model which is the same as the five-link model but with feet. In [79], the minimization of energy is targeted by minimizing ankle jerk and trajectory planning. This is done by monitoring KE. In applications where the focus is limited to monitoring energy liberation during gait, the 3D model is often used to take every joint into account [101, 102]. However, few other approaches consider 3D models for gait modification accompanied with ZMP adjustment [103].

6.2 State of the Art Controllers

The control methods used in gait design through energy minimization can be divided into two main approaches; deterministic and learning-based.

6.2.1 Deterministic Control Methods

The deterministic control approaches usually rely on the humanoid's equations of motion at each of the three phases; first single support, double support, and second single support.

In [83], the energy cost function based on impulse factor of heel strike is used for energy minimization based gait. The cost function shown in (6.2) is for one gait cycle between 0 and T. It is divided into the single support and double support phases, where u_{ss} is the input torque vector during single support phase and u_{ds} is for the double support phase, I_{cont} is the impulse of the impact force which is active during the contact phase, and I_{top} is during the non-contact phase.

$$J = \int_0^{T_1} u_{ss}^T u_{ss} dt + I_{cont}^T I_{cont} + \int_{T_1}^T u_{ds}^T u_{ds} dt + I_{top}^T I_{top} \tag{6.2}$$

Another deterministic control approach is zeroing the total mechanical energy in addition to applying ZMP control [97]. The energy function that is being minimized in this work is shown in (6.3), where θ is the joint velocity vector, M is the mass matrix, and P is the PE matrix.

$$E = \frac{1}{2} \dot{\theta}^T M(\theta) \dot{\theta} + P(\theta) \tag{6.3}$$

The most common approach of the deterministic control methods is the torque control which takes various forms and might be performed at various levels. As stated previously, different models lead to different actuated joints. Torque control is thus performed on the actuated joints in order to ensure stable gait [80, 98, 76, 100]. Therefore, torque control is applied on either some or all of the following joints:

- Ankle joints (with foot strike correction to avoid premature heel/toe strike)

- Knee joints (to minimize PE)

- Hip joints (to control the torso momentum)

Another type of torque control is the stiffness control which is applied in robots that don't support input torques on their joints.

6.2.2 Learning-based Control Methods

The main objective in the learning-based methods is to find the most energy-efficient gait parameters that ensure a stable gait. Such parameters include:

- Step length

- Step height

- Step duration

- Bending angle

- Bending time

- Torso pitch inclination

In [77], gradient parameter learning is used to find the above mentioned parameters that best suit the Nao humanoid. The experiments show that the optimized gait has less energy consumption than the standard Nao gait. Another learning-based approach is in the application of the multi virtual gravity forces discussed in the previous section [98]. While machine learning is a possible approach for humanoid gait design, it cannot be considered biomimetic. Since it doesn't adopt human characteristics, a high number of trials is needed to teach the robot a proper gait.

Chapter 7

Stable Humanoid Gait Design based on Energy-Exchange

This chapter covers the new energy-exchange gait design for humanoid robots. An Energy-Based Controller is also proposed to drive the joint motors to the desired gait angles.

7.1 Gait Design Outline

The first step in the proposed gait synthesis technique is to mathematically express the out-of-phase oscillation between the kinetic and potential energies at the humanoid's CoM. This is presented in (7.1) and (7.2), where $f(t)$ and $g(t)$ represent kinetic and potential energies, respectively. When (7.1) is true at a certain time t, then (7.2) should be applied as well.

$$\frac{df(t)}{dt} = \frac{dg(t)}{dt} = 0 \tag{7.1}$$

$$\frac{d^2 f(t)}{dt^2} \cdot \frac{d^2 g(t)}{dt^2} < 0 \tag{7.2}$$

Using the above constraints to design gaits renders the gait generation problem more flexible and applicable to different models. A flowchart of the gait synthesis steps is shown in Fig. 7.1.

The gait design starts with the choice of a biped model in the sagittal plane. Next, the inter-link angle of each actuated joint is represented by a sum of sines expression. This model for joint angles is inspired and derived from human motion capture data and additionally, it defines a parameter search space for the optimization problem.

Then, the kinetic and potential energies at the biped's CoM are computed in terms of joint angles. Once the energy expressions are obtained, an optimization problem is formed to solve for the parameters of joint angles. The optimization
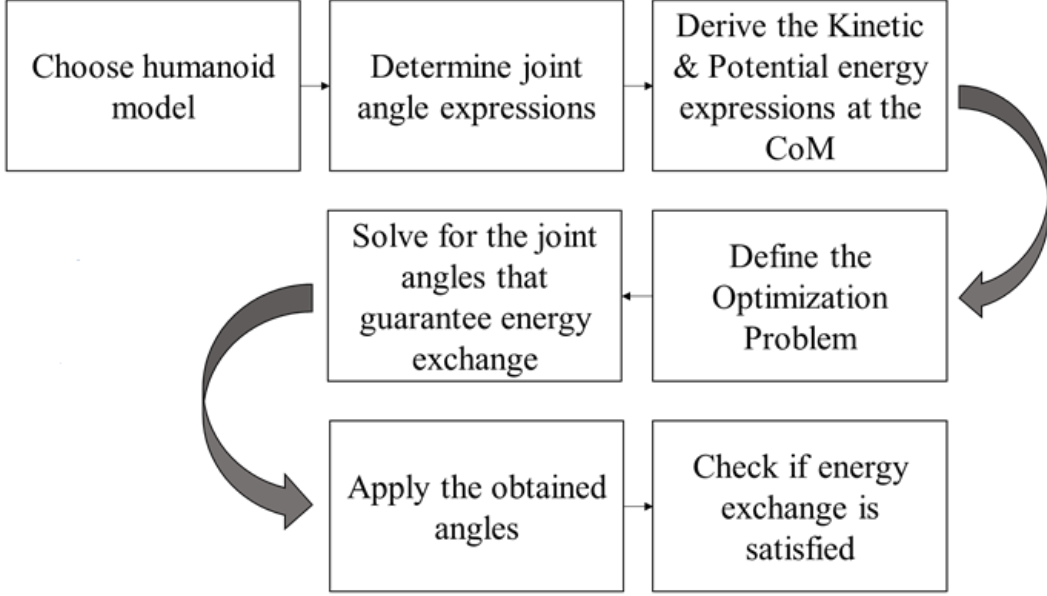
Figure 7.1: Gait generation algorithm based on the human-inspired energy exchange theory

objective function aims at maintaining the energy-exchange property. Once the resulting joint angles are solved for, the gaits are written to a motion file which is then fed to the robot's model for simulation. This proposed roadmap is applicable to any humanoid model.

The five-link model representing the torso, thighs, and knees is used and is depicted in Fig 7.2. Finally, the kinetic and potential energy expressions at the CoM are recomputed to validate the exchange of energies.

7.2 Humanoid Model and Energy Expressions

The five-link model is used to represent a simplified Hoap2 model with five DoFs shown in Fig. 7.2, where (x_0, y_0) is the CoM position. Hence, for the five links in the model, with positions (x_i, y_i) and masses, m_i, where $(x, y) = (\frac{\sum m_i x_i}{\sum m_i}, \frac{\sum m_i y_i}{\sum m_i})$ The model parameters are listed in Table 7.1.

The generalized coordinates are given in (7.3), whereas the expressions of the kinetic and potential energies of the CoM are shown in (7.5) and (7.6), respectively. Here $M(q)$ is the mass matrix and g is the gravitational acceleration.

$$q = (x_0, y_0, \alpha, \beta_l, \beta_r, \gamma_l, \gamma_r)^T \tag{7.3}$$

$$H(q) = \begin{bmatrix} y_0 - \frac{L_1}{2}\cos\alpha - \frac{L_2}{2}\cos(\alpha - \beta_l) & y_0 - \frac{L_1}{2}\cos\alpha - \frac{L_2}{2}\cos(\alpha - \beta_r) \\ y_0 - L_1(\cos\alpha + \cos(\alpha - \beta_l)) - \frac{L_2}{2}\cos(\alpha - \beta_l + \gamma_l) & y_0 - L_1(\cos\alpha\cos(\alpha - \beta_r)) - \frac{L_2}{2}\cos(\alpha - \beta_r + \gamma_r) \end{bmatrix} \tag{7.4}$$

60
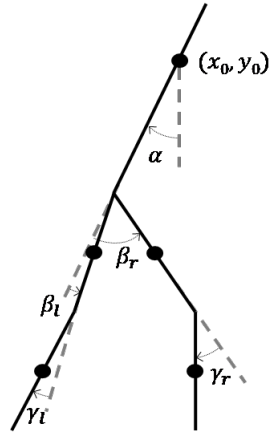
Figure 7.2: 5-link humanoid model chosen to simulate the new gait synthesis

Table 7.1: List of symbols and their corresponding parameters.

Model Parameters	
Symbol	**Parameter**
m_1	Torso mass
m_2	Thigh mass
m_3	Shank mass
L_1	Toso length
L_2	Thigh, shank length
α	Torso angle
$\beta_{l/r}$	Knee angle (left/right)
$\gamma_{l/r}$	Ankle angle (left/right)

$$KE = \frac{1}{2}\dot{q}^T M(q)\dot{q} \tag{7.5}$$

$$PE = m_1 g(y_0 - \frac{L_1}{2}\cos\alpha) + (m_2 m_3)gH(q) \tag{7.6}$$

7.3 Gait Motion Generation - An Optimization Problem

The joint angles are obtained by solving an optimization problem with energy exchange as its objective function. Before solving for the gait angles, they are represented as sum of sinusoids as shown in the following study done on human gait. Data analysis of human gait is done using Motive motion capture system done on three subjects during forward walking at subjects' preferred speed.The markers are placed on the ankles, knees, hips, and CoM to capture the position and orientation of the links of the five-link model adopted in this thesis. The respective joint angles are fitted with sum-of-sines functions with different degrees.

7.3.1 Joint Angle Expressions

Human gait is studied using the Motive motion capture software. The joint angles which correspond to the ones on the five-link model are analyzed in order to find a general form of each angle. Joint angles during constant speed gaits are known to be of sinusoidal nature.

In this section, the number of dominant frequencies for each angle is determined in order to find a general sum-of-sines representation. Fig. 7.3 shows the power spectrum of the torso oscillations. There is clearly one dominant frequency and therefore α in the five-link model can be represented as a simple sinusoidal function, as in (7.7):

$$\alpha = a_{\alpha 0} + a_{\alpha 1}\sin(b_\alpha t + \phi_\alpha) \tag{7.7}$$

The power spectrum of the left thigh oscillations is plotted in Fig. 7.4, showing two dominant frequencies. As a result, $\beta_{l/r}$ are expressed using a sum of two sines:

$$\beta_l = a_{\beta_{l1}}\sin(b_{\beta_l}t + \phi_{\beta_{l1}}) + a_{\beta_{l2}}\sin(b_{\beta_l}t + \phi_{\beta_{l2}}) \tag{7.8}$$

The knee oscillations $(\gamma_{l/r})$ are more complex as can be seen in the power spectrum of Fig. 7.5 and the expression:

$$\begin{aligned} \gamma_l =& a_{\gamma_{l0}} + a_{\gamma_{l1}}\sin(b_{\gamma_l}t + \phi_{\gamma_{l1}}) + a_{\gamma_{l2}}\sin(b_{\gamma_l}t + \phi_{\gamma_{l2}}) \\ &+ a_{\gamma_{l3}}\sin(b_{\gamma_l}t + \phi_{\gamma_{l3}}) \end{aligned} \tag{7.9}$$
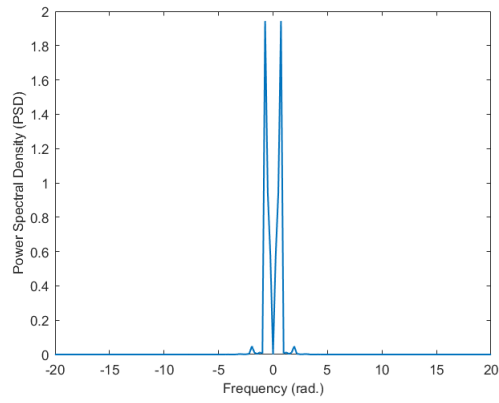
Figure 7.3: Power Spectral Density of torso oscillations (α)
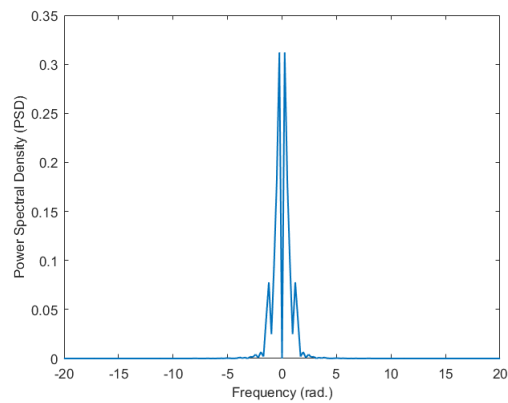
Figure 7.4: Power Spectral Density of thigh oscillations (β_l)
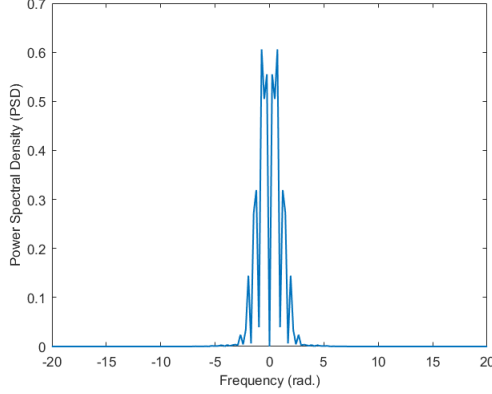
Figure 7.5: Power Spectral Density of thigh oscillations (γ_l)

The left and right joint angles have the same representation but with a phase shift of π rad, to ensure symmetry during gaits.

The obtained joint angle representations are used to provide a parameter search space for the optimization problem. The frequencies of the angle representations, $b_\alpha, b_{\beta_{l/r}}, b_{\gamma l/r}$, are used to set the speed of the gait so they could be predetermined before the optimization process. Therefore, one has to solve for the a and ϕ parameters. There are 3 parameters for α, 5 parameters for each β, and 7 parameters for each γ , making a total of 27 parameters.

7.3.2 Optimization problem

With the joint angles formulations derived above, the optimization problem is formalized as follows:

Objective function:

$$minQ = \left(\frac{dKE}{dt}\right)^2 + \left(\frac{dPE}{dt}\right)^2$$

Subject to:

- $\left(\frac{d^2KE}{dt^2}\right) \cdot \left(\frac{d^2PE}{dt^2}\right) < 0$

- joint angle limit constraints (set based on the physical limitations of the humanoid joints)

$$-0.0524 < \alpha < 1.5708 rad.$$
$$-1.4312 < \beta_{l/r} < 1.2392 rad.$$
$$-0.0175 < \gamma_{l/r} < 2.2689 rad.$$

- footstep duration constraint within which the peak exchange must occur

Solving for: 27 parameters (only a's and ϕ's) that constitute the joint angles (except the frequencies which are set to determine the gait speed).

The optimization problem is solved in Wolfram Mathematica using the Differential Evolution method with an Accuracy Goal of 20 and Precision Goal of 18. The objective function takes the sum of squares of the first derivative of KE and PE in order to force a non-negative solution. This could be also ensured through adding constraints on each of the KE and PE. Future work may include studying the effect of changing n while using $minQ = \left(\frac{dKE}{dt}\right)^n + \left(\frac{dPE}{dt}\right)^n$ as an objective function.

7.3.3 Simulation Results and Analysis

In this section, the energy-exchange gait generation algorithm is simulated on Hoap2 using the standard PID controller found in Webots. The generated walk is compared to the off-the-shelf one found in Webots in terms of energy analysis and joint-torque exertion.

Energy Analysis

The generated gaits were simulated on Hoap2 (parameters in Table 7.1) in Webots. Fig. 7.6 shows the simulation model and main specifications.

The proposed energy-exchange gait is simulated using the standard PID controller in Webots and compared to the off-the-shelf gait of Hoap2 provided by the simulator with the same controller. For all simulations Hoap2 walks at a speed of 0.025 m/s during both standard and energy-exchange gait. The new energy-exchange gait is evaluated by the generated energy patterns and compared to the original gait used for Hoap2.

Torque patterns of the actuated joints are also compared to show improvement in the new generated gait. Snapshots of the new gait and the standard walk are shown in Fig. 7.7 and Fig. 7.8 respectively. The kinetic and potential energies at the humanoid's CoM during the new gait are shown in Fig. 7.9 to validate the energy-exchange property. The peak exchange of the energy patterns resembles the behavior during human gait in Fig. 2.4 The proposed energy-exchange exerts less torque at the torso compared to that needed in the standard gait (Fig. 7.10). Similar improvements are evident on the thighs and shanks as shown in Fig. 7.11 and Fig. 7.12, provided that both gaits have the same speed and the standard controller in Webots is used to drive both gaits.

Averages of the absolute values of torques exerted at each link in both standard and proposed gait are summarized in Table 7.2. The average torque can be used as an indicator since both gaits are applied at the same constant speed.
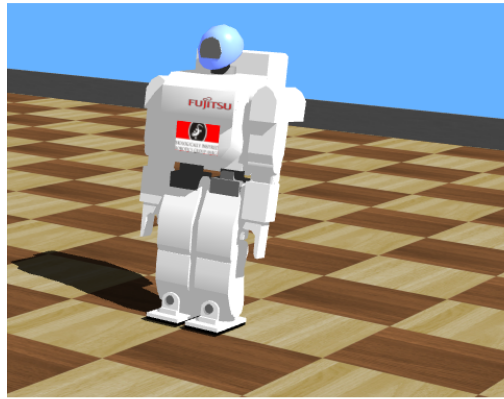
Hoap2 Specifications
Height: 48 cm
Weight: 7.03 kg
DoFs: 25

Figure 7.6: Hoap2 simulation model and specifications
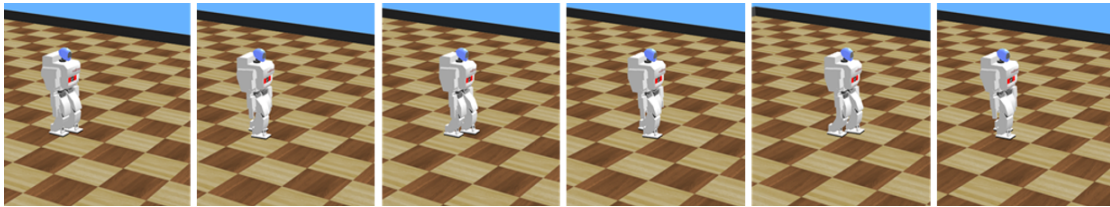
Figure 7.7: Snapshots of gait simulations with energy-exchange
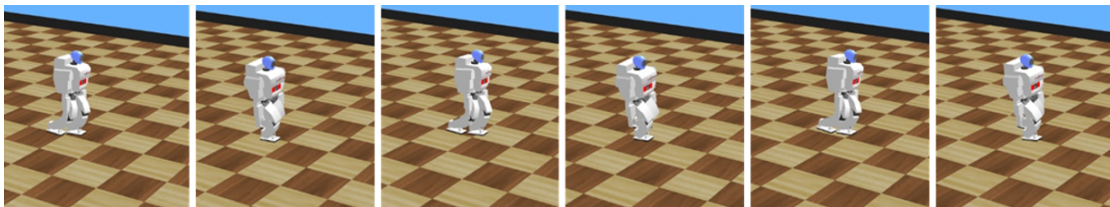
Figure 7.8: Snapshots of gait simulations with standard gait
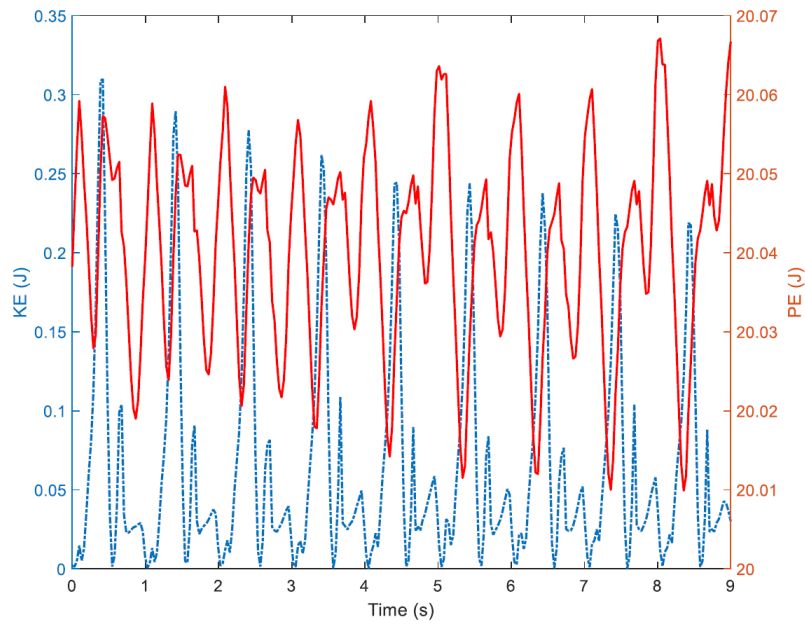
Figure 7.9: KE and PE patterns of Hoap2 CoM during new energy-exchange gait

Figure 7.10: Torque exerted at the torso during standard gait (blue) and energy-exchange gait (red dashed)

Figure 7.11: Torque exerted at the left thigh during standard gait (blue) and energy-exchange gait (red dashed)

Figure 7.12: Torque exerted at the left shank during standard gait (blue) and energy-exchange gait (red dashed)

Table 7.2: Average torque exerted at each link during standard and energy-exchange gaits.

Gait Type	Average Torque (absolute values) N rad		
	Torso	Thigh	Shank
Standard gait	0.56	7.76	4.89
Energy-exchange gait	0.48	0.47	1.15
% Improvement	14.3%	93.9%	76.5%
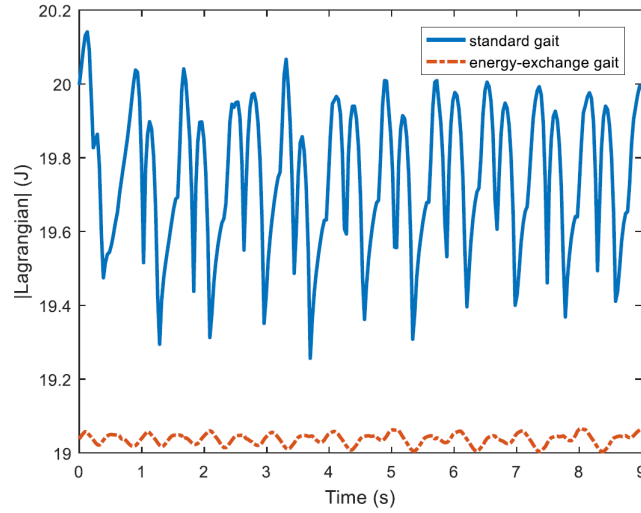
Figure 7.13: Overall Absolute Lagrangian during standard gait (blue) and energy-exchange gait (red dashed)

The new gait shows 14.3% improvement in torque exerted at the torso, 93.9% less torque at the thighs, and 76.5% improvement at the shanks.

In order to compare the overall energy-efficiency, the total mechanical energy during the two gaits is evaluated. The new proposed gait has an average mechanical energy of 19 J as compared to 19.98 J in the standard gait showing an improvement of 4.9%. The overall Lagrangian of the new proposed gait is plotted and compared to the standard gait Lagrangian as shown in Fig. 7.13. The improvement in energy-efficiency of the proposed gait is evident in the small variations of the Lagrangian (maximum difference between peaks is 0.06) as compared to the larger variations in the standard gait (maximum difference is 0.88). This highlights the energy-exchange in the proposed gait where the kinetic energy is being transformed to potential energy and backwards.

Gait Stability Against Push Disturbances

The proposed energy-exchange gait is tested against push disturbances in the sagittal and lateral planes as shown in Fig. 7.14. The push disturbances are
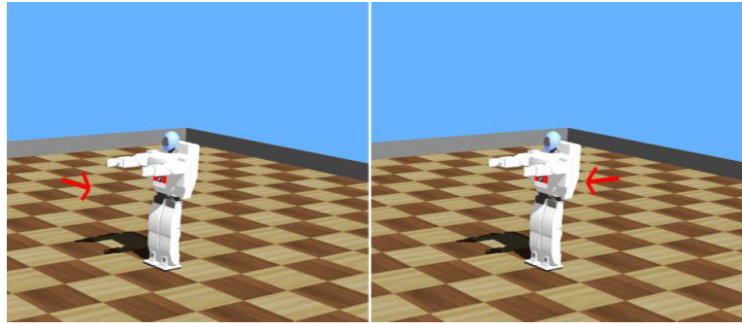
Figure 7.14: Push disturbances (sagittal and lateral) in Webots represented by red arrows

applied during single stance, which is the most vulnerable phase during gait.

The new energy-exchange gait withstands a push force up to a magnitude of 15 N.m in the sagittal plane and 10 N.m, in the lateral plane. This result presents a 36.4% improvement in the sagittal plane and 25% in the lateral plane compared to the standard Hoap2 gait.

Given the improvements introduced by the new gait generation technique, there remained an area for improvement in the control method used to achieve this gait. Since our biomimetic approach is centred on energy-exchange, a general purpose Energy-Based Controller was developed and used for humanoid gait control.

7.3.4 Experimental Results and Analysis

The energy-exchange gait generation algorithm is tested on the Nao humanoid. The generated walk is compared to the off-the-shelf one found in Webots in terms of energy analysis and joint-torque exertion.

Energy Analysis

The proposed energy-exchange gait is tested using the standard PID controller available with Nao and compared to the off-the-shelf gait angles found in th built-in Nao walk (with the same controller). For all experiments Nao walks at a speed of 0.03 m/s during both standard and energy-exchange gait. The new energy-exchange gait is evaluated by the generated energy patterns and compared to the original gait used for Nao.

Torque patterns of the actuated joints are also compared to show improvement in the new generated gait. The kinetic and potential energies at the humanoid's CoM during the new gait are shown in Fig. 7.15 to validate the energy-exchange property. The peak exchange of the energy patterns resembles the behavior during human gait in Fig. 2.4. The proposed energy-exchange exerts less torque at the torso compared to that needed in the standard gait (Fig. 7.16). The thighs
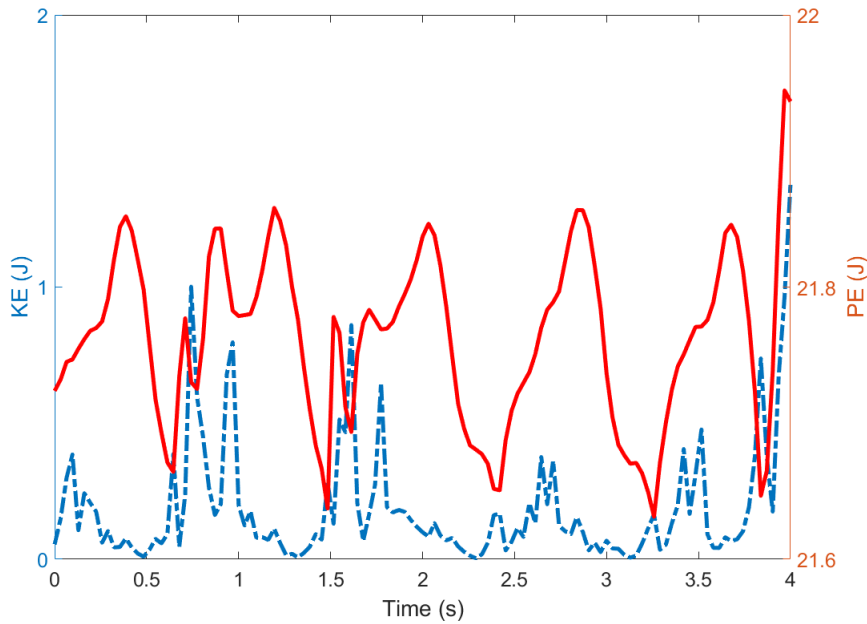
Figure 7.15: KE and PE patterns of Nao CoM during new energy- exchange gait

Table 7.3: Average torque exerted at each link during standard and energy-exchange gaits on Nao.

Gait Type	Average Torque (absolute values) N rad		
	Torso	Thigh	Shank
Standard gait	3.39	4.20	2.76
Energy-exchange gait	1.36	3.81	2.63
% Improvement	59.9%	9.3%	4.7%

and shanks experience similar improvements as shown in Fig. 7.17 and Fig. 7.18, given that both gaits have the same speed and same controller.

Averages of the absolute values of torques exerted at each link in both standard and proposed gait are summarized in Table 7.3. The average torque can be used as an indicator since both gaits are applied at the same constant speed. The new gait shows 59.9% improvement in torque exerted at the torso, 9.3% less torque at the thighs, and 4.7% improvement at the shanks.

In order to compare the overall energy-efficiency, the total mechanical energy during the two Nao gaits is evaluated. The new proposed gait has an average mechanical energy of 21.6 J as compared to 22.0 J in the standard gait showing an improvement of 1.8%. The overall Lagrangian of the new proposed gait is plotted and compared to the standard gait Lagrangian as shown in Fig. 7.19. The improvement in energy-efficiency of the proposed gait is evident in the small variations of the Lagrangian (maximum difference between peaks is 0.6) as com-
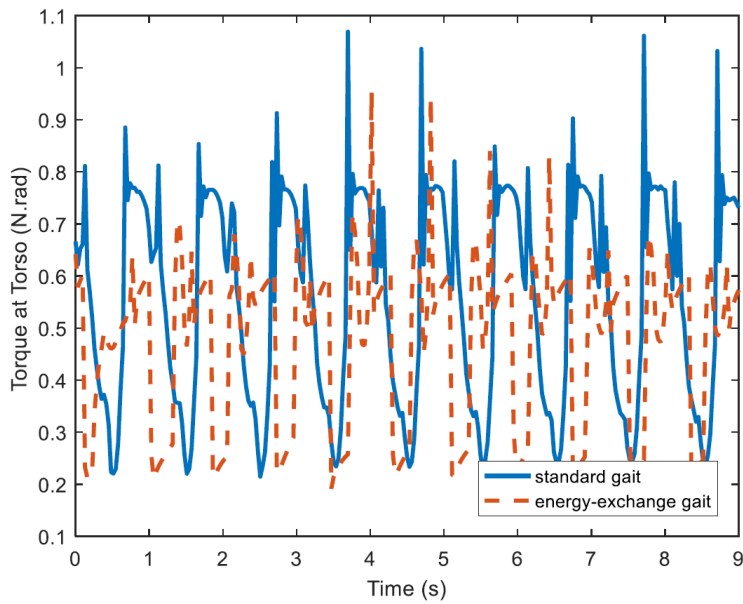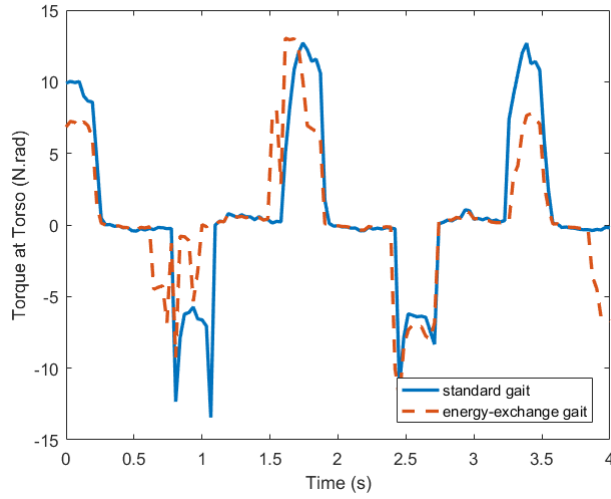
Figure 7.16: Torque exerted at the torso during standard gait (blue) and energy-exchange gait (red dashed)
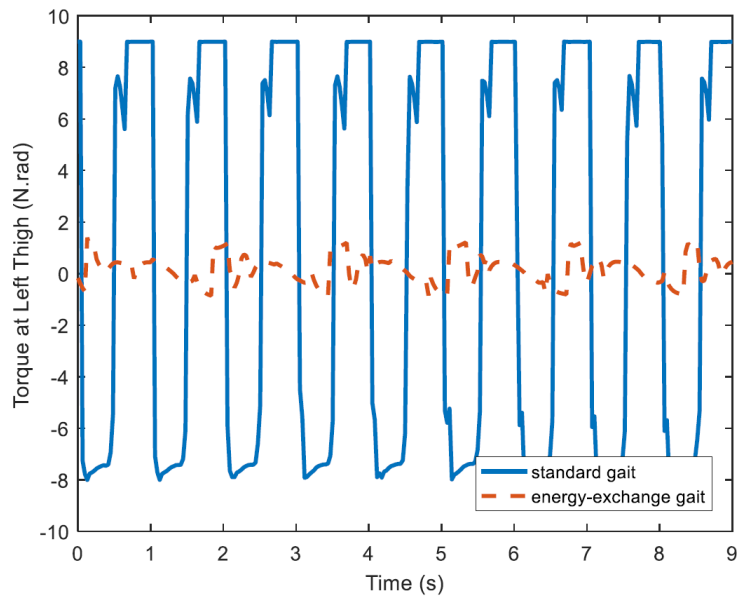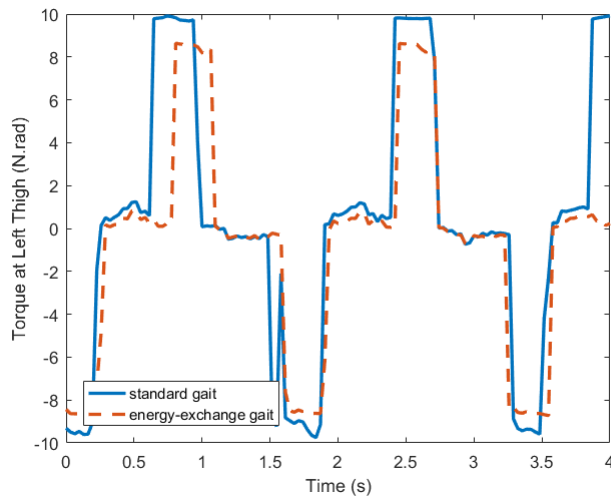

Figure 7.17: Torque exerted at the left thigh during standard gait (blue) and energy-exchange gait (red dashed)
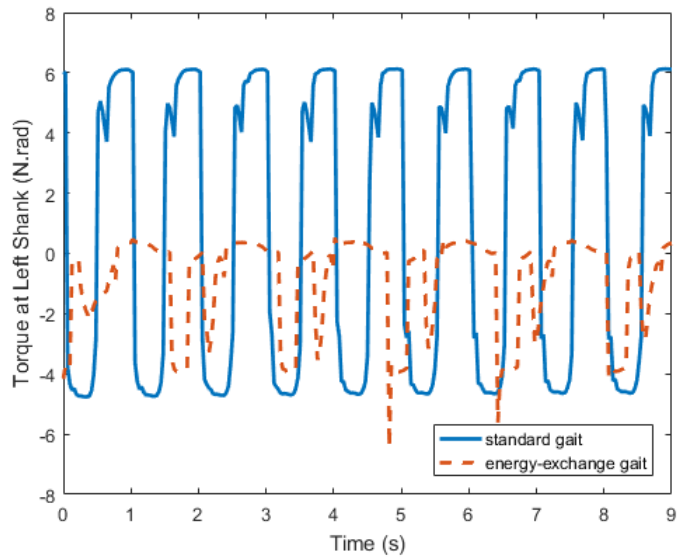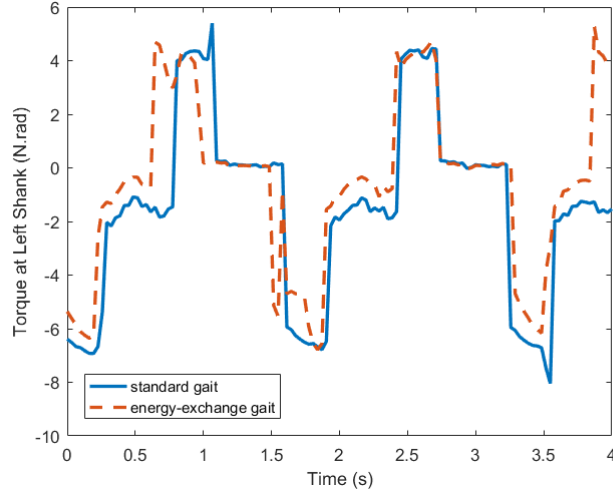
Figure 7.18: Torque exerted at the left shank during standard gait (blue) and energy-exchange gait (red dashed)

pared to the larger variations in the standard gait (maximum difference is 1.3). This highlights the energy-exchange in the proposed gait where the kinetic energy is being transformed to potential energy and backwards.

7.4 Energy-Based Control

In this section, the concept of Energy-Based Control (EBC) is introduced, and applied to the problem of an inverted pendulum with both, a fixed, and moving pivot.

7.4.1 Controller Design

The first step in the proposed energy-based controller is defining the system's vector of generalized coordinates q, and its derivative with respect to time $\dot{q}$. The vector q consists of the actuated and non-actuated coordinates q_{act} and q_{nonact}, respectively. The kinetic and potential $(P(q))$ energy expressions are derived in terms the aforementioned vectors and used to derive the Euler-Lagrangian equations of motion:

$$L = 1/2\dot{q}^T M \dot{q} - P(q)$$

$$\frac{d}{dt}\left(\frac{\partial L}{\partial \dot{q}_{act}}\right) - \frac{\partial L}{\partial q_{act}} = u,$$

$$\frac{d}{dt}\left(\frac{\partial L}{\partial \dot{q}_{nonact}}\right) - \frac{\partial L}{\partial q_{nonact}} = 0. \tag{7.10}$$
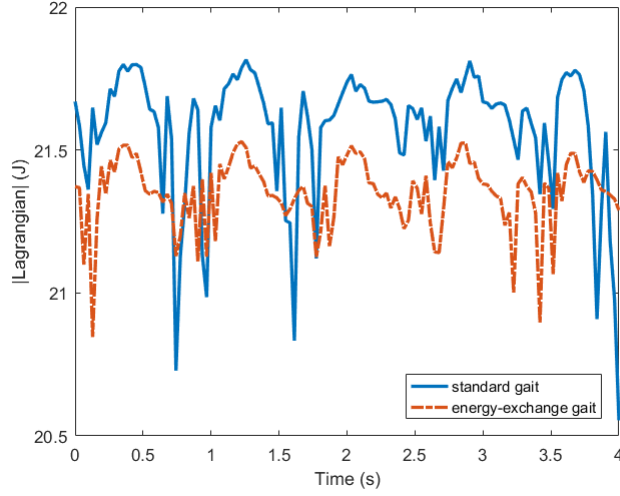
Figure 7.19: Overall Absolute Lagrangian during standard gait (blue) and energy-exchange gait (red dashed)

The equations of motion are derived from (7.10), where u is the control input, and used to find an expression for $\ddot{q}_{act}$.

A candidate Lyapunov function (V) is chosen to be a function of the system's total mechanical energy (E) the actuated portion of the generalized coordinates (q_{act}) and their derivative ($\dot{q}_{act}$) such that

$$V = \frac{1}{2}k_1 E^2 + \frac{1}{2}k_2 q_{act}^2 + \frac{1}{2}k_3 \dot{q}_{act}^2, \tag{7.11}$$

where k_1, k_2, and k_3 are tunable weights. In order for V to be a valid Lyapunov function and to ensure the system's stability, $\dot{V}$ must be negative semi-definite.

$$\dot{V} = k_1 E \dot{E} + k_2 q_{act} \dot{q}_{act} + k_3 \dot{q}_{act} \ddot{q}_{act}. \tag{7.12}$$

The work W, which is equivalent to the change in energy E can be expressed as [34]:

$$\Delta E = W = \int u \; dq_{act}, \tag{7.13}$$
$$\dot{E} = u\dot{q}_{act}.$$

Equation (7.13) allows us to rewrite $\dot{V}$ in a factorized form:

$$\dot{V} = \dot{q}_{act}(k_1 E u + k_2 q_{act} + k_3 \ddot{q}_{act}) \tag{7.14}$$

This makes it easier to find the appropriate control input, which maintains $\dot{V}$ as negative semi-definite. Enforcing the stability criterion as it pertains to the

74

Lyapunov analysis, $\dot{V} = -k_4 \ddot{q}_{act}^2$ is set in (7.14), and used to solve for the control input function u, to arrive at (7.15), where $k_1 E \neq 0$:

$$u = -\frac{1}{k_1 E}(k_4 + k_2 q_{act} + k_3 \ddot{q}_{act}). \tag{7.15}$$

Using the expression of $\ddot{q}_{act}$ obtained from the Euler-Lagrangian equations of motion, when plugged into (7.15) the final expression of the control input u is obtained, as will be done in the sections below.

Fixed Inverted Pendulum

Applying the above strategy to a fixed inverted pendulum, the Euler-Lagrangian equations of motion are derived from the system's kinetic and potential energies

$$KE = \frac{1}{2} m l^2 \dot{\theta}^2, \tag{7.16}$$

$$PE = -mgl \cos \theta, \tag{7.17}$$

$$L = \frac{1}{2} m l^2 \dot{\theta}^2 + mgl \cos \theta, \tag{7.18}$$

$$mgl \sin \theta + ml^2 \ddot{\theta} = u_{fixed}, \tag{7.19}$$

where m is the pendulum's mass, l is its length, θ is the angle, g is the gravitational acceleration, and u_{fixed} is the control input which is the torque at the pivot in this particular system.

From (7.19) the expression of the actuated coordinate acceleration is obtained, which will be used in deriving the control law:

$$\ddot{\theta} = \frac{u_{fixed} - mgl \sin \theta}{ml^2}. \tag{7.20}$$

The candidate Lyapunov function is chosen as described in (7.11) to include the total mechanical energy in addition to the actuated coordinates and their velocities.

$$V = \frac{1}{2} k_1 E^2 + \frac{1}{2} k_2 \theta^2 + \frac{1}{2} k_3 \dot{\theta}^2. \tag{7.21}$$

Ensuring stability by keeping $\dot{V} \leq 0$, the following control law is obtained:

$$u_{fixed} = -\frac{2lm(-gk_3 \sin \theta + k_2 l\theta + k_4 l\dot{\theta})}{2k_3 - 2gk_1 l^3 m^2 \cos \theta + k_1 l^4 m^2 \dot{\theta}^2}. \tag{7.22}$$
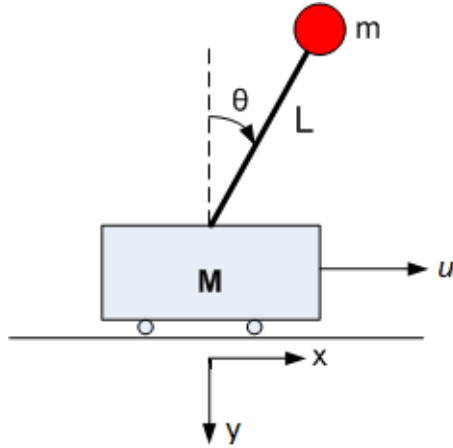
Figure 7.20: Inverted pendulum on a cart

In order to make our controller adaptive to changing desired references, θ_{ref} is added to the Lyapunov function as seen in (7.23), which in turn leads to a more adaptive control law in (7.24).

$$V = \frac{1}{2}k_1 E^2 + \frac{1}{2}k_2(\theta - \theta_{ref})^2 + \frac{1}{2}k_3\dot{\theta}^2, \tag{7.23}$$

$$u_{fixed,ref} = \frac{2lm(gk_3 s_\theta + k_2 l\theta_{ref} - l(k_2\theta + K_4\dot{\theta}))}{2k_3 - 2gk_1 l^3 m^2 c_\theta + k_1 l^4 m^2 \dot{\theta}^2}. \tag{7.24}$$

The inverted pendulum can thus be driven to any desired angle during operation. This is important when the energy-based controller is applied to a robotic system such as a humanoid. During humanoid gait, the desired joint angles change throughout the gait cycles, and thus an adaptive controller will help in following the planned motion.

Inverted Pendulum on a Cart

The procedure is similar to that of the fixed inverted pendulum. The system is shown in Fig. 7.20, where m and M are the pendulum and cart masses respectively, l is the pendulum length, x is the linear displacement of the cart, θ is the pendulum angle, and u_{cart} is the control input force (in this case the force pushing the cart).

The vector of generalized coordinates is shown in (7.25). Kinetic and potential energies of the system are presented in (7.26) and (7.27) respectively, where g is the gravitational acceleration. The Lagrangian, L, is used to derive the equations of motion shown in (7.29).

$$q = \begin{pmatrix} x \\ \theta \end{pmatrix}, \tag{7.25}$$

$$KE = \frac{1}{2}M\dot{x}^2 + \frac{1}{2}m\dot{x}^2 + \frac{1}{2}ml^2\dot{\theta}^2 + ml(\cos\theta)\dot{\theta}\dot{x}, \tag{7.26}$$

$$PE = -mgl(\cos\theta), \tag{7.27}$$

$$L = \frac{1}{2}M\dot{x}^2 + \frac{1}{2}m\left(\dot{x}^2 + \frac{1}{2}l^2\dot{\theta}^2 + lc_\theta\dot{\theta}\dot{x}\right) + mglc_\theta, \tag{7.28}$$

$$(M+m)\ddot{x} + ml(\cos\theta)\ddot{\theta} - ml(\sin\theta)\dot{\theta}^2 = u_{cart},$$
$$l\ddot{\theta} + (\cos\theta)\ddot{x} + g(\sin\theta) = 0, \tag{7.29}$$

Solving (7.29) gives the expression of the linear acceleration.

$$\ddot{x} = \frac{u_{cart} + m\sin\theta(g\cos\theta + l\dot{\theta}^2)}{m + M - m(\cos\theta)^2}. \tag{7.30}$$

The chosen Lyapunov function to control the pendulum on a cart is shown in (7.31), where E is the total mechanical energy. It is clear that V is positive semi-definite as long as the gains k_1, k_2, and k_3 are non-negative.

$$V = \frac{k_1}{2}E^2 + \frac{k_2}{2}x^2 + \frac{k_3}{2}\dot{x}^2. \tag{7.31}$$

For V to be a proper candidate Lyapunov function and in order to ensure stability, $\dot{V}$ (shown in (7.32)) must be negative semi-definite.

$$\dot{V} = k_1 E\dot{E} + k_2 x\dot{x} + k_3\dot{x}\ddot{x}. \tag{7.32}$$

Taking advantage of the fact that $\dot{E} = \dot{x}u$ the expression of $\dot{V}$ can be simplified as:

$$\dot{V} = \dot{x}(k_1 E u_{cart} + k_2 x + k_3\ddot{x}). \tag{7.33}$$

In order to make sure that $\dot{V} \leq 0$ choose:

$$k_1 E u_{cart} + k_2 x + k_3\ddot{x} = -k_4\dot{x}, \tag{7.34}$$

where $k_4 \geq 0$. Solving (7.34) and replacing $\ddot{x}$ with its expression in (7.30) results in the following input:

$$u_{initial} = \frac{2(mc_{2\theta} - m - 2M)(k_2 x + k_4\dot{x}) - 2gk_3 ms_{2\theta} - k_3 lms_\theta\dot{\theta}^2}{4k_3 - (m + 2M - mc_{2\theta})D} \tag{7.35}$$

where $D = 2gk_1 lmc_\theta - k_1\left((m+M)\dot{x}^2 - 2lmc_\theta\dot{x}\dot{\theta} - l^2 m\dot{\theta}^2\right)$.
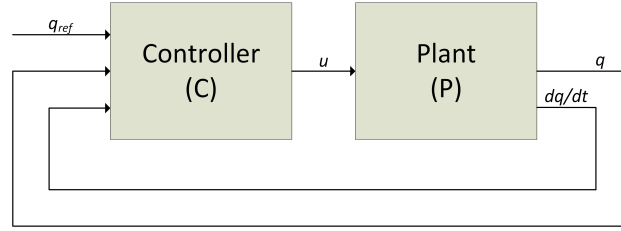
Figure 7.21: Generic block diagram for the three controllers

Table 7.4: Control Input Expressions for the Three Controllers

Controller (C)	Control input u of the Inverted Pendulum	
	Fixed	**On a Cart**
CL	$\dfrac{\left(\kappa\beta\sin\theta(\alpha\dot{\theta}^2+D\cos\theta)-c\left(\alpha-\left(\frac{\beta^2}{\gamma}\right)\cos\theta\right)^2\right)\left((\lambda(\kappa+1)+1)\beta\cos\theta\dot{\theta}\right)}{\alpha-\frac{\beta^2}{\gamma}(1+\kappa)(\cos\theta)^2}$	$\dfrac{\kappa\beta\sin\theta(\alpha\dot{\theta}^2+D\cos\theta)-c\left(\alpha-\left(\frac{\beta^2}{\gamma}\right)(\cos\theta)^2\right)\left((\lambda(\kappa+1)+1)\beta\cos\theta\dot{\theta}+\lambda\gamma\dot{x}\right)}{\alpha-\left(\frac{\beta^2}{\gamma}\right)(1+\kappa)(\cos\theta)^2}$
PID	$k_p + e(t)k_i \int e(t)dt + k_d\frac{de(t)}{dt}$	
EBC	$-\dfrac{2lm(-gk_3\sin\theta+k_2l\theta+k_4l\dot{\theta})}{2k_3-2gk_1l^3m^2\cos\theta+k_1l^4m^2\dot{\theta}^2}$	Refer to (26)

Since the pendulum's pivot is not actuated and there is no direct control over θ, the system's performance is improved by including proportional and derivative components at the angle and angular velocity of the inverted pendulum. The resulting control input becomes:

$$u_{cart} = u_{initial} + k_5\theta + k_6\dot{\theta}. \qquad (7.36)$$

The generic block diagram with controller C and plant P is depicted in Fig. 7.21, where u can take various values depending on the controller, as shown in Table 7.4.

7.4.2   System Analysis

In this section the controllability and stability of the inverted pendulum is tested in the fixed system and on a cart. In nonlinear systems one can test for a weaker form of controllability, which is the local strong accessibility [104]. This property is linked back to controllability in linear systems [104]. In order to prove local strong accessibility of a nonlinear system, it has to be proven that the matrix formed of the drift vector, the input vector, and their Lie bracket is of full rank [104].

First, the accessibility for the inverted pendulum on a cart is tested. The states are defined as $q = [x_1, x_2, x_3, x_4] = [\theta, \dot{\theta}, x, \dot{x}]$. The state space equations are then presented as:

$$\dot{x}_1 = x_2,$$

$$\dot{x}_2 = \frac{g(m + M)\sin x_1 + \cos x_1 \left(u + lm(\sin x_1)x_2^2\right)}{-l(m + M) + lm(\cos x_1)^2},$$

$$\dot{x}_3 = x_4, \tag{7.37}$$

$$\dot{x}_4 = \frac{u + m\sin x_1 \left(g\cos x_1 + lx_2^2\right)}{m + M - m(\cos x_1)^2},$$

In order to test accessibility, the states have to be written in terms of the drift and input vector fields $\dot{x} = g_1(x) + g_2(x)u$, with $g_1(x)$ and $g_2(x)$ as shown in (7.38) and (7.39) respectively.

$$g_1(x) = \begin{bmatrix} x_2 & \frac{g(m+M)\sin x_1 + \cos x_1\left(lm(\sin x_1)x_2^2\right)}{-l(m+M)+lm(\cos x_1)^2} & x_4 & \frac{m\sin x_1\left(g\cos x_1 + lx_2^2\right)}{m+M-m(\cos x_1)^2} \end{bmatrix} \tag{7.38}$$

$$g_2(x) = \begin{bmatrix} 0 & \frac{\cos x_1}{-l(m+M)+lm(\cos x_1)^2} & 0 & \frac{1}{m+M-m(\cos x_1)^2} \end{bmatrix} \tag{7.39}$$

The Lie bracket formed by the two vector fields is calculated as:

$$[g_1(x), g_2(x)] = \frac{\partial g_2}{\partial x}g_1(x) - \frac{\partial g_1(x)}{\partial x}g_2(x). \tag{7.40}$$

Since the rank of the matrix formed by the three vectors is three, then the system is considered to be locally strong accessible. The same proof applies to the fixed inverted pendulum. The state vector and state equations are written in (7.41) and (7.42).

$$q = [x_1, x_2] = \left[\theta, \dot{\theta}\right], \tag{7.41}$$

$$\dot{x}_2 = \frac{u - glm\sin x_1}{l^2m}. \tag{7.42}$$

The corresponding drift and input vector fields are shown in (7.43) and (7.44) respectively. The Lie bracket of the previously mentioned vectors is calculated as done in (7.40).

$$g_1(x) = \left[x_2, \frac{-g\sin x_1}{l}\right], \tag{7.43}$$

$$g_2(x) = \left[0, \frac{1}{l^2m}\right]. \tag{7.44}$$

The matrix formed of $g_1(x)$, $g_2(x)$, and $g_1g_2(x)$ is full rank of two, which indicates that the system is locally strong accessible.

Table 7.5: Gain Parameters of the Three Controllers for the Simulations and Experiments

Controller	Parameter Values												
	EBC						Controlled Lagrangian				PID		
	k_1	k_2	k_3	k_4	k_5	k_6	λ	κ	b	c	k_p	k_i	k_d
Fixed IP simulation	0.5	120	50	280	-	-	0.01	2460	0.1	50	10.1	1.8	15
IP on a cart simulation	0.1	100	50	300	20	1	0.05	424	0.3	40	-3.9	-2.5	-0.55
Fixed IP experimental	0.1	2	1	5	-	-	0.01	964	0.15	45	0.1	1	0.01
Humanoid simulation	0.5	150	55	220	-	-	0.01	0.005	0.2	53	10.2	7.5	12.4

The Lyapunov Energy-Based Control (EBC) ensures local stability as long as the derivative $\dot{V}$ of the candidate Lyapunov function is negative semi-definite. Since the chosen control law for both the fixed inverted pendulum and the one on a cart is based on keeping $\dot{V}$ negative semi-definite, then this guarantees local stability for the two systems. Even in the adaptive fixed inverted pendulum, the systems stability is ensured since the reference angle is included in the Lyapunov function without disturbing the negative semi-definite property.

7.4.3 Simulation and Experimental Results-Inverted Pendulum

In this section, the energy-based controller is implemented and validated in MAT-LAB/Simulink simulations for the inverted pendulum in the fixed state and on a cart and in experiments on the Quanser QUBE-Servo for the fixed inverted pendulum.

The energy-based controller is compared to the PID control and the controlled Lagrangian approaches. The controller parameters for the tested scenarios are shown in Table 7.5, where the first two rows present the gains for the simulations of the fixed inverted pendulum and the one on a cart. The third and fourth row present the gains for the fixed pendulum experiments and the humanoid simulations respectively. The comparison metrics used are the maximum overshoot, settling time, peak input force, and cumulative work.

The work done to bring the fixed inverted pendulum and the one on a cart into the upright position is calculated using (7.45) and (7.46) respectively.

$$Work_{oncart} = |\Delta x \cdot u|, \tag{7.45}$$

$$Work_{fixed} = |\Delta \theta \cdot u|. \tag{7.46}$$

The metric used to compare energy expenditure between the different controllers is the cumulative work.

$$CumulWork = \int_0^{t_f} Work \; dt. \qquad (7.47)$$

7.4.4 Simulation Results of the Fixed Inverted Pendulum

The fixed pendulum angle variation for the three controllers is shown in Fig. 7.22 while the applied torque is shown in Fig. 7.23. The energy-based controller brings the fixed inverted pendulum to the equilibrium position with no overshoot, contrary to the other two controllers. While it requires 11.33 seconds longer as a settling time than the traditional PID controller, it needs 103.5 N less peak torque input (10 N less compared to the Controlled Lagrangian). The energy-based controller also requires less work to reach stability than the other two controllers (around three times less than the nearest controller). The performance results of the three controllers are shown in Table 7.6.

Table 7.6: Performance Metrics for the Three Controllers of the Fixed Inverted Pendulum

Controller	Performance Metrics			
	θ overshoot (rad.)	θ settling time (sec.)	|Peak input torque|(N)	Cumulative Work (N.rad.)
CL	-0.081	47.000	10.230	10.790
PID	-0.123	0.277	103.700	981.000
EBC	No Overshoot	11.610	0.248	3.180

7.4.5 Simulation Results of the Inverted Pendulum on a Cart

The simulations are done in Simulink and the model parameter values for the inverted pendulum are shown in Table 7.7. The controllers are tested for an initial angular displacement of 1.0472 rad which is the same angle used in the literature to test the Controlled Lagrangian and PID controllers [105, 106]. The weight parameters are for tuning and at this stage they are being tuned manually while conforming to the constraints set by the Lyapunov function.

The controllers are compared based on angle displacement, control input magnitude, and cumulative work done. Fig. 7.24 shows the pendulum angle variation of the inverted pendulum on a cart for the three controllers. While the EBC leads
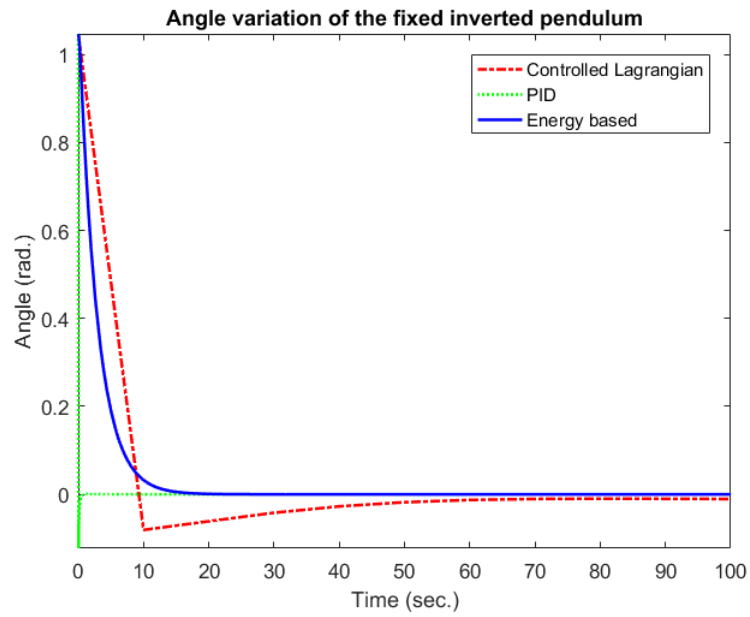
Figure 7.22: Angle variation of the fixed inverted pendulum
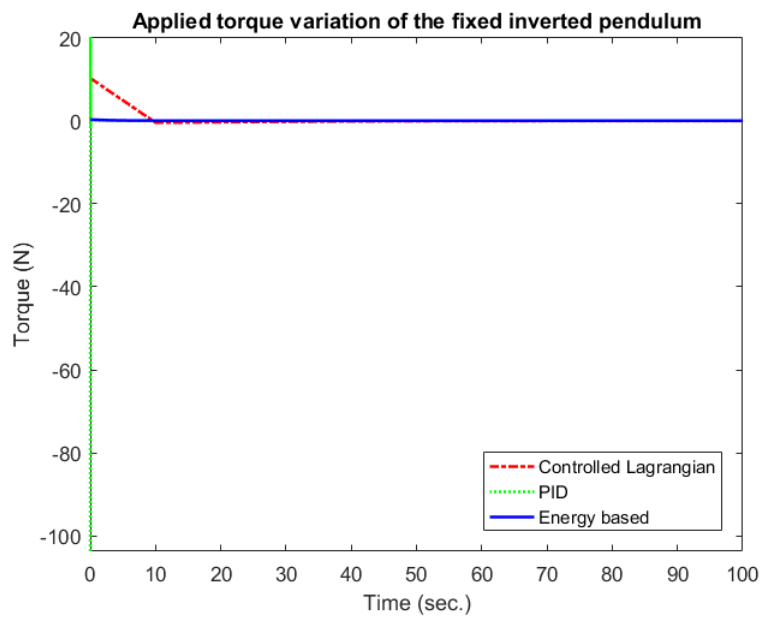
Figure 7.23: Torque variation of the fixed inverted pendulum

Table 7.7: Parameter Values - Inverted Pendulum on a Cart

Parameter	Value
M	0.44 kg
m	0.14 kg
l	0.215 m
g	9.81 m/s^2
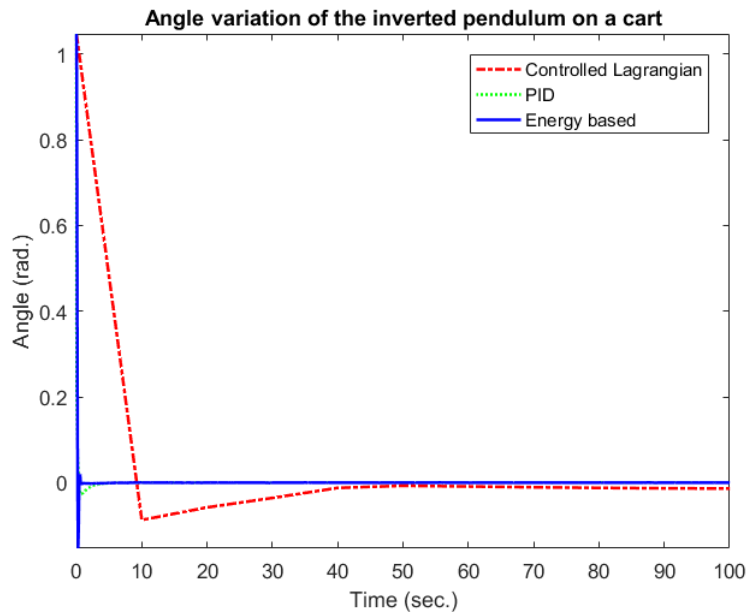
Figure 7.24: Angle displacement variation for the inverted pendulum on a cart

to a slightly higher overshoot, it has a faster settling time than the other two controllers. The exact numerical statistics are presented in Table 7.8.

The input force variation for the three controllers is shown in Fig. 7.25. For a clearer presentation of the results, the comparison is shown in Table 7.8. The energy-based controller offers a compromise between the excessive peak input force required by the PID controller and the minimal force required by the Controlled Lagrangian approach. This is done while ensuring the least amount of cumulative work done to achieve stability of the inverted pendulum in the upright position. The energy-based controller shows 3974.7 N less peak input force than the PID controller and 10.2 N more peak input force than the Controlled Lagrangian. The cumulative work comparison is shown in Table 7.8, where the energy-based spends the least work with 4.0323 N.m. and the closest controller (Controlled Lagrangian) spending 2261 N.m. proving a significant improvement. It is important to note that the results are subject to controller gain tuning and

83

Table 7.8: Performance Metrics for the Three Controllers of the Inverted Pendulum on a Cart

Controller	Performance Metrics			
	θ overshoot (rad.)	θ settling time (sec.)	|Peak input force|(N)	Cumulative Work (N.m.)
CL	-0.087	36.000	10.197	2261.000
PID	0.028	1.281	3995.000	1.664e+7
EBC	-0.153	0.461	20.349	4.032
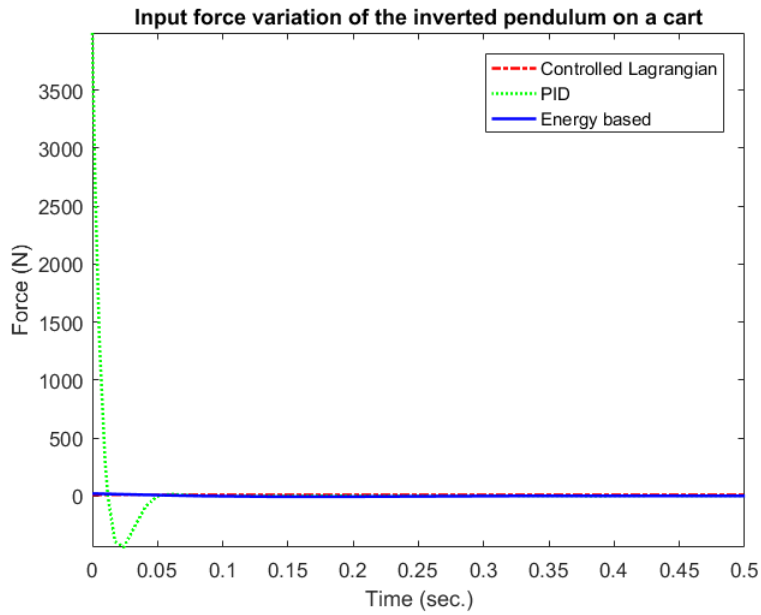
Figure 7.25: Input force variation for the inverted pendulum on a cart

extensive iterations were done to find the best gains for each controller used for comparison.

7.4.6 Experimental Results of the Fixed Inverted Pendulum

The EBC is tested on the QUBE-Servo inverted pendulum (Fig. 7.26) and compared to the Controlled Lagrangian and PID control algorithms. The inverted pendulum is subjected to an impact from a ball released from a consistent angle. The parameter values guiding the experimental setup are shown in Table 7.9, where m_p is the pendulum, l_p is the pendulum length, m_b is the mass of the ball, and l_r is the rope's length.

84

Figure 7.26: Experimental Setup

Table 7.9: Parameter Values of the Experimental Setup

Parameter	Value
m_p	0.05487 kg
l_p	0.144 m
m_b	23.28 g
l_r	0.167 m
g	9.81 m/s^2
$\theta_{release}$	34.7°

Table 7.10: Performance Metrics for the Three Controllers of the Fixed Inverted Pendulum Experiments

Controller	Performance Metrics			
	θ overshoot (rad.)	θ settling time (sec.)	|Peak input torque|(N)	Cumulative Work (N.rad.)
CL	0.052	2.35	0.273	0.812
PID	0.122	3.968	0.046	0.632
EBC	0.141	5.438	0.001	0.551

The swaying angle, input torque, and cumulative exerted work of the pendulum are measured and plotted for a response to the impact with the released ball. The ball release represents an impulse disturbance or a push disturbance as will be shown in the following section. The numerical results are listed in Table 7.10.

The angle variation of the inverted pendulum can be seen in Fig. 7.27. The EBC leads to more swaying time and higher swaying angle (0.141 rad compared to 0.052 rad of the Controlled Lagrangian) than the PID and Controlled Lagrangian methods but this is due to the low energy expenditure constraint put on the proposed controller.

The increase in swaying angle and settling time (3.088 seconds longer than the fastest controller) is reflected in the low input torque needed by the energy-based controller to achieve stability of the inverted pendulum in the upright position (Fig. 7.28).

Regarding the cumulative work expenditure, which is the main goal behind introducing the energy-based approach the results are shown in Fig. 7.29. Energy-based control ensures stability with 14.7% less work than the PID controller and 47.4% less work than the Controlled Lagrangian. The improvement in experiments are less than those in simulation as the hardware used doesn't support high torques. In simulation more freedom was available in the torque input range.

7.4.7 Humanoid Push Recovery Simulations

The motivation behind the energy-based controller design was to implement it on humanoid robots in quiet stance and during gait. The previous simulations and experiments were done on the inverted pendulum model since humanoids are usually modeled as inverted pendulums to simplify the control and motion planning process.

The three controllers covered in this section are simulated on the Nao H25 V5.0 humanoid in Webots against a 20N push disturbance in the sagittal plane as seen in Fig. 7.30. The 20N push is considered a strong disturbance given that the controllers are applying the ankle strategy while all other joints are locked.
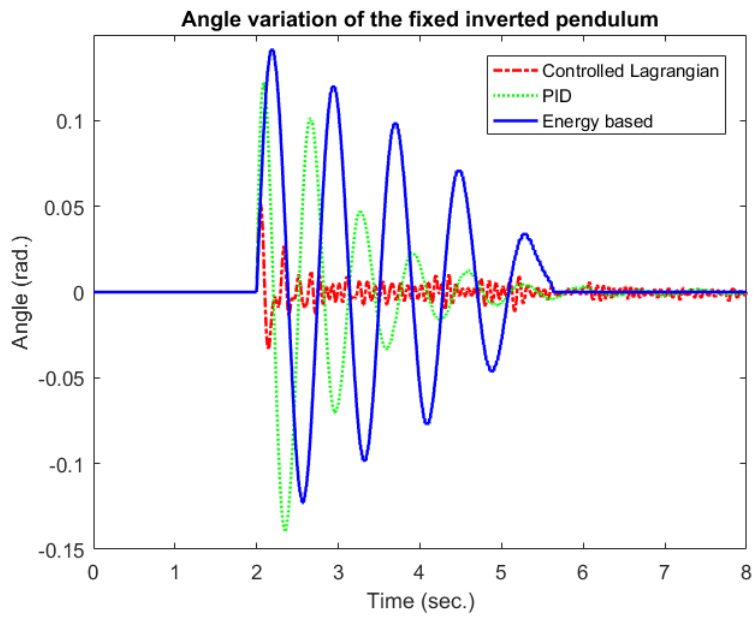
Figure 7.27: Angle variation of the fixed inverted pendulum while recovering from the ball impact
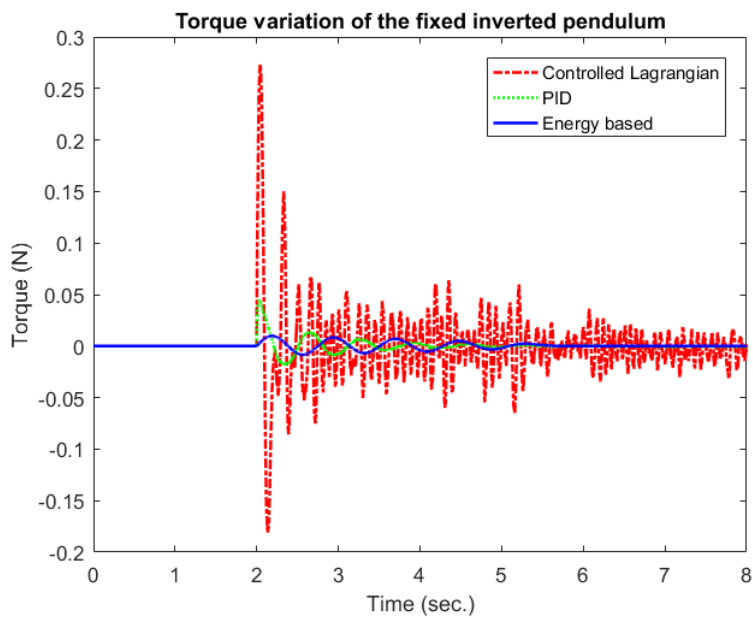
Figure 7.28: Input torque variation of the fixed inverted pendulum while recovering from the ball impact
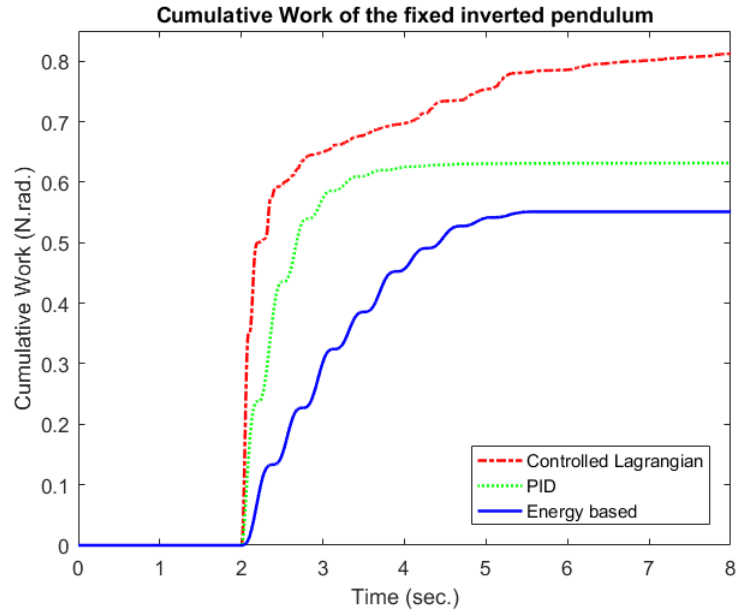
Figure 7.29: Cumulative work expenditure of the fixed inverted pendulum while recovering from the ball impact

Nao is modeled as a fixed inverted pendulum actuated at the ankle joints in the sagittal plane with its feet fixed on the ground (no foot rotation). The response is plotted for analysis and the performance metrics are listed in Table 7.11.

The swing angle variation of Nao is shown in Fig. 7.31 while recovering from the push disturbance for each of the three controllers. The plots show a 253% improvement when using the energy-based controller as compared to the closer control algorithm which is the Controlled Lagrangian method. The energy-based approach also improves the settling time as compared to the other two controllers.

The energy-based controller also improves the required input torque to recover from the push disturbance. While the PID controller requires a peak torque of 82.36 N and the Controlled Lagrangian method requires 15.92 N, the energy-based approach needs only 0.79 N to recover from the same push disturbance. The input torque plots for the three controllers are shown in Fig. 7.32.

In order to compare the energy expenditure during push recovery, Webots offers torque feedback calculations which reflect the energy expenditure and battery consumption of the motors at the ankle joint. Fig. 7.33 shows the cumulative feedback torque plots for the three controllers. The energy-based approach proves to be 5.4% more energy-efficient than the PID controller and 142.7% more efficient than the Controlled Lagrangian approach.

The energy-based controller outperforms the PID and Controlled Lagrangian approaches in energy expenditure and cumulative work when tested in simulation and experiments. It also outperformed them in peak input force and angle
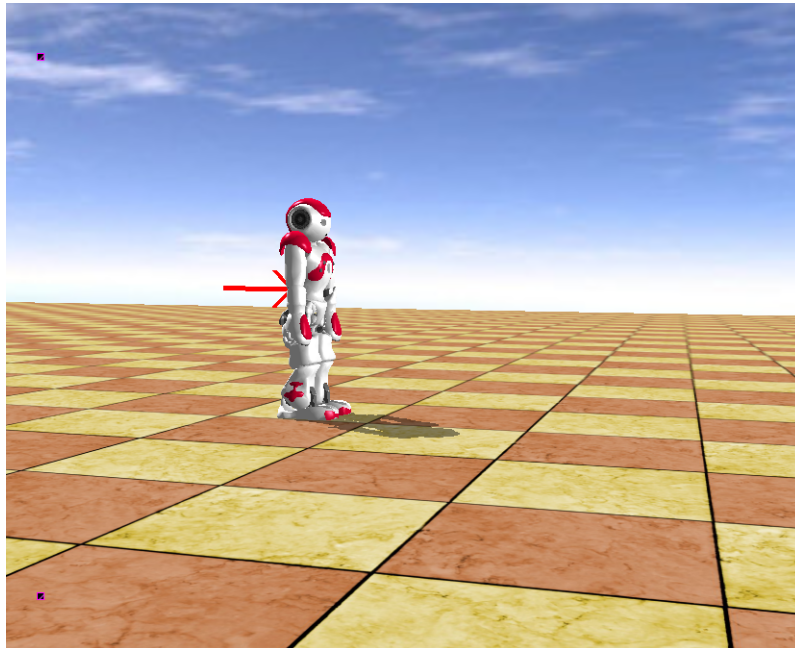
Figure 7.30: Webots simulation setup on Nao humanoid
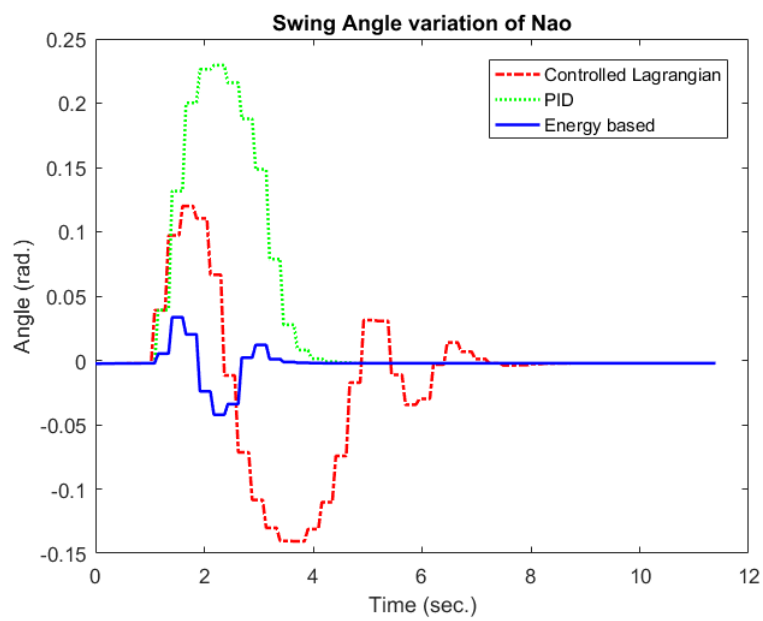
Figure 7.31: Angle variation of Nao while recovering from a 20N push
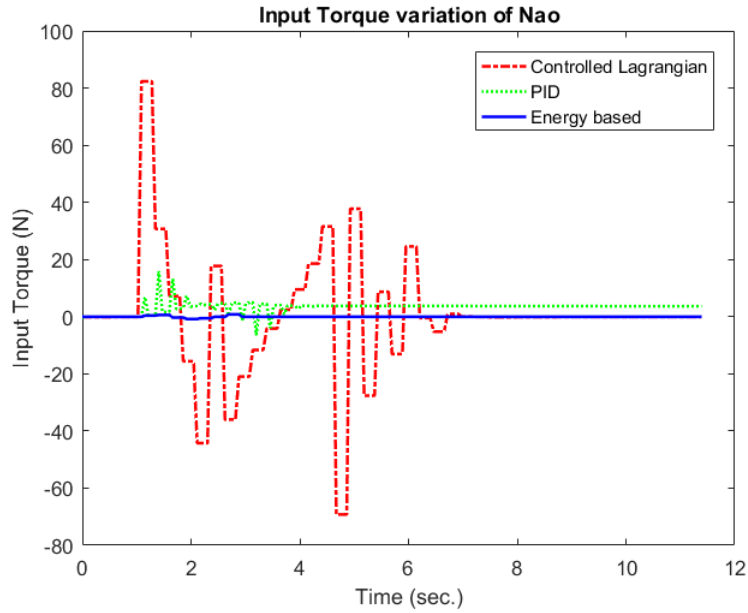
Figure 7.32: Input torque at Nao's ankle joints while recovering from a 20N push

Table 7.11: Performance Metrics - Nao Push Recovery

Controller	Performance Metrics			
	θ overshoot (rad.)	θ settling time (sec.)	|Peak input torque|(N)	Cumulative Work (N.rad.)
CL	0.120	6.208	82.360	128.900
PID	0.230	3.712	15.920	55.880
EBC	0.034	2.944	0.788	53.110

overshoot when simulated in Simulink and Webots on Nao. However, in the experiments on the Quanser QUBE Servo, the energy-based control had higher overshoot than its competitors. This may be due to the fact that the pendulum's inertia is not included in the equations of motion and thus affected the performance in the experiments. Nevertheless, the proposed controller was still capable of maintaining equilibrium in a more energy-efficient manner.

7.5 Energy-Based Humanoid Gait

The EBC developed in the previous section is applied to the new gait generation algorithm since the EBC proved to require less torque in comparison with traditional controllers. Instead of relying on the PID controller which is set by
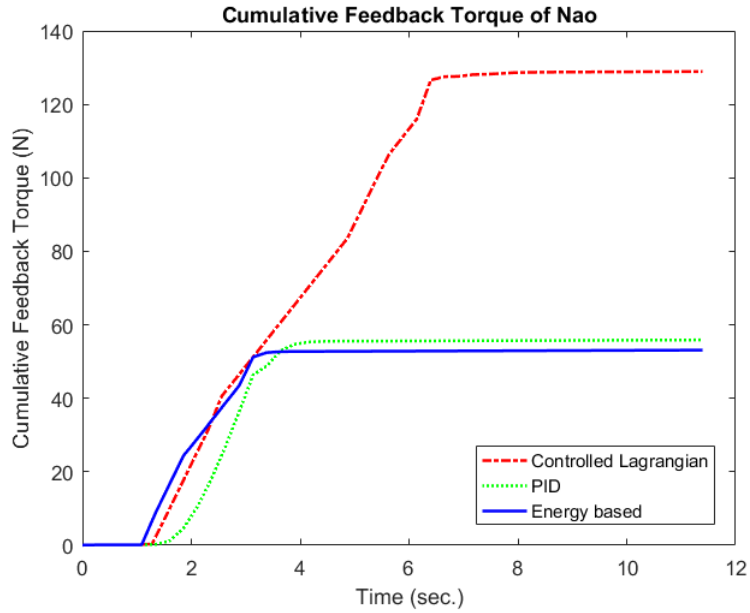
Figure 7.33: Cumulative feedback torque at Nao's ankle joints while recovering from a 20N push

default in Webots, EBC is applied along with the newly derived gait angles based on energy-exchange. Therefore, there is an EBC at each joint of the humanoid to obtain the desired gait angle at each step of the gait cycle. As in the previous simulations, Hoap2 walks at a speed of 0.025 m/s. The effect of using EBC along with energy-exchange gait angles is evaluated through the analysis of energy patterns and average torques exerted at the actuated joints.

The kinetic and potential energies at the humanoid's CoM during the new gait are shown in Fig. 7.34 to validate the energy-exchange property. The use of EBC exerts less torque at the torso compared to that needed with the standard PID controller (Fig. 7.35). Similar improvements are evident on the thighs and shanks as shown in Fig. 7.36 and Fig. 7.37, provided that the same energy-exchange gait angles are applied and the only difference is in the controllers used.

Averages of the absolute values of torques exerted at each link in both PID and EBC are summarized in Table 7.12. The average torque can be used as an indicator since both gaits are applied at the same constant speed with the same target angles. The Energy-Based Controller leads to 39.6% improvement in torque exerted at the torso, 55.3% less torque at the thighs, and 3.5% improvement at the shanks.

The total mechanical energy during the energy-exchange gait under EBC has an average of 18.8 J which is about 1% less than the energy during the use of PID control. The overall Lagrangian of the gait under both controllers is shown in Fig. 7.38. The improvement in energy-efficiency of the proposed controller (EBC) is

91
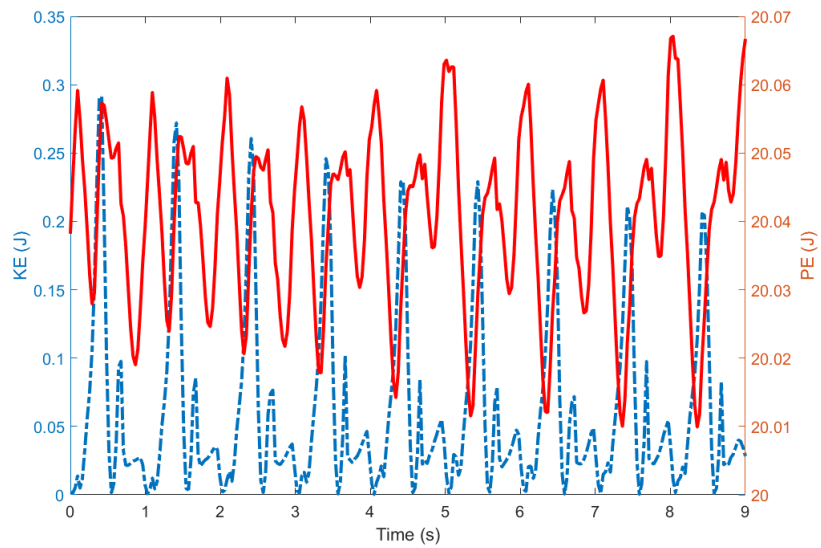
Figure 7.34: KE and PE patterns of Hoap2 CoM during new energy-exchange gait with EBC
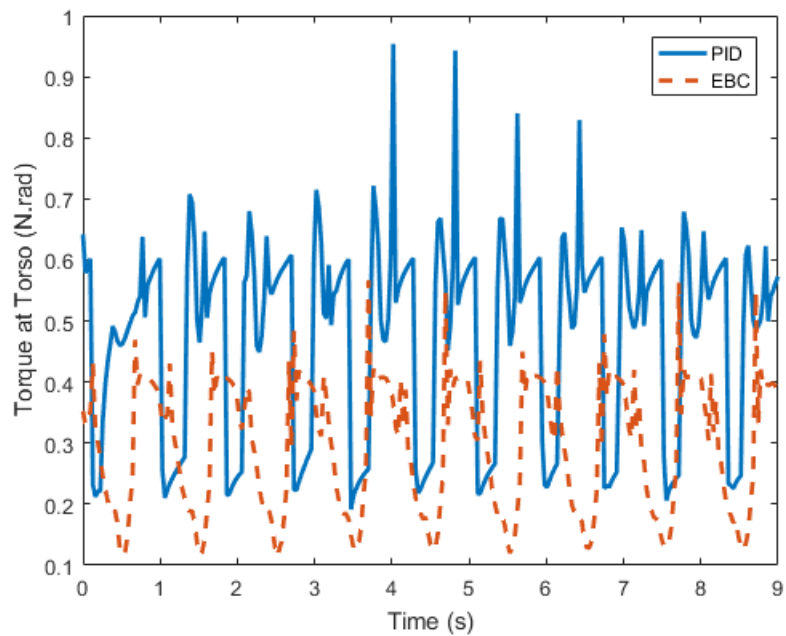
Figure 7.35: Torque exerted at the torso during energy-exchange gait with PID control (blue) and EBC (red dashed)
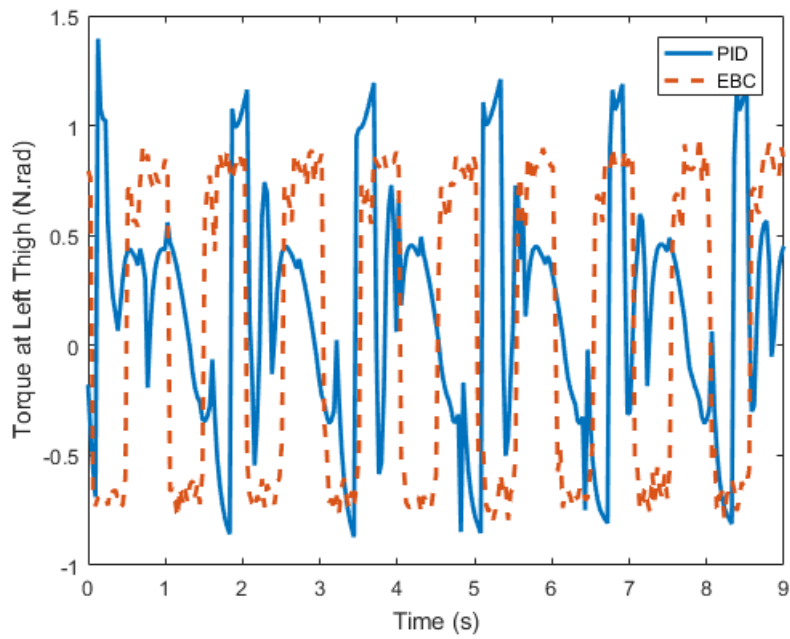
Figure 7.36: Torque exerted at the left thigh during energy-exchange gait with PID control (blue) and EBC (red dashed)
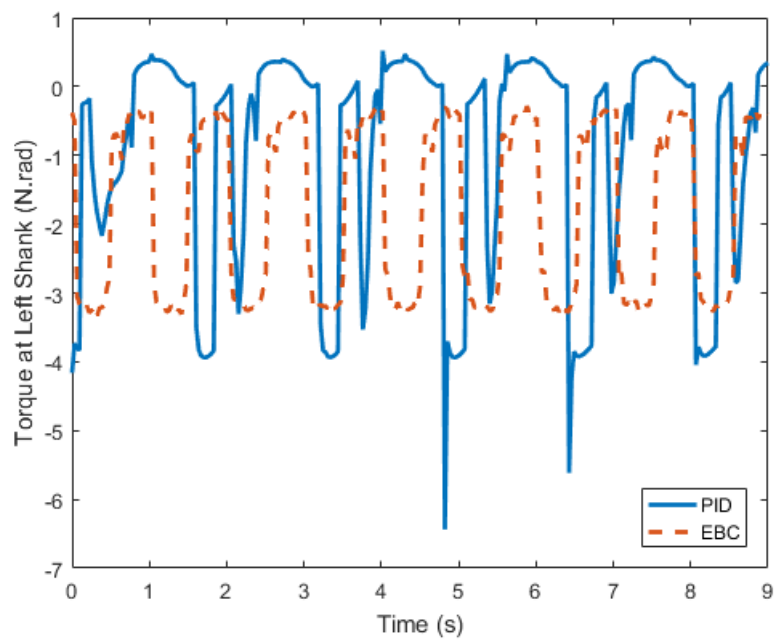
Figure 7.37: Torque exerted at the left shank during energy-exchange gait with PID control (blue) and EBC (red dashed)

Table 7.12: Average torque exerted at each link during energy-exchange gait with standard PID control and EBC.

Controller	Average Torque (absolute values) N rad		
	Torso	Thigh	Shank
PID	0.48	0.47	1.15
EBC	0.29	0.21	1.11
% Improvement	39.6%	55.3%	3.5%
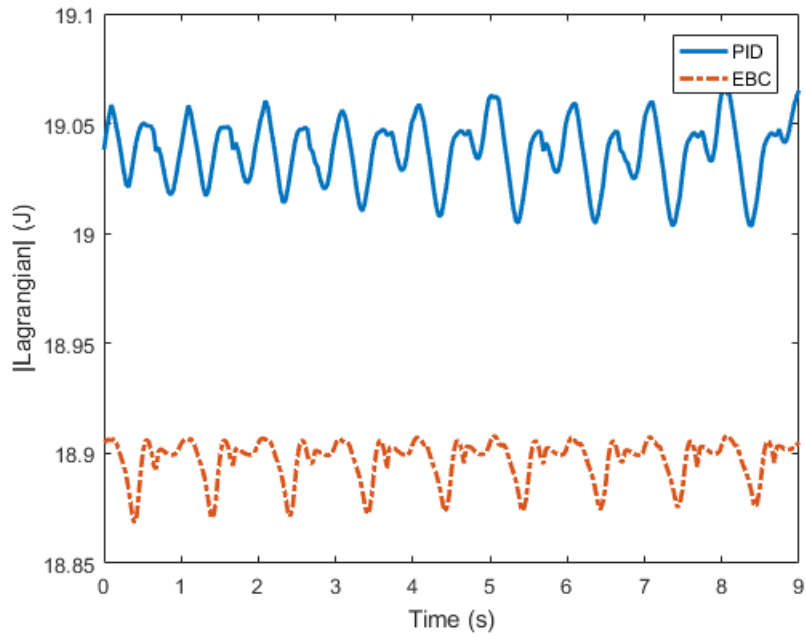
Figure 7.38: Overall Absolute Lagrangian during energy-exchange gait with standard PID control (blue) and EBC (red dashed)

evident in the smaller variations of the Lagrangian (maximum difference between peaks is 0.04) as compared to the slightly larger variations in the standard gait (maximum difference is 0.06).

The proposed control strategy also increases robustness against push disturbances during single stance in the sagittal plane (up to 16.5 N.m) and the lateral plane (up to 11 N.m). This shows 10 % improvement in disturbance rejection in both planes when using EBC as compared to standard PID control.

Chapter 8

Conclusion and Future Work

8.1 Conclusion

In this thesis a human-inspired mechanism for humanoid fall avoidance and stable gait generation was presented. The sensory reweighting algorithm improved the role of visual sensing in humanoid fall avoidance during quiet standing. Through dynamically varying the degree of reliance on each sensor the robot is able to maintain balance in different environments and in unforeseen circumstances. The experimental scenarios described in the previous section demonstrate that the sensory reweighting system performs better in terms of the magnitude of the ankle torque as well as the settling time in the angular displacement. The use of proprioceptive sensory inputs increases the robot's ability to reject disturbances of higher magnitudes regardless of the disturbance direction and location. The model-free push recovery scheme improves the response time and resistance to disturbances of higher magnitude compared to traditional fall avoidance strategies. The results are validated both in simulations and by conducting experiments on the actual Nao.

This thesis also contributed in the development of human-like walking on small-scale commercial humanoid robots. This became possible through the development of the energy-exchange gait. The walking algorithm is inspired by a theory in Kinesiology which guides human walking. In addition to the gait synthesis, a new Energy-Based Controller is developed to enforce the energy-exchange property in humanoid walking. The new proposed gait was shown to be more energy-efficient than the standard gait. The energy conscious gait is also more stable against push disturbances in the sagittal and lateral planes during the most vulnerable phase of the gait cycle which is single stance.

8.2 Future Work

The work done in this thesis formulated an understanding of the importance of studying human behavior comprehensively. The clear understanding of the characteristics that guide human behavior lays the foundation for a strong humanoid maneuverability and stability. The focus in this thesis was on mimicking the intuition behind human stability and walking. A suggested approach for future research is more of a design path where the humanoid joints and limbs are manufactured to resemble those of humans.

While this thesis presented a number of solutions to the problem of small-scale humanoid stability and gait design, it opens the door to many areas of interest that are worth investigating in the future. The main points of interest for future work are listed below.

- The inclusion of environment perception in assessing the humanoid's posture and possibilities of recovery from push disturbances. For example, vision is not only useful in differentiating between ego-motion and a moving environment. It could be used to identify objects in the environment that could aid in maintaining balance (e.g. a wall to lean on).

- The enhancement of proprioceptive sensors on small-scale humanoid robots by adding force-sensing skins could improve the estimation of disturbance magnitudes, direction, and point of contact.

- The study of the effect of human running on the energy-exchange property and whether it holds under different patterns of running. This would present an important step in developing complex maneuvers on small-scale humanoid robots with limited physical capabilities.

- The application of energy-exchange gait on exoskeletons in order to correct the walk of people with disabilities, and increase energy-efficiency.

- The study of the arm movements during human gait and fall avoidance. While the arms are used for fall management and preventing damage to other body parts, they also play a role in maintaining balance. A simple example is the extension of the arms while walking on a narrow edge.

- The use of proprioceptive sensors for adapting the energy-exchange gait to different terrain types. The current gait synthesis requires even terrains for successful walking. Adding a stage of calibration before walking helps in detecting terrain types and adjusting the gait generation process. The terrain type would be estimated using the robot's foot pressure sensors. In this case, the proprioceptive information obtained could be used to enable model-free control on the stance foot during energy-exchange gait in uneven terrains.

Appendix A

Abbreviations

CL	Controlled Lagrangian
CoG	Center of Gravity
CoM	Center of Mass
DoF	Degree of Freedom
EBC	Energy-Based Control
EMG	Electromyography
EP	Equilibrium Point
ERP	Event-Related Potential
FSR	Force Sensitive Resistor
HSV	Hue-Saturation-Value
IMU	Inertial Measurement Unit
KE	Kinetic Energy
LIPM	Linear Inverted Pendulum Model
ME	Mechanical Energy
PE	Potential Energy
PID	Proportional Integral Derivative
RANSAC	RANdom SAmple Consensus
SLAM	Simultaneous Localization and Mapping
VMC	Virtual Model Control
ZMP	Zero Moment Point

Bibliography

[1] "Nao robot — design & architecture — pinterest — robot, humanoid robot and robot design."

[2] A. Hallemans, P. Aerts, B. Otten, P. P. De Deyn, and D. De Clercq, "Mechanical energy in toddler gait a trade-off between economy and stability?," *Journal of experimental biology*, vol. 207, no. 14, pp. 2417–2431, 2004.

[3] B. Jalgha, D. Asmar, and I. Elhajj, "A hybrid ankle/hip preemptive falling scheme for humanoid robots," in *Robotics and Automation (ICRA), 2011 IEEE International Conference on*, pp. 1256–1262, IEEE, 2011.

[4] D. Hobbelen, T. De Boer, and M. Wisse, "System overview of bipedal robots flame and tulip: Tailor-made for limit cycle walking," in *Intelligent Robots and Systems, 2008. IROS 2008. IEEE/RSJ International Conference on*, pp. 2486–2491, IEEE, 2008.

[5] P. Cominoli, "Development of a physical simulation of a real humanoid robot," *Diploma Thesis, BIRG, Logic Systems Laboratory, School of Computer and Communication Sciences, Swiss Federal Institute of Technology*, 2005.

[6] M. Nardini, D. Cowie, A. Bremner, D. Lewkowicz, and C. Spence, "The development of multisensory balance, locomotion, orientation and navigation," *Multisensory development. Oxford University Press, Oxford*, pp. 137–158, 2012.

[7] R. Peterka, "Sensorimotor integration in human postural control," *Journal of neurophysiology*, vol. 88, no. 3, pp. 1097–1118, 2002.

[8] F. B. Horak, "Postural orientation and equilibrium: what do we need to know about neural control of balance to prevent falls?," *Age and ageing*, vol. 35, no. suppl_2, pp. ii7–ii11, 2006.

[9] K. A. Tahboub, "Biologically-inspired humanoid postural control," *Journal of Physiology-Paris*, vol. 103, no. 3-5, pp. 195–210, 2009.

[10] D. A. Winter, "Human balance and posture control during standing and walking," *Gait & posture*, vol. 3, no. 4, pp. 193–214, 1995.

[11] D. A. Winter, A. E. Patla, and J. S. Frank, "Assessment of balance control in humans," *Med Prog Technol*, vol. 16, no. 1-2, pp. 31–51, 1990.

[12] S. Jo, *Hierarchical neural control of human postural balance and bipedal walking in sagittal plane*. PhD thesis, Massachusetts Institute of Technology, 2006.

[13] J. Rodin and E. Langer, "Aging labels: The decline of control and the fall of self-esteem," *Journal of Social Issues*, vol. 36, no. 2, pp. 12–29, 1980.

[14] S. Hwang, P. Agada, T. Kiemel, and J. J. Jeka, "Dynamic reweighting of three modalities for sensor fusion," *PloS one*, vol. 9, no. 1, p. e88132, 2014.

[15] S. Thorpe, D. Fize, and C. Marlot, "Speed of processing in the human visual system," *nature*, vol. 381, no. 6582, p. 520, 1996.

[16] T. J. Szabo and J. B. Welcher, "Human subject kinematics and electromyographic activity during low speed rear impacts," tech. rep., SAE Technical Paper, 1996.

[17] B. L. Day and M. Guerraz, "Feedforward versus feedback modulation of human vestibular-evoked balance responses by visual self-motion information," *The Journal of physiology*, vol. 582, no. 1, pp. 153–161, 2007.

[18] S. Park, F. B. Horak, and A. D. Kuo, "Postural feedback responses scale with biomechanical constraints in human standing," *Experimental brain research*, vol. 154, no. 4, pp. 417–427, 2004.

[19] S. Kim, C. G. Atkeson, and S. Park, "Perturbation-dependent selection of postural feedback gain and its scaling," *Journal of biomechanics*, vol. 45, no. 8, pp. 1379–1386, 2012.

[20] B. E. Maki and W. E. McIlroy, "The role of limb movements in maintaining upright stance: the change-in-support strategy," *Physical therapy*, vol. 77, no. 5, pp. 488–507, 1997.

[21] C. A. Oatis *et al.*, *Kinesiology: the mechanics and pathomechanics of human movement*. Lippincott Williams & Wilkins Philadelphia, 2004.

[22] P. López-Miñarro, J. Muyor, F. Alacid, and P. Rodríguez, "Influence of sport training on sagittal spinal curvatures," *Posture: Types, assessment and control*, pp. 63–98, 2011.

[23] D. S. Marigold, A. J. Bethune, and A. E. Patla, "Role of the unperturbed limb and arms in the reactive recovery response to an unexpected slip during locomotion," *Journal of neurophysiology*, vol. 89, no. 4, pp. 1727–1737, 2003.

[24] J. K. Aggarwal and Q. Cai, "Human motion analysis: A review," *Computer vision and image understanding*, vol. 73, no. 3, pp. 428–440, 1999.

[25] N. P. Hamilton, *Kinesiology: scientific basis of human motion.* Brown & Benchmark, 2011.

[26] J. Perry, J. R. Davids, *et al.*, "Gait analysis: normal and pathological function," *Journal of Pediatric Orthopaedics*, vol. 12, no. 6, p. 815, 1992.

[27] J. Crosbie, R. Vachalathiti, and R. Smith, "Patterns of spinal motion during walking," *Gait & Posture*, vol. 5, no. 1, pp. 6–12, 1997.

[28] E. Uyar, O. Baser, R. Baci, and E. Özçivici, "Investigation of bipedal human gait dynamics and knee motion control," *Izmir, Turkey: Dokuz Eylül University-Faculty of Engineering Department of Mechanical Engineering. Retrieved August,* 2009.

[29] A. G. Feldman, "Origin and advances of the equilibrium-point hypothesis," in *Progress in motor control,* pp. 637–643, Springer, 2009.

[30] A. G. Feldman and M. F. Levin, "The equilibrium-point hypothesis–past, present and future," in *Progress in motor control,* pp. 699–726, Springer, 2009.

[31] M. L. Latash, "The bliss (not the problem) of motor abundance (not redundancy)," *Experimental brain research*, vol. 217, no. 1, pp. 1–5, 2012.

[32] Z. Wang, J. H. Ko, J. H. Challis, and K. M. Newell, "The degrees of freedom problem in human standing posture: collective and component dynamics," *PloS one*, vol. 9, no. 1, p. e85414, 2014.

[33] V. G. Ivancevic and T. T. Ivancevic, *Human-like biomechanics: a unified mathematical approach to human biomechanics and humanoid robotics,* vol. 28. Springer Science & Business Media, 2008.

[34] G. A. Cavagna, N. C. Heglund, and C. R. Taylor, "Mechanical work in terrestrial locomotion: two basic mechanisms for minimizing energy expenditure," *American Journal of Physiology-Regulatory, Integrative and Comparative Physiology*, vol. 233, no. 5, pp. R243–R261, 1977.

[35] S. Kajita, F. Kanehiro, K. Kaneko, K. Yokoi, and H. Hirukawa, "The 3d linear inverted pendulum mode: A simple modeling for a biped walking pattern generation," in *Intelligent Robots and Systems, 2001. Proceedings. 2001 IEEE/RSJ International Conference on*, vol. 1, pp. 239–246, IEEE, 2001.

[36] D. Adams, "Cga normative gait database," June 2013.

[37] S. Lim, S. Oh, and K. I. Kim, "Balance control for biped walking robots using only zero-moment-point position signal," *Electronics letters*, vol. 48, no. 1, p. 1, 2012.

[38] M. Vukobratović and B. Borovac, "Zero-moment pointthirty five years of its life," *International journal of humanoid robotics*, vol. 1, no. 01, pp. 157–173, 2004.

[39] A. Mahboobin, P. J. Loughlin, M. S. Redfern, S. O. Anderson, C. G. Atkeson, and J. K. Hodgins, "Sensory adaptation in human balance control: lessons for biomimetic robotic bipeds," *Neural Networks*, vol. 21, no. 4, pp. 621–627, 2008.

[40] T. J. Klein, J. Jeka, T. Kiemel, and M. A. Lewis, "Navigating sensory conflict in dynamic environments using adaptive state estimation," *Biological cybernetics*, vol. 105, no. 5-6, pp. 291–304, 2011.

[41] M.-A. N. Mahani, S. Jafari, and H. Rahmatkhah, "A novel approach for humanoid push recovery using stereopsis," *Robotica*, vol. 32, no. 3, pp. 413–431, 2014.

[42] B. Jalgha, D. Asmar, E. Shammas, and I. Elhajj, "Hierarchical fall avoidance strategy for small-scale humanoid robots," in *Robotics and Biomimetics (ROBIO), 2012 IEEE International Conference on*, pp. 1–7, IEEE, 2012.

[43] D. C. Asmar, B. Jalgha, and A. Fakih, "Humanoid fall avoidance using a mixture of strategies," *International Journal of Humanoid Robotics*, vol. 9, no. 01, p. 1250002, 2012.

[44] J. Rebula, F. Canas, J. Pratt, and A. Goswami, "Learning capture points for humanoid push recovery," in *Humanoid Robots, 2007 7th IEEE-RAS International Conference on*, pp. 65–72, IEEE, 2007.

[45] L. Colasanto, N. G. Tsagarakis, and D. G. Caldwell, "A compact model for the compliant humanoid robot coman," in *Biomedical Robotics and Biomechatronics (BioRob), 2012 4th IEEE RAS & EMBS International Conference on*, pp. 688–694, IEEE, 2012.

[46] H.-J. Byun and S. G. Shon, "Application of imitation control and foot sensors to bipedal robot walking," *International Journal of Control and Automation*, vol. 7, no. 9, pp. 225–238, 2014.

[47] D. B. Grimes, R. Chalodhorn, and R. P. Rao, "Dynamic imitation in a humanoid robot through nonparametric probabilistic inference.," in *Robotics: science and systems*, pp. 199–206, Citeseer, 2006.

[48] T. Tanaka, H. Takeda, T. Izumi, S. Ino, and T. Ifukube, "Effects on the location of the centre of gravity and the foot pressure contribution to standing balance associated with ageing," *Ergonomics*, vol. 42, no. 7, pp. 997–1010, 1999.

[49] A. Kavounoudias, R. Roll, and J.-P. Roll, "Foot sole and ankle muscle inputs contribute jointly to human erect posture regulation," *The Journal of physiology*, vol. 532, no. 3, pp. 869–878, 2001.

[50] T. McGeer, "Passive dynamic walking," *The international journal of robotics research*, vol. 9, no. 2, pp. 62–82, 1990.

[51] N. Maalouf, I. Elhajj, D. Asmar, and E. Shammas, "Model-free human-like humanoid push recovery," in *RObotics and BIOmimetics (ROBIO), 2015 IEEE International Conference on*, IEEE, 2015.

[52] K. Harada, S. Kajita, K. Kaneko, and H. Hirukawa, "An analytical method for real-time gait planning for humanoid robots," *International Journal of Humanoid Robotics*, vol. 3, no. 01, pp. 1–19, 2006.

[53] T. Komura, H. Leung, S. Kudoh, and J. Kuffner, "A feedback controller for biped humanoids that can counteract large perturbations during gait," in *Robotics and Automation, 2005. ICRA 2005. Proceedings of the 2005 IEEE International Conference on*, pp. 1989–1995, IEEE, 2005.

[54] J. Pratt, J. Carff, S. Drakunov, and A. Goswami, "Capture point: A step toward humanoid push recovery," in *Humanoid Robots, 2006 6th IEEE-RAS International Conference on*, pp. 200–207, IEEE, 2006.

[55] J. Pratt and G. Pratt, "Intuitive control of a planar bipedal walking robot," in *Robotics and Automation, 1998. Proceedings. 1998 IEEE International Conference on*, vol. 3, pp. 2014–2021, IEEE, 1998.

[56] S.-H. Hyon, J. G. Hale, and G. Cheng, "Full-body compliant human–humanoid interaction: balancing in the presence of unknown external forces," *Robotics, IEEE Transactions on*, vol. 23, no. 5, pp. 884–898, 2007.

[57] A. Wright and S. Rothenberg, *Posture: Types, Assessment, and Control*. Human anatomy and physiology, Nova Science, 2011.

[58] C. A. Oatis, "The mechanics and pathomechanics of human movement," 2003.

[59] P. Gregorio, M. Ahmadi, and M. Buehler, "Design, control, and energetics of an electrically actuated legged robot," *IEEE Transactions on Systems, Man, and Cybernetics, Part B (Cybernetics)*, vol. 27, no. 4, pp. 626–634, 1997.

[60] R. Ortega, A. J. Van Der Schaft, I. Mareels, and B. Maschke, "Putting energy back in control," *IEEE Control Systems*, vol. 21, no. 2, pp. 18–33, 2001.

[61] M. W. Spong, "Energy based control of a class of underactuated mechanical systems," *IFAC Proceedings Volumes*, vol. 29, no. 1, pp. 2828–2832, 1996.

[62] M. W. Spong, "The swing up control problem for the acrobot," *IEEE control systems*, vol. 15, no. 1, pp. 49–55, 1995.

[63] P. G. Howlett, P. J. Pudney, and X. Vu, "Local energy minimization in optimal train control," *Automatica*, vol. 45, no. 11, pp. 2692–2698, 2009.

[64] S. Morimoto, H. Nakayama, M. Sanada, and Y. Takeda, "Sensorless output maximization control for variable-speed wind generation system using ipmsg," *IEEE Transactions on Industry Applications*, vol. 41, no. 1, pp. 60–67, 2005.

[65] A. I. Dounis and C. Caraiscos, "Advanced control systems engineering for energy and comfort management in a building environmenta review," *Renewable and Sustainable Energy Reviews*, vol. 13, no. 6-7, pp. 1246–1261, 2009.

[66] T. Nemoto, R. E. Mohan, and M. Iwase, "Energy-based control for a biologically inspired hexapod robot with rolling locomotion," *Digital Communications and Networks*, vol. 1, no. 2, pp. 125–133, 2015.

[67] S. Agrawal, R. S. Yadav, *et al.*, "A preemption control technique for system energy minimization of weakly hard real-time systems," in *Software Engineering, Artificial Intelligence, Networking and Parallel/Distributed Computing*, pp. 201–215, Springer, 2008.

[68] D. Gurdan, J. Stumpf, M. Achtelik, K.-M. Doth, G. Hirzinger, and D. Rus, "Energy-efficient autonomous four-rotor flying robot controlled at 1 khz," in *Robotics and Automation, 2007 IEEE International Conference on*, pp. 361–366, IEEE, 2007.

[69] A. A. Schäffer, O. Eiberger, M. Grebenstein, S. Haddadin, C. Ott, T. Wimböck, S. Wolf, and G. Hirzinger, "Soft robotics, from torque feedback-controlled lightweight robots to intrinsically compliant systems," *IEEE Robotics and Automation Magazine*, vol. 15, no. 3, pp. 20–30, 2008.

[70] S. M. Khansari-Zadeh and A. Billard, "Learning control lyapunov function to ensure stability of dynamical system-based robot reaching motions," *Robotics and Autonomous Systems*, vol. 62, no. 6, pp. 752–765, 2014.

[71] K. Matsusaka, M. Uemura, and S. Kawamura, "Realization of highly energy efficient pick-and-place tasks using resonance-based robot motion control," *Advanced Robotics*, vol. 30, no. 9, pp. 608–620, 2016.

[72] O. Khatib, J. Warren, V. De Sapio, and L. Sentis, "Human-like motion from physiologically-based potential energies," in *On advances in robot kinematics*, pp. 145–154, Springer, 2004.

[73] S. Nansai, M. Iwase, and M. R. Elara, "Energy based position control of jansen walking robot," in *Systems, Man, and Cybernetics (SMC), 2013 IEEE International Conference on*, pp. 1241–1246, IEEE, 2013.

[74] H. Jeong, O. Sim, H. Bae, K. Lee, J. Oh, and J.-H. Oh, "Biped walking stabilization based on foot placement control using capture point feedback," in *Intelligent Robots and Systems (IROS), 2017 IEEE/RSJ International Conference on*, pp. 5263–5269, IEEE, 2017.

[75] F. Asano and Z.-W. Luo, "Asymptotically stable gait generation for biped robot based on mechanical energy balance," in *Intelligent Robots and Systems, 2007. IROS 2007. IEEE/RSJ International Conference on*, pp. 3327–3333, IEEE, 2007.

[76] D. O. Morales and P. X. La Hera, "Design of energy efficient walking gaits for a three-link planar biped walker with two unactuated degrees of freedom," in *Robotics and Automation (ICRA), 2012 IEEE International Conference on*, pp. 148–153, IEEE, 2012.

[77] Z. Sun and N. Roos, "An energy efficient dynamic gait for a nao robot," in *Autonomous Robot Systems and Competitions (ICARSC), 2014 IEEE International Conference on*, pp. 267–272, IEEE, 2014.

[78] I. S. Godage, Y. Wang, and I. D. Walker, "Energy based control of compass gait soft limbed bipeds," in *Intelligent Robots and Systems (IROS 2014), 2014 IEEE/RSJ International Conference on*, pp. 4057–4064, IEEE, 2014.

[79] A. KhazeniFard, F. Bahrami, M. E. Andani, and M. N. Ahmadabadi, "An energy efficient gait trajectory planning algorithm for a seven linked biped

robot using movement elements," in *Electrical Engineering (ICEE), 2015 23rd Iranian Conference on*, pp. 1006–1011, IEEE, 2015.

[80] J. K. Holm and M. W. Spong, "Kinetic energy shaping for gait regulation of underactuated bipeds," in *Control Applications, 2008. CCA 2008. IEEE International Conference on*, pp. 1232–1238, IEEE, 2008.

[81] S. Y. Aleshinsky, "An energy sources and fractions approach to the mechanical energy expenditure problemi. basic concepts, description of the model, analysis of a one-link system movement," *Journal of biomechanics*, vol. 19, no. 4, pp. 287–293, 1986.

[82] L. Zhang, C. Zhou, P. Zhang, Z. Song, Y. P. Kong, and X. Han, "Optimal energy gait planning for humanoid robot using geodesics," in *Robotics Automation and Mechatronics (RAM), 2010 IEEE Conference on*, pp. 237–242, IEEE, 2010.

[83] L. Roussel, C. Canudas-de Wit, and A. Goswami, "Generation of energy optimal complete gait cycles for biped robots," in *ICRA*, pp. 2036–2041, 1998.

[84] Y. Hu and K. Mombaur, "Influence of compliance modulation on human locomotion," in *Robotics and Automation (ICRA), 2017 IEEE International Conference on*, pp. 4130–4137, IEEE, 2017.

[85] T. Otani, K. Hashimoto, S. Miyamae, H. Ueta, M. Sakaguchi, Y. Kawakami, H. Lim, and A. Takanishi, "Angular momentum compensation in yaw direction using upper body based on human running," in *Robotics and Automation (ICRA), 2017 IEEE International Conference on*, pp. 4768–4775, IEEE, 2017.

[86] K. Chao and P. Hur, "A step towards generating human-like walking gait via trajectory optimization through contact for a bipedal robot with one-sided springs on toes," in *Intelligent Robots and Systems (IROS), 2017 IEEE/RSJ International Conference on*, pp. 4848–4853, IEEE, 2017.

[87] Y. You, C. Zhou, Z. Li, and N. Tsagarakis, "A study of nonlinear forward models for dynamic walking," in *2017 IEEE International Conference on Robotics and Automation (ICRA)*, pp. 3491–3496, May 2017.

[88] M. Shafiee-Ashtiani, A. Yousefi-Koma, and M. Shariat-Panahi, "Robust bipedal locomotion control based on model predictive control and divergent component of motion," in *2017 IEEE International Conference on Robotics and Automation (ICRA)*, pp. 3505–3510, May 2017.

[89] T. Zhang, C. Liu, and Q. Chen, "Rebalance control for humanoid walking based on online foot position compensation," in *2017 IEEE/RSJ International Conference on Intelligent Robots and Systems (IROS)*, pp. 4605–4610, Sept 2017.

[90] T. Ishikawa, Y. Kojio, K. Kojima, S. Nozawa, Y. Kakiuchi, K. Okada, and M. Inaba, "Bipedal walking control against swing foot collision using swing foot trajectory regeneration and impact mitigation," in *2017 IEEE/RSJ International Conference on Intelligent Robots and Systems (IROS)*, pp. 4531–4537, Sept 2017.

[91] B. Stephens, "Humanoid push recovery," in *Humanoid Robots, 2007 7th IEEE-RAS International Conference on*, pp. 589–595, IEEE, 2007.

[92] N. S. El Khazen, *Omnidirectional humanoid fall avoidance strategies and decision volume.* PhD thesis, 2014.

[93] A. J. Davison, I. D. Reid, N. D. Molton, and O. Stasse, "Monoslam: Real-time single camera slam," *IEEE Transactions on Pattern Analysis and Machine Intelligence*, vol. 29, pp. 1052–1067, June 2007.

[94] F. Crete, T. Dolmiere, P. Ladret, and M. Nicolas, "The blur effect: perception and estimation with a new no-reference perceptual blur metric," in *Electronic Imaging 2007*, pp. 64920I–64920I, International Society for Optics and Photonics, 2007.

[95] G. Ligorio and A. M. Sabatini, "Extended kalman filter-based methods for pose estimation using visual, inertial and magnetic sensors: Comparative analysis and performance evaluation," *Sensors*, vol. 13, no. 2, pp. 1919–1941, 2013.

[96] A. Robotics, "Nao documentation," *Only available online: www. aldebaran-robotics. com/documentation*, 2012.

[97] F. Asano, M. Yamakita, N. Kamamichi, and Z.-W. Luo, "A novel gait generation for biped walking robots based on mechanical energy constraint," *Robotics and Automation, IEEE Transactions on*, vol. 20, no. 3, pp. 565–573, 2004.

[98] L. Yuan, L. Yuan, and H. Lu, "Energy optimization with multi virtual gravity for robotic gait," in *Digital Manufacturing and Automation (ICDMA), 2012 Third International Conference on*, pp. 388–392, IEEE, 2012.

[99] M. Scheint, M. Sobotka, and M. Buss, "Compliance in gait synthesis: Effects on energy and gait," in *Humanoid Robots, 2008. Humanoids 2008. 8th IEEE-RAS International Conference on*, pp. 259–264, IEEE, 2008.

[100] Y. Fujimoto, "Minimum energy biped running gait and development of energy regeneration leg," in *Advanced Motion Control, 2004. AMC'04. The 8th IEEE International Workshop on*, pp. 415–420, IEEE, 2004.

[101] S. Rodrigo, I. García, M. Franco, A. Alonso-Vázquez, and J. Ambrósio, "Energy expenditure during human gait. ian optimized model," in *Engineering in Medicine and Biology Society (EMBC), 2010 Annual International Conference of the IEEE*, pp. 4254–4257, IEEE, 2010.

[102] S. Rodrigo, I. García, M. Franco, A. Alonso-Vázquez, and J. Ambrósio, "Energy expenditure during human gait. ii-role of muscle groups," in *Engineering in Medicine and Biology Society (EMBC), 2010 Annual International Conference of the IEEE*, pp. 4858–4861, IEEE, 2010.

[103] H.-K. Shin and B. K. Kim, "Energy-efficient gait planning and control for biped robots utilizing vertical body motion and allowable zmp region," *Industrial Electronics, IEEE Transactions on*, vol. 62, no. 4, pp. 2277–2286, 2015.

[104] H. Nijmeijer and A. van der Schaft, *Nonlinear Dynamical Control Systems*. Berlin, Heidelberg: Springer-Verlag, 1990.

[105] H. K. Khalil, "Noninear systems," *Prentice-Hall, New Jersey*, vol. 2, no. 5, pp. 5–1, 1996.

[106] A. M. Bloch, N. E. Leonard, and J. E. Marsden, "Controlled lagrangians and the stabilization of mechanical systems. i. the first matching theorem," *IEEE Transactions on automatic control*, vol. 45, no. 12, pp. 2253–2270, 2000.